Li and B in ascending magmas: an experimental study on their mobility and isotopic fractionation

---

Roberta Spallanzani

Univ.-Diss.

zur Erlangung des akademischen Grades
"doctor rerum naturalium"
(Dr. rer. nat.)
in der Wissenschaftsdisziplin "Mineralogie"

eingereicht an der
Mathematisch-Naturwissenschaftlichen Fakultät
Institut für Erdwissenschaften
der Universität Potsdam

Ort und Tag der Disputation: Potsdam, 21.07.2022

Hauptbetreuer*in:	Prof. Dr. Max Wilke, Universität Potsdam Prof. Dr. Kenneth T. Koga, Université Clermont Auvergne
Betreuer*innen:	Dr. Sarah B. Cichy
Gutachter*innen:	Prof. Dr. Sumit Chakraborty, Ruhr Universität Bochum Dr. Francesco Vetere, Universitá degli studi di Perugia

https://doi.org/10.25932/publishup-56061
https://nbn-resolving.org/urn:nbn:de:kobv:517-opus4-560619

Declaration of Authorship

I hereby declare that this dissertation was prepared independently by the author, Roberta Spallanzani, without the use of any other means that the specified. All ideas derived from other sources are indicated as such. This work has been submitted only to the University of Potsdam.

Zusammenfassung

Diese Forschungsstudie konzentriert sich auf das Verhalten von Li und B während des magmatischen Aufstiegs und der Druckentlastungsbedingten Entgasung im Zusammenhang mit vulkanischen Systemen. Das Hauptziel dieser Dissertation besteht darin, festzustellen, ob es möglich ist, die Diffusionseigenschaften der beiden Spurenelemente als Instrument zur Verfolgung der magmatischen Aufstiegsgeschwindigkeit zu nutzen. Unter Verwendung von synthetischen Gläsern mit rhyolitischer Zusammensetzung und einem Wassergehalt von 4,2 Gew.-% wurden Diffusionspaar- und Druckentlastungsexperimente durchgeführt, um die Mobilität von Li und B zunächst in der Schmelze und dann in einem sich entwickelnden System während der Druckentlastungsgetriebenen Entgasung zu untersuchen.

Diffusionspaar wurden mit einem festen Druck von 300 MPa durchgeführt. Die Temperatur wurde im Bereich von 700-1250 °C variiert, wobei die Dauer zwischen 0 Sekunden und 24 Stunden lag. Unsere Ergebnisse zeigen, dass die Diffusionsfähigkeit von Li sehr schnell ist und bei sehr niedrigen Temperaturen auftritt. Eine Isotopenfraktionierung findet aufgrund der schnelleren Mobilität von ^{6}Li im Vergleich zu ^{7}Li statt. Die Diffusion von Bor wird durch die Anwesenheit von Wasser ebenfalls beschleunigt, bleibt aber langsamer als die von Li. Die Ergebnisse der Isotopenverhältnisse zeigen, dass die Bor-Isotopenfraktionierung durch die Speziation von Bor in der Silikatschmelze beeinflusst werden könnte, da ^{10}B und ^{11}B tendenziell eine tetraedrische bzw. trigonale Koordination aufweisen.

Druckentlastungsversuche wurden bei 900 °C und 1000 °C mit Drücken von 300 MPa bis 71-77 MPa und einer Dauer von 30 Minuten, zwei, fünf und zehn Stunden durchgeführt, um die Wasserauflösung und die Bildung von Gasblasen in der Probe auszulösen. Texturbeobachtungen und die Berechnung der Blasenanzahldichte bestätigten, dass die Blasengröße und -verteilung nach der Druckentlastung direkt proportional zur Druckentlastungsrate ist.

Generell zeigen die SIMS-Analysergebnisse von Li und B, dass die Konzentration der beiden Spurenelemente mit abnehmender Druckentlastungsgeschwindigkeit allmählich abnimmt. Dies ist darauf zurückzuführen, dass bei längeren Druckentlastungszeiten mehr Zeit für die Diffusion von Li und B in die Blasen zur Verfügung steht und die Schmelze

kontinuierlich flüchtige Bestandteile verliert, während die Blasen ihr Volumen ausdehnen.

Bei schnellen Druckentlastungen zeigen die Li- und B-Ergebnisse einen Konzentrationsanstieg mit einer δ^{7}Li- und δ^{11}B-Abnahme in der Nähe der Blasengrenzfläche, was mit der plötzlichen Bildung der Glasbläser und dem Auftreten eines Diffusionsprozesses in der entgegengesetzten Richtung, vom Blasenmeniskus zur unveränderten Schmelze, zusammenhängt. Wenn das Blasenwachstum dominiert und Li und B in die Gasphase übergehen, verarmt die Silikat Schmelze in der Nähe der Blase an Li und B, da die Spurenelemente stärker in die Blase diffundieren.

Unsere Daten werden auf verschiedene Modelle angewandt, die darauf abzielen, die Dynamik der Blasenkernbildung und des Blasenwachstums mit der Entwicklung der Spurenelementkonzentration und des Isotopenverhältnisses zu kombinieren. Hier werden erste Überlegungen zu diesen Modellen vorgestellt und abschließende Bemerkungen zu dieser Forschungsstudie gemacht. Diese Ergebnisse sind eine vielversprechende Grundlage für die weitere Untersuchung von Li und B, um dekompressionsbedingte Magma-Aufstiegsraten in vulkanischen Systemen zu ermitteln.

Abstract

This research study focuses on the behaviour of Li and B during magmatic ascent, and decompression-driven degassing related to volcanic systems. The main objective of this dissertation is to determine whether it is possible to use the diffusion properties of the two trace elements as a tool to trace magmatic ascent rate. With this objective, diffusion-couple and decompression experiments have been performed in order to study Li and B mobility in intra-melt conditions first, and then in an evolving system during decompression-driven degassing.

Synthetic glasses were prepared with rhyolitic composition and an initial water content of 4.2 wt%, and all the experiments were performed using an internally heated pressure vessel, in order to ensure a precise control on the experimental parameters such as temperature and pressure.

Diffusion-couple experiments were performed with a fix pressure 300 MPa. The temperature was varied in the range of 700-1250 °C with durations between 0 seconds and 24 hours. The diffusion-couple results show that Li diffusivity is very fast and starts already at very low temperature. Significant isotopic fractionation occurs due to the faster mobility of ^{6}Li compared to ^{7}Li. Boron diffusion is also accelerated by the presence of water, but the results of the isotopic ratios are unclear, and further investigation would be necessary to well constrain the isotopic fractionation process of boron in hydrous silicate melts. The isotopic ratios results show that boron isotopic fractionation might be affected by the speciation of boron in the silicate melt structure, as ^{10}B and ^{11}B tend to have tetrahedral and trigonal coordination, respectively.

Several decompression experiments were performed at 900 °C and 1000 °C, with pressures going from 300 MPa to 71-77 MPa and durations of 30 minutes, two, five and ten hours, in order to trigger water exsolution and the formation of vesicles in the sample. Textural observations and the calculation of the bubble number density confirmed that the bubble size and distribution after decompression is directly proportional to the decompression rate.

The overall SIMS results of Li and B show that the two trace elements tend to progressively decrease their concentration with decreasing decompression rates. This is explained because for longer decompression times, the diffusion of Li and

B into the bubbles has more time to progress and the melt continuously loses volatiles as the bubbles expand their volumes.

For fast decompression, Li and B results show a concentration increase with a δ^{7}Li and δ^{11}B decrease close to the bubble interface, related to the sudden formation of the gas bubble, and the occurrence of a diffusion process in the opposite direction, from the bubble meniscus to the unaltered melt. When the bubble growth becomes dominant and Li and B start to exsolve into the gas phase, the silicate melt close to the bubble gets depleted in Li and B, because of a stronger diffusion of the trace elements into the bubble.

Our data are being applied to different models, aiming to combine the dynamics of bubble nucleation and growth with the evolution of trace elements concentration and isotopic ratios. Here, first considerations on these models will be presented, giving concluding remarks on this research study. All in all, the final remarks constitute a good starting point for further investigations. These results are a promising base to continue to study this process, and Li and B can indeed show clear dependences on decompression-related magma ascent rates in volcanic systems.

Acknowledgements

I would like to start by thanking my supervisors, Max Wilke, Ken Koga, and Sarah B. Cichy, for their priceless support and help in all the aspects of my work at the University of Potsdam: technical, scientific, and moral. Max and Ken have always been an inexhaustible source of inspiration and support whenever I have needed them, and Sarah B. Cichy has not only been an incredible teacher, from whom I have learned and continue to learn every time, but she has also become a dear friend, who has been there for me during the discouraging moments I went through during these four years.

I would also like to thank the technicians at the University of Potsdam and GFZ, Christina, Christine, Jens, Antje, Reiner, Hans Peter, and Sebastian for the incredible work they did to allow me to progress in my research project, from sample preparation to technical support. Moreover, a huge thanks goes the secretaries of the University of Potsdam and the GFZ, Ines, Tanja, Martina, Cornelia, and Beate because they have been the most patient people in the world in helping me deal with every single German document since I moved here until my last day.

A giant thank you goes to my colleagues and friends, who have been an incredible moral and mental support during these four years: Lea, Alessia, Lélia, Magda, Theresa, Maria, Sebastian, Lukas, Jan, Jakob, and Niels have been of such great encouragement during my good days and bad days. They are an example for me in terms of strength, perseverance, and tenacity in working for a goal.

I would like to thank my family, who have always been by my side and never believed that I could not make it, not even for a single day. My parents Carla and Franco, Carlo, and Elena and in particular Diego believed in me even when I was the first one not to. They had the strength to support me in every situation, even when everything seemed to go wrong. They are the real reason for my success.

I would like to say a final thank you to my second family, my friends in Modena, who despite the distance have always been close to me and have always known how to make me relieve the stress accumulated at work. I would like to thank Ambra, Davide, Chiara, Samuele, Jessica, Sam, Andrea, Samuele and Gabriele for their precious moral support.

A Carla, Franco, Carlo e Diego

Table of contents

List of Figures

List of Tables

1. Introduction and aim of the study

Studying volcanic eruptions has been, notably in the last decades, a very intriguing topic for many scientists. Volcanic eruptions are the result of the combination of many geological processes and magma properties. The combination of these parameters generates a wide variety of eruptive phenomena that can dramatically affect the local and/or global population. One crucial aspect that influences deeply volcanic eruptions is the way magmas are stored at depth and how they are triggered to ascend to the surface through the volcanic conduit.

The scientific community tries constantly to implement tools for tracing magmatic ascent using a combination of different areas of study. Two primary areas are distinguished: real-time geophysical observations on the volcanic field, and a combination of geochemical and petrological studies of erupted materials. Typically the majority of available data on magmatic ascent is collected by real-time geophysical methods, such as the observation of the topographic deformation of the volcanic edifice, or seismological data which can trace real-time migration of the magmatic body at depth (e.g. Endo and Murray 1991; Teasdale et al.2015). Real-time geophysical observations can provide good estimates of magma ascent rates during volcanic eruptions in present times, but it is equally essential to be able to estimate magma ascent rates from past eruptions as well. In fact, each volcano has its own specific range of different eruption styles, and it is important to know what can be expected from every volcano, even those of which only historical evidence of their eruption dynamics is available. Secondly, a series of different geochemical and petrological methods can be applied to the erupted material. Examples of this approach consist in the study of crystal dissolution or formation during magmatic evolution, trace element diffusion in growing minerals, volatiles behaviour in erupted products or the application of field techniques such as the study of volcanic gas emissions at the surface (Spilliaert *et al.*, 2006; Cichy *et al.*, 2011; Armienti *et al.*, 2013; Vlastélic *et al.*, 2013; Richter *et al.*, 2014, 2017; Neave and Maclennan, 2020).

Alternatively, laboratory experiments are useful in the study of magmatic ascent, by the reproduction of naturally occurring processes in a controlled environment and with perfectly known parameters. It is possible to experimentally determine the phase relations between different mineral assemblages, the crystallization processes or perform decompression experiments at a controlled rate, to clarify the effect of the volatile components on the degassing phase of an ascending magma. In particular, the decompression rate has been proven to be related to the bubble size and distribution of erupted materials, quantified by the Bubble Number Density BND (Mourtada-Bonnefoi and Laporte, 1999, 2002, 2004; Nowak *et al.*, 2011; Fiege *et al.*, 2014; Marxer *et al.*, 2014; Fiege and Cichy, 2015).

Although the experimental approach has provided insightful results on the dynamics of bubble nucleation and growth, the use of the BND alone is not sufficient for a clear definition of the degassing path of a magma. Magmatic ascent is not a linear and constant process, bubble coalescence or the loss of volatile components significantly affects the ascent kinetics. This cannot be registered by the BND calculation, because it results from the sum of all these processes mixed together (Lautze *et al.*, 2011; Fiege and Cichy, 2015). Moreover, the bubble nucleation during ascent-related decompression is often heterogeneous, as it is affected by the presence and size of microlites that act as nucleation sites (e.g. Cichy et al. 2011).

Within this area of study, volatiles have been widely proven to be the main trigger for volcanic eruptions and to control magmatic degassing and eruption styles. Despite the considerable number of studies performed on the exsolution of volatiles, this process has still unclear timescales. Furthermore, evidence of disequilibrium degassing have been highlighted by several experimental studies, therefore the use of equilibrium degassing models is often unprecise (Mourtada-Bonnefoi and Laporte, 2004; Gonnermann and Manga, 2005; Namiki and Manga, 2006). This leads to the need for further investigations on degassing and ascent rates for a better understanding of the main parameters controlling this process.

Among the different techniques to trace magmatic ascent, geochemical tracers are an additional option. Noble gases or trace elements do not interfere with the dynamics of bubble nucleation and growth, thereby they can register magmatic degassing without modifying their asset in the silicate melt (Watkins *et al.*, 2017). Out of the possible elements, this dissertation will focus on lithium and boron because they have the right properties for the purpose of this research (e.g.

fluid-mobility, isotopic fractionation), highlighted by a few existing studies on their elemental and isotopic behaviour prior and during volcanic eruptions. These studies focus on the observation of natural samples and the combination of analyses of erupted material and surface gas geochemistry (Gillis *et al.*, 2003; Kuritani and Nakamura, 2006; Vlastélic *et al.*, 2011, 2013). Vlastélic et al. (2011, 2013) and Menard et al. (2013) highlighted an evident depletion of lithium and boron during volcanic eruptions that could be related to extensive magma degassing rather than differentiation or crystallization.

Lithium and boron are two light elements having atomic numbers 3 and 5, with small ionic radius. They are lithophile and moderately incompatible during mantle melting, found in volcanic systems as trace elements. They are highly fluid-mobile, therefore they preferentially partition into the fluid phase in the interaction between melt and fluid (Marschall *et al.*, 2007).

Lithium: Lithium is an alkaline metal element with an atomic mass of 6.94 u. Its two stable isotopes are ^{6}Li and ^{7}Li with relative abundancies of 7.5% and 92.5%, respectively. In a silicate structure, lithium ions tend to cluster with Non-Bridging-Oxygens, positioned in the interstices of the tetrahedral polymeric network. Hence, Li does not bond with the tetrahedral network, but its placement depends on the space left between SiO4 tetrahedra (Puls and Eckert, 2007). Its placement allows Li to be decoupled from the silicate structure, meaning that it can be described as a very fast-moving element (Ross *et al.*, 2015).

Lithium mobility has been largely studied in minerals and anhydrous melts of different compositions, and many of these studies confirmed that lithium diffusivity in in water-free melts is extremely fast, similar to nitrogen and hydrogen (Jambon and Semet, 1978; Giletti and Shanahan, 1997; Richter *et al.*, 1999; Zhang *et al.*, 2010). In spite of the numerous studies conducted on lithium diffusion in dry silicate melts, very few investigations have been performed at hydrous conditions. Recently, (Holycross *et al.*, 2018) presented a first study on lithium diffusion and isotopic fractionation in highly silicic, hydrous melts, demonstrating that the mobility of lithium increases strongly in the presence of water, compared to similar studies in dry conditions.

Concerning lithium isotopes, it is well known that ^{6}Li diffuses faster than ^{7}Li by ~12%, causing a very clear isotopic fractionation during diffusion processes

(Lesher and Spera, 2015; Holycross *et al.*, 2018). Richter et al. (2003) and Holycross et al. (2018) reported values of the diffusive fractionation coefficient (β) for lithium isotopes around 0.21 (Richter *et al.*, 2003; Holycross *et al.*, 2018), among the highest values reported for isotopic fractionation of elements. Although the two studies present an extremely different experimental setup, there is good agreement between Richter et al. (2003) and Holycross et al. (2018). Richter et al. (2003) studied the isotopic fractionation of lithium between a rhyolite and a basalt under dry conditions, while Holycross et al. (2018) presented a study based on diffusion-couple experiments between two samples of the same chemical composition, but in the presence of water. The two studies report similar results, although the experimental setups are significantly different. This generates uncertainties in the characterization of the lithium isotope fractionation process, considering that the combination of several different parameters could have led to similar results (Richter et al., 2003; Holycross et al., 2018).

Boron: Boron is a metalloid element with two in nature stable isotopes 11B and ^{10}B, with respective abundancies of 80.1% and 19.9% (Lécuyer, 2016; Foster *et al.*, 2018). Its structural role in silicates is more complicated than for lithium. Boron is usually dissolved in magmas in trigonal coordination as $BO_3$3-, but a minor percentage (2% in dry albitic melts, 6% in hydrous melts) is present in tetrahedral coordination as $BO_4$5- (Schmidt *et al.*, 2004). Interestingly, the most abundant isotope ^{11}B is mostly trigonally coordinated, which is also a weaker bond, compared to tetrahedral coordination. In contrast, the less abundant isotope ^{10}B is preferentially positioned in tetrahedral coordination, with a stronger bond with the oxygen of the silicate lattice (Schmidt *et al.*, 2004; Marschall and Foster, 2018).

Despite the large use of boron in geological research, very few studies investigated boron diffusivity in silicate melts (Baker, 1992; Chakraborty *et al.*, 1993), and only one reported preliminary results on boron mobility in hydrous melts (Mungall *et al.*, 1999). Mungall et al. (1999) reported that boron diffusivity, similarly to lithium, is increased by presence of water during diffusion processes. The lack of available data on this topic highlights the need to clarify boron mobility in highly silicic, hydrous melts.

Hervig et al. (2002) investigated the partition of B isotopes between fluid and melt, reporting that ^{11}B partitions preferentially into the fluid phase, rather than ^{10}B.

No studies have ever been reported on intra-melt diffusive isotopic fractionation of B isotopes, either in dry or hydrous melts. Only Chakraborty et al. (1993) attempted analyses of isotopic ratios after performing diffusion-couple experiments between a dry haplogranitic glass and a dry borate glass. Chakraborty's study did not identify any particular result in that case, concluding that the experimental setup was not prepared specifically for the study of boron diffusive fractionation and that further investigations were necessary.

1.1. Aim of the study

Considering the availability of data previously published on lithium and boron diffusion and isotopic fractionation and based on the geochemical results of Vlastélic et al. (2011, 2013) and Menard et al. (2013) the main course of action of this study were defined. The sole direct comparison between the bubble size and distribution and the decompression rate of an ascending magma is insufficient to develop a precise geospeedometer. In the products of volcanic eruptions, one can only see the results of the combination of several different processes. This does not always allow to determine precisely the magmatic ascent rate, as these processes can coexist together or evolve in time during magmatic eruptions. Therefore, geochemical tracers such as Li and B are a good option – in combination with the study of bubble size and distribution – to deeply understand the processes that occurred during the eruption and unravel helpful information that would not be detectable with other techniques.

The study is centred on rhyolitic melt compositions in order to avoid unwanted secondary effects (e.g. bubble coalescence or reabsorption) during the high pressure and high temperature experiments. Having set the main directives for the experimental approach, the main aim of this study is to evaluate whether it is possible to use Li and B diffusion as geochemical tracer for decompression-related volatile exsolution during magmatic ascent in volcanic systems.

It is essential to define the properties of chemical diffusivity and isotopic fractionation of lithium and boron under the conditions of a hydrous, rhyolitic silicate melt. This theme needs further development in relation to the existing literature: while lithium mobility has been examined only in the last years, almost no information is available on boron behaviour under these conditions. Therefore, there is a strong necessity of an extensive study on lithium and boron diffusion and isotopic fractionation.

A set of diffusion-couple experiments will be presented where diffusion of lithium and boron results were compared to the existing literature, and their behaviour was evaluated as a function of the water concentration in the silicate melt, in order to create a first connection between water content and Li and B mobility in rhyolitic melts. The study of lithium and boron diffusion in hydrated magmas was useful to characterise the homogenisation time of the two trace elements with the presence of water in the silicate melt. Hence, it was possible to define the time windows when the diffusion of lithium and boron is distinguishable.

Subsequently, following the results obtained by the study of Li and B diffusion, the main conditions for the second and central part of this study have been defined: Li and B diffusion was applied to a decompression-driven degassing magma, in order to find a relation between the mobility of the two elements and the dynamics of volatiles exsolution. This allowed to characterize a first link between the behaviour of Li and B and the magmatic ascent rate. With this intent, several decompression experiments were performed at different temperatures and decompression rates following the procedure presented by Koga et al. (2011). These experiments allowed us to apply the realistic conditions of an ascending magma and to better control the parameters involved in the degassing process.

For each decompression rate, the bubble size and distribution were associated to the effects of the lithium and boron exsolution process, in the area surrounding the bubbles formed by water exsolution. Several comparisons were discussed between the concentration and isotopic ratios of lithium and boron in the melt and the decompression rate of each experiment. This study can be further improved with the addition of parameters which better approach natural systems. Nonetheless, it constitutes a good basis for the development of a precise geospeedometer that uses the lithium and boron exsolution process as a tool to trace the ascent rate of an erupting magma.

2. Theoretical background: magma properties and eruption dynamics

2.1. Magma structure and properties

Magmas can be defined as a mixture of phases in gaseous, liquid, and solid state. They are usually composed of a portion of molten rock (liquid phase) in which small bubbles (gas phase) and crystals (solid phase) are present (e.g. Schmincke 2004). Their main constituent is silicon oxide, which is arranged in SiO_4-tetrahedra. As shown in a schematic representation in Figure 1, the tetrahedra are connected via corner-oxygens, creating a three-dimensional partially to fully polymerized network (Lockwood and Hazlett, 2010; Mysen and Richet, 2019).

Depending on the degree of chemical differentiation of magmas, their SiO_2 content usually ranges between 40-75 wt%, going from primitive basaltic magmas to highly silicic rhyolitic compositions. Natural melts are a mix of several major and minor elements, which create variations in the silicate melt structure at the microscopic scale (Al, Fe, Ca, Mg, Na, Ca, Ti, Mn, K, and P). These cations can be divided into two categories, depending on their effects on the polymerization of

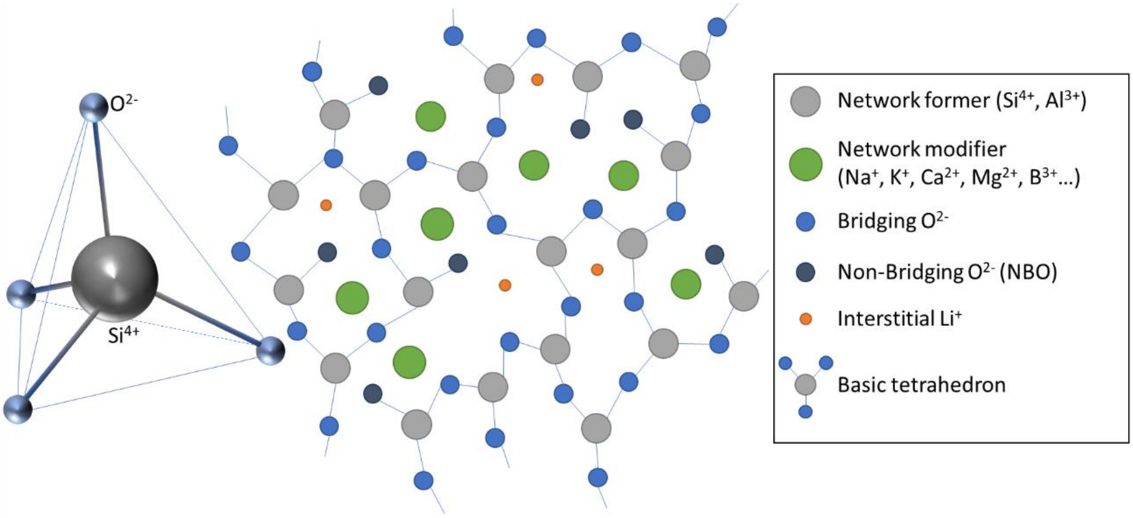

Figure 1: Schematic representation of SiO_2 tetrahedra and its disposition in space in silicate melts. Grey circles represent network-forming ions, such as Si or Al, while light blue circles are the bridging oxygens, linked to two network forming ions. Non-bridging oxygen are represented in dark blue, while green circles are network-modifying cations and orange circles are interstitial ions.

the silicon oxide tetrahedra. Network formers take the place of silicon in the network and are capable to continue the silicate structure by keeping the same charge balance as silicon ion (Si^{4+}). At low pressure, aluminium is the most common additional network former, because it has a similar ionic radius compared to silicon. Having a charge of +3, its substitution with silicon must be accompanied by a neighbouring charge-compensating ion in order to maintain the charge neutrality (Mysen and Richet, 2019). When the ratio between Al and charge-compensating cations is not balanced, Al may behave as a network modifier. The unbalanced charge causes a rupture in the network and oxygen cannot bond as usual with two network-forming cations becoming a Non-Bridging-Oxygen (NBO) and breaking the network (dark blue circles in Figure 1). NBOs are sites which do not continue the tetrahedral structure, decreasing the degree of polymerization of the silicate melt (Mysen and Richet, 2019). Most frequently, typical network modifiers are cations with large radius and/or high charge, such as alkali metals, alkaline earths, or high field strength elements, graphically represented by the green circles in Figure 1. Less commonly, small cations (e.g. Li) or inert components (e.g. N_2), can be included into the silicate structure but they do not bond to the SiO_4 tetrahedra. They can fit into the interstitial spaces between the silicon tetrahedra, making them decoupled from the rest of the structure (orange circles in Figure 1).

In order to numerically estimate the amount of NBO present in the structure of a silicate melt, the parameter NBO/T has been introduced, which numbers the amount of Non-Bridging Oxygens (NBO) per tetrahedrally coordinated cation (T). This value is however approximate, since it does not distinguish the kind of the considered cations (Mills *et al.*, 2014; Mysen and Richet, 2019). NBO/T can be calculated using the following equation, where X_{MO}, X_{M2O} are the mole fraction of MO (MgO, CaO, FeO, MnO…) and M_2O (Na_2O, K_2O…), respectively:

$$NBO/T = 2\left(\sum X_{MO} + \sum X_{M_2O} + X_{Al_2O_3}\right)/\left(X_{SiO_2} + 2\,X_{Al_2O_3}\right) \tag{1}$$

The value of NBO/T is going to be zero for fully polymerized melts and increases with decreasing degree of polymerization. Hence, highly silicic rhyolites have a smaller NBO/T value compared to basaltic magmas, which are significantly less polymerized.

Other constituents of magmas are volatile components (notably H_2O, CO_2, SO_2) and trace elements, so called because present in concentrations below 0.1 wt% (e.g. Rogers 2015). Volatile components are dissolved into the liquid phase of the magma when it is stored at depth. In particular, water has a deep impact on the melt structure and its properties, even at very low quantities (Mysen and Richet, 2019). It has a very wide range of concentrations in natural silicate melts, depending on the composition of the magma and the conditions of pressure and temperature. The presence of water dissolved in the silicate melt affects its phase stability, its physical and chemical properties, such as kinetic processes, and chemical reactions (Ihinger *et al.*, 1999; Mysen and Richet, 2019). Water can have a wide range of concentrations in magmas, depending on the composition of the magma, its storage depth, and its geodynamic context. The solubility of water in silicate melts is mainly controlled by pressure, but is also affected by H_2O concentration, composition of magma and its temperature. Generally, when water is incorporated into the silicate melt structure, oxygen ions bond with hydrogen and form OH^- groups, causing the rupture of the silicate lattice, and generating a drastic effect of depolymerization of the melt (Ihinger *et al.*, 1999; Mysen and Richet, 2019).

Different studies have discovered that water is present in the silicate structure in coexisting species, as OH^- groups and molecular H_2O compounds (Figure 2). The relative abundance of the two species can have a strong influence on the silicate melt structure, as OH^- groups are the main cause of the depolymerization of the melt lattice (Mysen *et al.*, 1980; Ihinger *et al.*, 1999; Ottonello *et al.*, 2018; Mysen and Richet, 2019). In glasses at room temperature, the number of OH^- groups is mostly controlled by the concentration of the total water in the liquid phase, as reported by shown in Figure 2A, where the concentration of OH^- groups and molecular H_2O is shown as a function of the total water concentration (Mysen and Richet, 2019). The increase of OH^- groups generates an increase in the NBO/T value, shown in Figure 2B: for equal amount of molecular H_2O, the higher the concentration of OH-groups, the higher the NBO/T value will be. At magmatic temperature, the relative abundance of OH^- groups and molecular H_2O is not only controlled by the water concentration, but temperature also plays a major role (Mysen and Richet, 2019). In fact, with increasing temperature, the OH^- groups

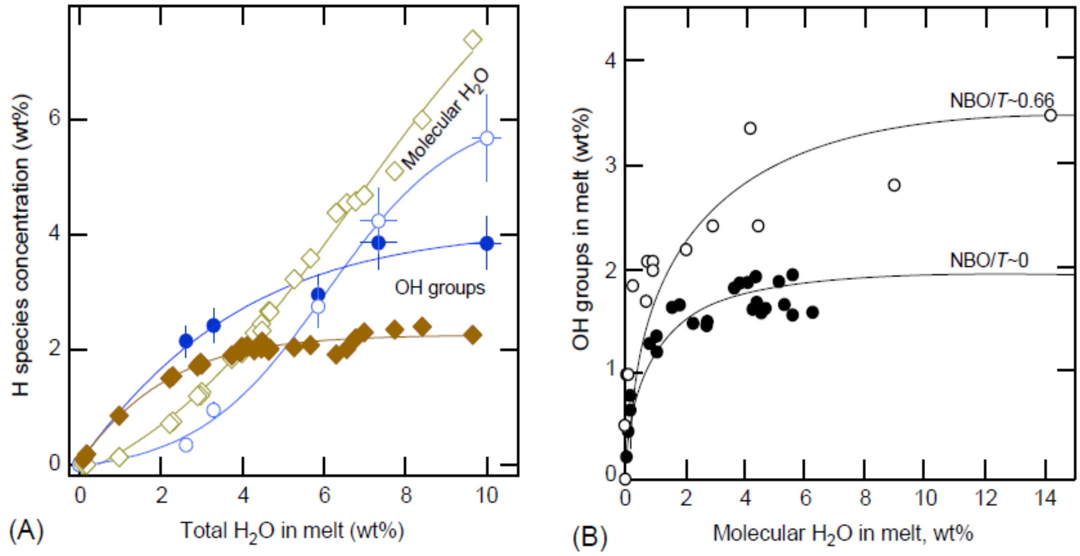

Figure 2: (A) Relative abundance of OH-groups (filled symbols) and molecular H_2O (empty symbols) in melts of different compositions (circles for $Na_2O{\cdot}4SiO_2$ and diamonds for $NaAlSi_3O_8$), as a function of the total water content. (B) Diagram of OH-groups versus molecular H_2O related to the NBO/T value (Mysen & Richet, 2019).

progressively become the dominant species in the silicate melt, while molecular H_2O simultaneously decrease its relative abundance (Nowak and Behrens, 2000).

Differently from the OH-groups, molecular H_2O has been found to be most likely positioned in the cavities between the SiO_4 tetrahedra, and it is considered to be chemically inert with respect to the silicate network (Mysen and Richet, 2019). Its behaviour approaches that of noble gases or other molecular compounds such as N_2 or O_2, which do not interact with the structure of the melt (Doremus, 1966; Shackelford *et al.*, 1972). The solubility of molecular H_2O is mostly controlled by the radius of the molecule and seems to be less affected by the degree of polymerization of the silicate structure, compared to other species, such as N_2 (Mysen and Richet, 2019).

The other major component of the gas phase in silicate melts is CO_2, which has usually very low concentrations in magmas, compared to water (typically on the order of thousands of µg/g at storage depth). Carbon dioxide, as water, can be present in two different forms in the silicate melt structure: as molecular CO_2 or as carbonate group CO_3^{2-} (Wallace *et al.*, 2015). Differently from water, its speciation is mainly controlled by the silicate melt composition, and increases linearly with pressure (Wallace *et al.*, 2015).

A crucial aspect of the study of volcanic eruptions is the understanding of magma transport properties. They involve the propagation of heat, chemicals or momentum in silicate melts (Dingwell, 2006; Wallace *et al.*, 2015) and affect deeply the mechanisms of differentiation, ascent, and eruption. The main transport properties are the melt viscosity, thermal conductivity, and chemical diffusion.

Magma viscosity describes the capacity to flow of the silicate melts and is mainly controlled by chemical composition and temperature. Melts with a high degree of polymerization tend to have a high viscosity, as the network is overall completely connected, and the bonds between connected tetrahedra refrain the material to flow easily. Temperature has the opposite effect: the more the temperature increases, the lower will be the viscosity. This occurs because the thermic energy is translated in stronger atomic vibrations, and this facilitates the rupture of the atomic bonds of the lattice (Bird *et al.*, 2006; Wallace *et al.*, 2015). Thermal conductivity is defined as the transport of heat within the silicate melt, and comprehends several processes such as convection, conduction and radiation, which all involve heat transfer into space (Bird *et al.*, 2006; Wallace *et al.*, 2015). Lastly, diffusion is the transport of particles at atomic or molecular scale.

2.2. Chemical diffusion and isotopic fractionation

One of the key processes taking place in magma chambers is chemical diffusion. This process can severely change the silicate melt composition or the atomic arrangement in the silicate network, leading to variations in the physical and chemical properties of magmas. Evidence of diffusive transport in minerals and melt can give interesting insights on what a magma went through, in terms of differentiation, cooling and degassing. Most commonly the observation of the diffusion process in silicate melts is applied to the study of mineral crystallization and dissolution during magmatic differentiation, but it can also be employed in the understanding of the evolution of the silicate melt over time, such as its cooling history and residence time in the magma chamber (Richter *et al.*, 2014, 2017; Costa *et al.*, 2020).

Diffusion is defined as the random migration of particles at atomic scale, and it is a strongly temperature-dependent process. It occurs always as random walk of particles, but in the case of a gradient in chemical composition, chemical diffusion is driven by the difference in chemical potential between two distinct parts of the system and it can occur in fluid and solid states (Crank, 1975; Liang, 2017). The mathematics of diffusion start with Fick's first law, which has an identical mathematical form as the heat conduction equation to mass transfer (Fick, 1855; Crank, 1975). The flux J is a vector that defines the direction of the particle flow and the transfer rate per unit area for a diffusing substance a. Flux J of the element a is calculated by the following equation:

$$J_x^a = -D\frac{\partial C^a}{\partial x}$$

2

where C^a is the concentration of the diffusing particle a, and x is the distance unit perpendicular to the section (Figure 3A). The diffusion coefficient D^a describes the capacity of the particle to migrate in a specific material. Its value is very specific for each element or compound and varies as a function of the diffusion medium. For instance, if the composition of the magma changes, D^a will change as well.

However, Fick's first law can only locally describe the evolution of a system with time. A development of this law brings to the second law of Fick, where the mass transfer and the concentration change with time in a finite volume. Looking at Figure 3B, assuming that the only operating process on the system is diffusion (and no outer inputs can change the particle asset), the flux J for a certain space distance dx can be considered as the net budget of the particles entering the box J(x), and particles going out from the box J(x+dx).

$$\frac{\partial C^a}{\partial t} = D^a\frac{\partial J_x^a}{\partial x^2} = \frac{\partial}{\partial x}\left(D^a\frac{\partial C^a}{\partial x}\right)$$

3

In this equation, t is the time during which diffusion progressed. If D^a is constant throughout the entire diffusion process, Fick's second law is obtained, where D^a is a function of the distance x and the time t, writing equation 3 as follows:

$$\frac{\partial C}{\partial t} = D\frac{\partial^2 C}{\partial x^2}$$

4

Fick's second law needs to be further developed if the diffusion is seen as a three-dimensional process. This can be reduced when the diffusion medium is isotropic and for suitable boundary conditions, e.g. if transport is considered for

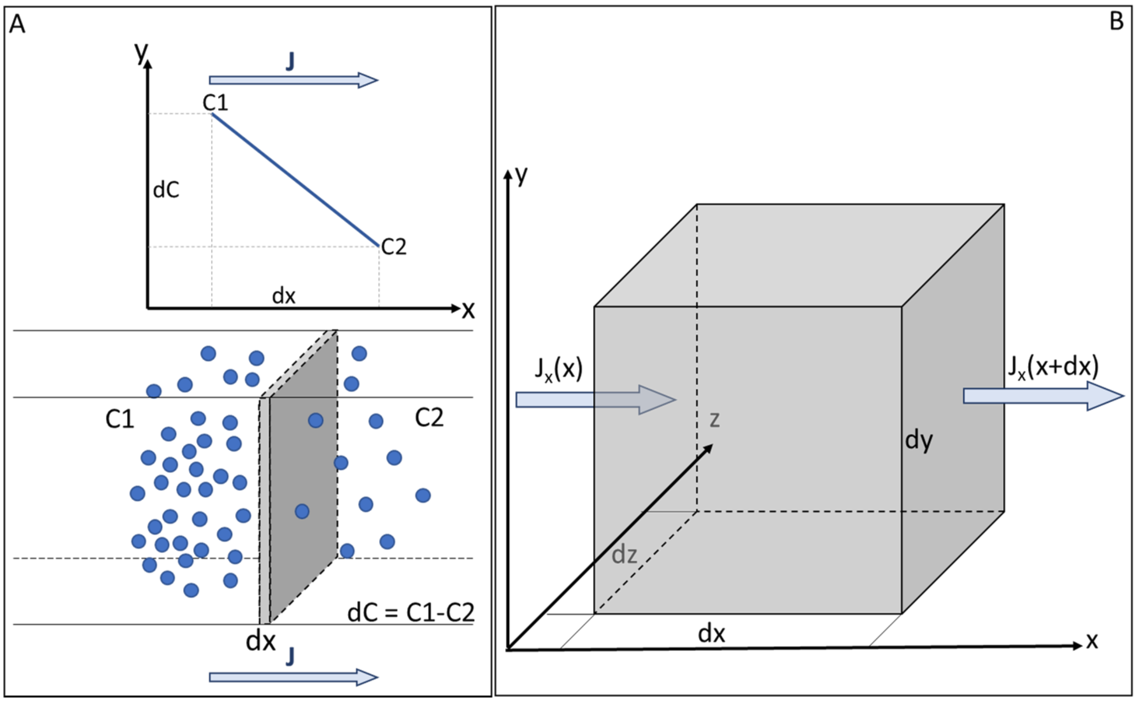

Figure 3: Schematic representation of the Fick's first (a) and second (b) laws for an isotropic, three-dimensional medium.

only one direction as in magmas and glasses of this case study: D and J have the same values along the three spatial components, no matter what the direction of the ongoing diffusion is. A more complicated situation is verified often for the study of the diffusion process in many crystals, where the particle migration is allowed only in very specific sites, depending on the mineral lattice. Here, the same diffusing particles move at different rates as a function of the direction of movement. In this case, both D and J have to be decomposed into their three-dimensional components (Crank, 1975; Chakraborty, 1995; Mehrer, 2007).

The diffusion process can be divided into categories, depending on the type of diffusing species, the chemical state of the host material, and the initial conditions for particle motion. In particular, two main categories of diffusion are distinguished: multi-component or chemical diffusion and self- or intra-melt diffusion. The first type of diffusion involves several species of diffusing particles moving in opposite directions. Typically, it occurs during magma mixing, when two melts in contact have significantly different chemical composition and are in chemical disequilibrium. This type of diffusion occurs when the mobility of an element in one direction is influenced by the diffusion of another element (or more) in the opposite direction, in the attempt to maintain the mass-transfer balance between the two processes taking place at the same time (Chakraborty, 1995, 1997; Dohmen and Chakraborty, 2007; Liang, 2017). This process is strongly concentration-dependent of at least two if not all interdiffusing species, and results in asymmetric diffusion profiles (Chakraborty *et al.*, 1993; Chakraborty, 1997). A common example is the interdiffusion of Mg-Fe in olivine, reported by Chakraborty et al. (1997).

Self-diffusion or intra-melt diffusion usually involves the migration of particles in a chemically homogeneous medium. In this case, diffusion is triggered by a chemical gradient between trace elements only, which do not significantly modify the arrangement of the major elements in the silicate network. Alternatively, it is considered self-diffusion when the process involves the different isotopes of an element. Here, the host-magma is chemically completely homogeneous, but presents differences in the relative concentration of the isotopes of the same element (Chakraborty, 1995; Liang, 2017).

The diffusion process is strongly dependent on temperature and composition of the silicate melt. The diffusion coefficient is related to the temperature by the Arrhenius relation which allows to determine the values of the activation energy E_a and the pre-exponential factor D_0.

$$\mathrm{D} = \mathrm{D_0} \exp\left(-\frac{\mathrm{E_a}}{\mathrm{RT}}\right) \tag{5}$$

T is the temperature expressed in K, and R is the ideal gas constant. On a plot of ln D vs 1/T this equation defines a linear trend as exemplified in Figure 4. The activation energy and D_0 can be determined from the slope of a linear regression

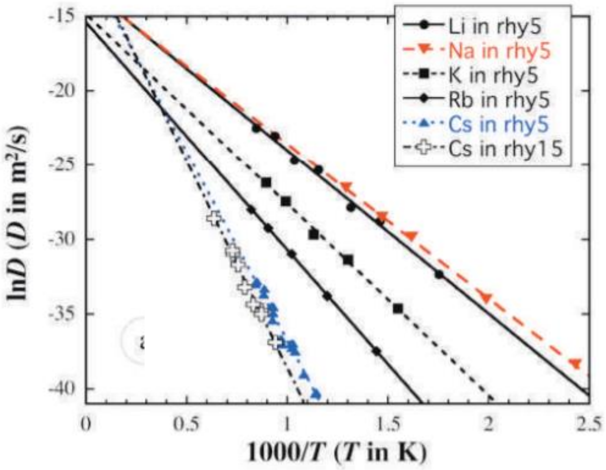

Figure 4: Data collection on the diffusivity of different alkali elements in dry rhyolitic melts available on the existing literature and reported by the review of Zhang et al. (2010).

of measured D-values and axis intercept, respectively (Mehrer, 2007; Zhang *et al.*, 2010). The activation energy is defined as the minimum amount of energy that an ion needs to start moving from its own site, in order to be able to jump to a surrounding site. The smaller the slope in an Arrhenian diagram, the lower the activation energy, therefore the easier it will be for a certain particle to start moving in the host medium.

Figure 4 reports the available data on alkali earth elements diffusion in rhyolitic melts, collected and reviewed by Zhang *et al.* (2010). In the picture, the linear regression of the different datasets visually shows the activation energy of each element in glasses of rhyolitic composition. The review from Zhang et al. (2010) highlights that usually, smaller elements have a faster diffusion. For instance in the case of lithium, Zhang et al. (2010) reports that in dry rhyolitic melts lithium diffusivity is overall similar to the one of sodium, but significantly faster than other alkaline elements, such as K, Rb and Cs (Zhang *et al.*, 2010; Ni *et al.*, 2015).

It is well known that chemical diffusion and viscous flow can be associated in terms of process kinetics (Chakraborty, 1995; Behrens and Haack, 2007). The Eyring equation establishes the relation between viscosity, diffusion and the temperature based on principles of Brownian motion (Kauzmann and Eyring, 1940; Chakraborty, 1995; Mungall, 2002) and successfully describes this relation for species where viscous flow and diffusive motion are highly correlated. This equation is usually applied to describe the process of viscous flow in relation to the melt composition and temperature (Mungall, 2002). Furthermore, the Eyring equation has been proven to be successfully used to characterize the process of diffusion for slow-moving network formers within the silicate melt using the equation 6:

$$\mathrm{D} = \frac{\mathrm{k_B T}}{\eta\lambda} \tag{6}$$

where k_B is the Boltzmann constant, T is the temperature in K, η is the viscosity of the host melt and λ is the jump distance of the diffusing species between two adjacent sites in the host medium (e.g., Mungall 2002). This equation is often only valid for slow moving species that are dominated by the polymerized network, such as high field-strength elements (i.e. Hf, Ti, Zr; Mungall et al.1999) while it cannot be taken into consideration for fast-diffusing species, as they commonly are decoupled from motion of the silicate network and are less dependent on the chemical composition of the host-magma (Chakraborty, 1995). Viscous flow and chemical diffusion are equally affected by the addition of water, among other components, as it usually facilitates and accelerates the two processes (Watson, 1994; Chakraborty, 1995).

When diffusion acts on stable isotopes of an element, the two isotopes can respond slightly different due to the different masses and relative abundance (as shown in Figure 5, (Mungall *et al.*, 1999). In this case isotopic fractionation occurs, which can also be used as a geochemical tracer for magmatic processes. In this study, the isotope ratio will be transformed into the relative "delta notation". This value describes the relative variation of the isotopic ratio in comparison to the reference material and is normalised to ‰ variation. In the following equation and Figure 5, ^{a}X and ^{b}X are the concentration of heavy and the light isotopes of the element X, respectively.

$$\delta\,^{a}X = \left(\frac{\left(^{a}X/\,^{b}X \right)_{sample}}{\left(^{a}X/\,^{b}X \right)_{reference}} - 1 \right) * 10^{3} \tag{7}$$

Diffusive fractionation is a complex process, and the isotope ratio reflects the behaviour of individual isotopes, including their speciation within the silicate structure. The most classical representation of isotopic fractionation is shown in Figure 5: if the element only has one coordination site in the melt (as for the case of lithium), the fractionation of the two isotopes is only controlled by the progress of chemical diffusion. In this case, the relation occurring between the diffusivity of the two different isotopes is defined by the parameter β (Richter *et al.*, 1999, 2003). This parameter correlates the difference between the isotopic masses and the diffusion coefficients, and is determined by the following equation, where m_a and m_b are the masses and D_a and D_b are the diffusion coefficients of the two isotopes.

$$\frac{\mathrm{D_a}}{\mathrm{D_b}} = \left(\frac{\mathrm{m_b}}{\mathrm{m_a}} \right)^{\beta} \tag{8}$$

If an element can occur in more than one coordination site, the effect of isotopic fractionation during diffusion becomes more complex than illustrated in

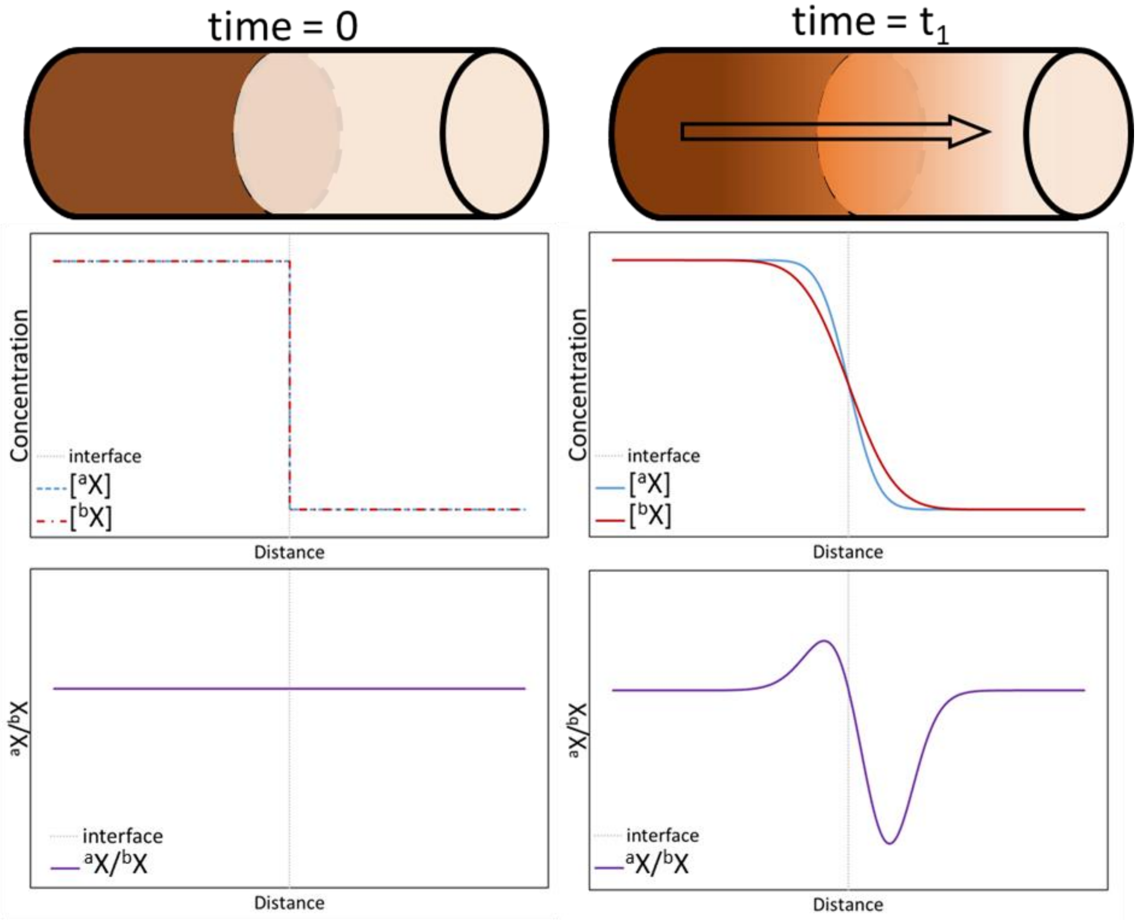

Figure 5: Schematic representation of diffusion for different isotopes of the same element, with the evolution of the concentration and isotopic ratio before and after diffusion.

Figure 5. In the case of boron, two coordination sites occur in silicate melts, and ^{11}B is preferentially fractionated into the trigonal site, while ^{10}B fractionates mostly into the tetrahedral site (Kakihana *et al.*, 1977). This generates a superposition of parameters, controlling the boron isotopic fractionation. This effect is mostly generated by the difference in the bond strength between boron in trigonal and tetrahedral coordination: B–O bonds are significantly stronger when boron is in tetrahedral coordination because of the shorter B–O distance (Hervig *et al.*, 2002; Kowalski *et al.*, 2013).

Being a mass-dependent process, the definition of the isotopic fractionation effects of stable isotopes has been largely used to trace differentiation processes or magma mixing. Particular interest has been given to isotopic fractionation to trace degassing processes of magmas, because of the strong tendency of many isotopes to partition between the gas and melt phase (Vlastélic *et al.*, 2011, 2013).

2.3. Magmatic ascent, degassing, and eruption

Volcanic eruptions occur in a multitude of different styles, as they are strongly influenced by several variables, which interact together before and during magmatic ascent. The structure of the volcanic edifice, the chemical composition of the magma, the temperature and the volatile budget are only a few of the parameters that affect the eruption style and dynamics. The magma is commonly stored underneath the surface in a series of magma chambers, variable in size, number, and depth. For highly active volcanoes, the residence time of the magma between its formation and the eruption ranges usually between 1 and 100 years (Pyle, 1992). For highly silicic, highly explosive volcanoes the magma residence time is estimated in the range 1-500 ky, depending on the characteristics of eruption and the aspect of the volcanic complex (Costa, 2008).

Perturbation of the conditions of a magma chamber (i.e., replenishment of the reservoir from a deep source input, cooling, and crystallization of the stored magma) can generate an overpressure inside the reservoir and provoke the beginning of the magma ascent towards the surface. In this scenario, volatile components reach oversaturation, where their concentration exceeds their solubility at given conditions (Zhang, 1999; Acevedo, 2020). A gas phase begins to separate from the silicate melt, forming bubbles of different shape and size,

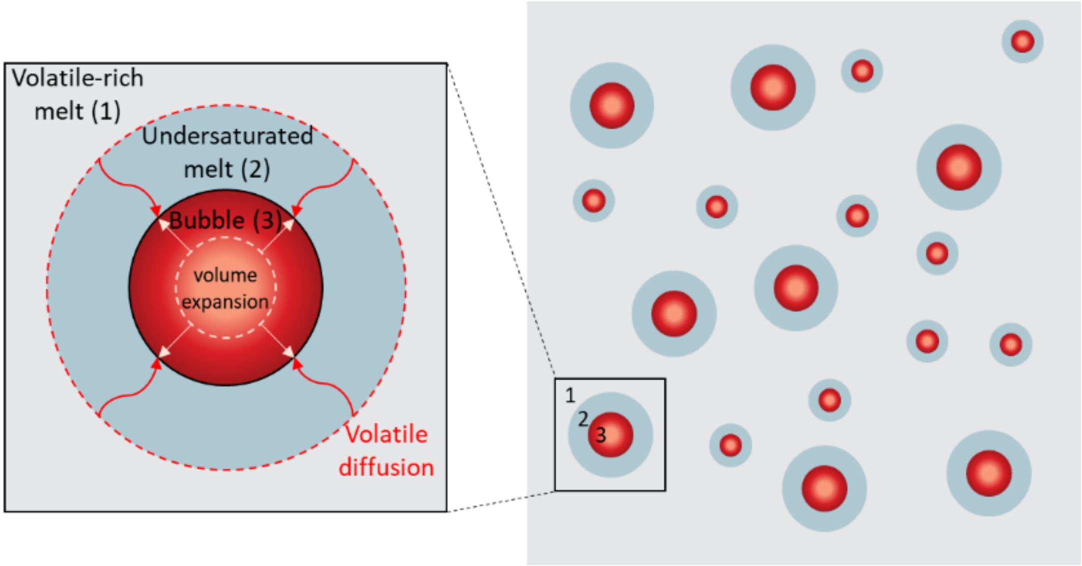

Figure 6: Dynamics of bubble growth, considering three separate areas: (1) the homogeneous volatile-rich silicate melt, not interested by the bubble growth; (2) a melt area characterized by diffusion of volatiles into the bubble and by undersaturated conditions; (3) the enlarging bubble, growing in volume due to gas expansion. Figure re-drawn from Gonnermann and Gardner (2013).

depending on the ascent-induced decompression rate (Gonnermann and Manga, 2007; Wallace *et al.*, 2015). In the initial stage of magmatic ascent, numerous small bubbles start to nucleate (Gonnermann and Manga, 2012). These bubbles will grow leading to an overall decrease of the bulk density of the magma and increasing buoyant forces (e.g., Gonnermann and Manga, 2007).

In natural systems, bubble nucleation is very complex, as it can be affected by many different parameters. In general, this process is divided into homogeneous and heterogeneous bubble nucleation (Mourtada-Bonnefoi and Laporte, 1999; Mangan and Sisson, 2000; Fiege *et al.*, 2014; Fiege and Cichy, 2015). Homogeneous bubble nucleation occurs when the magma has no pre-existing gas phase before starting its decompression-driven degassing. Additionally, no crystal microlites are present in the magma, to function as a nucleation site. In this type of bubble nucleation, the gas phase is entirely produced by the decompression-induced magma degassing during its ascent (Mourtada-Bonnefoi and Laporte, 1999; Gonnermann and Manga, 2007; Cichy *et al.*, 2011; Toramaru, 2022). On the contrary, heterogeneous bubble nucleation occurs when microlites constitute nucleation sites, or when a gas phase was already existing in the magma chamber prior to the magmatic ascent, due to differentiation and/or magma cooling (Gonnermann and Manga, 2007; Acevedo, 2020).

When the overpressure of the gas phase allows the bubbles to grow instead of being re-absorbed, the bubbles start to expand, because during ascent and decompression, the solubility of the volatile components continues to decrease (Figure 6) The volatile components (mainly H_2O) start to diffuse into the growing bubble, as represented schematically in Figure 6, while the bubble continuously expands its volume inside the liquid phase. However, during magma ascent, the volume expansion of the bubble is limited because the silicate melt progressively loses volatile components, with a consequent increase in its viscosity (Gonnermann and Manga, 2007, 2012).

The type of volcanic eruption is not only determined by simple bubble nucleation and growth, but results from the sum of several secondary processes that can take place between the ascending magma and the gas phase. Figure 7 shows the principal types of eruption, and highlights which processes develop in the shallow level of the volcanic conduit. In the case of highly silicic, highly viscous magmas, two extreme scenarios are represented by Figure 7A and Figure 7B, where the main difference between the two types of eruption is whether the gas phase reaches the surface or not. Typically, this is defined by the ascent rate: in Figure 7A the ascent occurs at very low rates and in open-system conditions.

Outgassing can occur in all types of magmas: the volatile phase escapes from the ascending magma through permeable flow (Gonnermann and Manga, 2012), and the gas phase separates from the silicate melt via fractures and pores, generating highly degassed lava flows, or intrusive dykes (Gonnermann and Manga, 2012). Figure 7B shows the opposite situation when magma ascent is fast enough to cause fragmentation of the magma. In this case, the magma does not behave as a liquid, but rather has a brittle response to the stress of ascent. The melt will not be able to re-arrange its structural units, and the magma body will

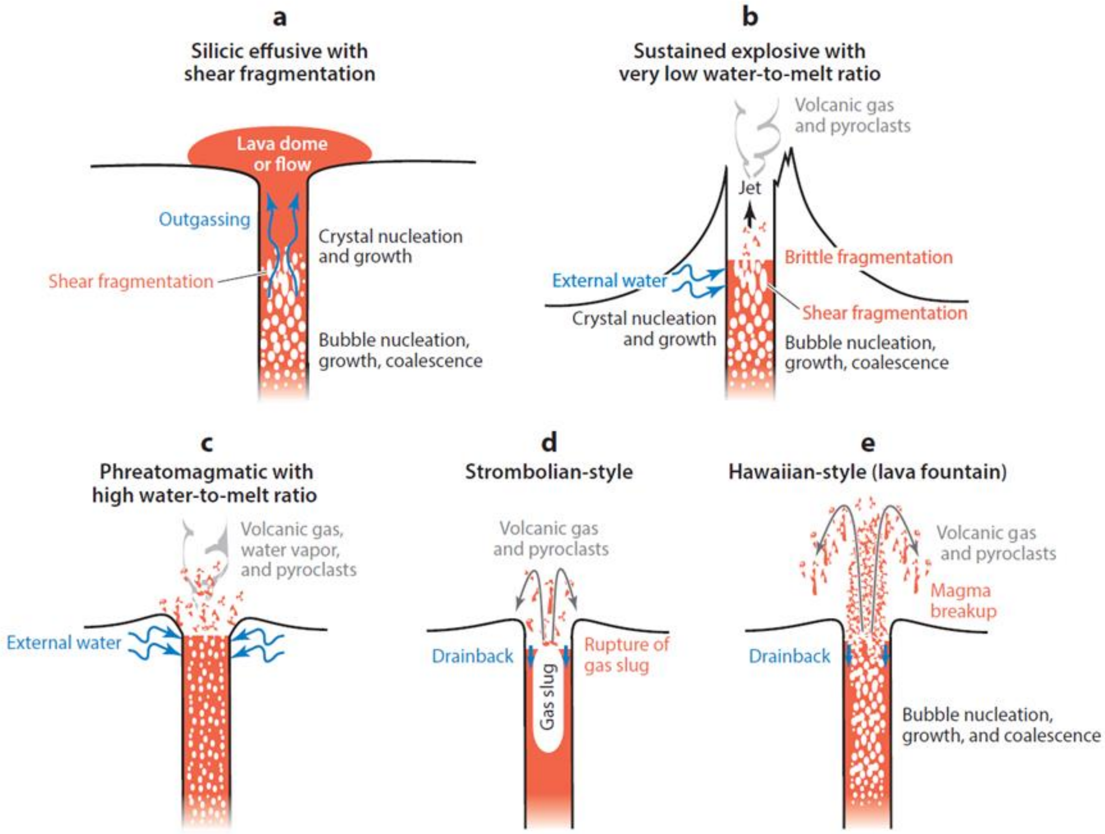

Figure 7: Visual representation of volcanic eruptions in their different dynamics (Gonnermann and Manga, 2007). (a) effusive eruptions generated by the complete loss of volatiles through outgassing. (b) magma fragmentation leading to explosive plinian/sub-plinian activity. (c) Interaction between magma and external water resulting in phreatomagmatic eruptions. (d) Strombolian mildly explosive eruptions caused by massive bubble coalescence and the formation of big gas slugs. (e) Hawaiian eruptions, characterized by low viscosity magmas and eruption of not completely degassed material.

break up into liquid or solid pyroclasts and rock fragments that are ejected at high velocity at the surface (Gonnermann, 2015).

Magma fragmentation mainly occurs due to gas phase overpressure, but it can be caused as well by sudden increase of the gas phase volume due to interaction between magma and external water (as for the case of phreatomagmatic eruptions, Figure 7C). Moreover, it can involve only a portion of the volcanic conduit, i.e. when the shear stress given by magmatic ascent gets an elastic response only at the contact with the volcanic conduit walls (Gonnermann, 2015).

Bubble coalescence takes place when several bubbles blend together to form a bigger unit. Since the velocity of bubble ascent is proportional to its radius, this process has severe implications on the eruption style, in particular regarding the separation of the gas phase from the liquid phase (Gonnermann and Manga, 2007; Toramaru, 2022). Previously mentioned process is more evident in low-viscosity melts, where the bubbles can move within the liquid phase more freely. In such scenarios, the bubble ascent is extremely fast compared to magmatic ascent. As shown in Figure 7D, big slugs may form from the coalescence of a large number of bubbles, accumulating towards the upper part of the rising magma and producing strombolian eruptions (Gonnermann and Manga, 2007). For low-viscosity melts, if the volatile component remain in the melt phase along the entire magmatic ascent, as it is the case of Hawaiian eruptions, shown in Figure 7E, where pyroclasts and scoria are ejected at the surface via volatile-rich lava fountains (Gonnermann and Manga, 2012).

As the magma ascent in the volcanic conduit is not a steady phenomenon, two or more of these processes can combine together, and the products of the eruptions are not able to record the involved processes by the sole observation of the bubble number and distribution. From here, the association to the study of magma vesiculation of trace elements (such as lithium and boron) as geochemical tracers would allow for better constraining which processes played a role in the magmatic ascent phase and can help improving the knowledge on magmatic ascent rates, prior to volcanic eruptions.

3. Experimental setup and analytical methods

3.1. Starting material and sample preparation

For the diffusion-couple and decompression experiments, synthetic glasses have been prepared because of the possibility to have good control on a simplified system, which could be modified following the requirements of this study. The glass composition chosen for this research project corresponds to the one from the obsidian of the Cerro de Los Posos volcano near Bandelier, New Mexico (Stanton, 1990). This area is very well studied, and this obsidian is used as a reference material for SIMS measurements of lithium at the Arizona State University, USA.

Two different batches of starting glasses were prepared with the same major element composition but different lithium and boron concentration. The two series were called LPR50 and LPR200 for the depleted and enriched starting glass, respectively (Los Posos Rhyolite, LPR), and constitute the two endmembers for the diffusion-couple experiments. Several different components were mixed (SiO_2, Al_2O_3, $CaCO_3$, MgO, Na_2CO_3, K_2CO_3) and the two batches were doped with specific amounts of $Li_2B_4O_7$, whose addition to both mixtures resulted in different Li and B concentrations, but identical isotope ratios in both batches (Table 1). The mixtures were placed in platinum crucibles and melted in a one-atmosphere oven at 1000 °C for two hours, subsequently ramping up to 1600 °C for four hours. The obtained melt was quenched in a water bath (Cichy *et al.*, 2011) and ground into fine powder. A second stage of melting in the Pt crucibles (four hours at 1600 °C) was conducted to ensure complete homogenization of the synthesized glass. Afterwards, the obtained glasses were manually ground into powder in an agate mortar with two grain sizes < 63 µm and 63-150 µm by sieving the glass powder. They were then mixed in a 1:1 mass ratio (e.g. Cichy 2011), to reduce as much as possible the air-filled space between grains and to suppress bubble formation in the following steps of the experimental procedure.

Initially prepared glasses were planned to have 1.14 wt% of total iron (Fe_2O_3 + FeO) and 0.10 wt% of TiO_2, but tests of the glass synthesis revealed that at the conditions chosen for the experiments it was not possible to obtain homogeneous, completely bubble-free glasses due to the presence of microlithic oxides of Fe and Ti, which are known to affect the bubble nucleation process (Hurwitz and Navon, 1994). Hence, new glass batches were prepared whose composition is reported in Table 1, without adding Fe and Ti in the mixture, these elements considered neglectable in the chosen rhyolitic composition. This choice indeed prevented the formation of undesired oxide microlites in the synthesized glasses, allowing to perform both diffusion-couple and decompression experiments (even though microprobe analyses detected very small amounts of Fe and Ti in the newly prepared glasses).

Table 1: Composition of the synthetic glasses and the natural Los Posos rhyolitic obsidian.

Oxide [wt%]	**LPR50**	**LPR200**	**Los Posos rhyolite (Stanton, 1990)**
SiO_2	74.7 ± 0.5	74.6 ± 0.4	76.6
Al_2O_3	12.9 ± 0.2	13.0 ± 0.2	12.7
K_2O	3.76 ± 0.03	3.77 ± 0.03	4.60
Na_2O	3.92 ± 0.06	3.96 ± 0.04	4.10
CaO	0.35 ± 0.02	0.36 ± 0.02	0.31
MgO	0.04 ± 0.01	0.038 ± 0.005	0.02
Fe_2O_3	-	-	0.56
FeO	0.08 ± 0.03	0.07 ± 0.02	0.58
TiO_2	0.02 ± 0.03	0.03 ± 0.01	0.1
MnO	0.009 ± 0.003	0.009 ± 0.004	-
H_2O	4.2 ± 0.5	4.2 ± 0.6	-
Li [µg/g]	58 ± 10	200 ± 10	35
B [µg/g]	170 ± 30	600 ± 30	-

For the decompression experiments generally two capsules were prepared at each experiment, one with the depleted and one with the enriched starting glass powder. Capsules were prepared using Pt or Au-Pd tubes 3.4 mm of diameter and of 15 mm length, filled with the starting powder and an amount of distilled water to get an initial 4 wt% content (undersaturated conditions). The filled capsule has been gently squeezed on its sides in order to prevent capsule opening during the decompression, as the bubble growth inside the Pt tube causes a general increase of the volume of the melt (Figure 8). Finally, the capsules were welded shut by point welding. The capsules sealing was verified by placing them into a 100 °C oven for ca. 10 minutes, checking that the weight before and after the test remained constant. The diffusion-couple experiments required an additional step of glass synthesis at high pressure and high temperature, which allowed to get bubble-free hydrous glass cylinders of each starting material.

To obtain homogeneous water-bearing glass cylinders (Figure 8), a first synthesis at high pressure and temperature was performed using an internally heated pressure powder and distilled water to obtain a homogeneous glass with a water content of 4.2 wt%. To homogenise the water-bearing silicate melt, the IHPV was kept stable for 48 hours at pressure and temperature conditions of 300 MPa and 1200 °C. After the experiment, the capsules were confirmed to have not leaked by comparing the weight before and after the experimental run. Then the platinum capsule was peeled off leaving the glass intact. Approximately 5 mm thick slices were cut, mounted in epoxy, and polished before drilling multiple glass cylinders with diameters of 3.6 mm.

This procedure ensured that the produced glass was bubble-free and homogeneous, before performing the diffusion-couple experiment. Subsequently, the polished surfaces of the two glasses identical in major element composition

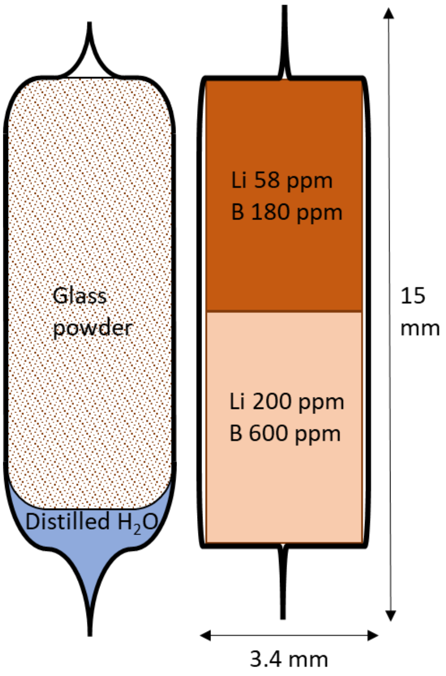

Figure 8: Schematic image of the decompression samples (left) and the diffusion-couple samples (right).

but differing in lithium and boron contents, were put in contact within a platinum capsule. The bottom part of the capsule was flattened into a cylindrical shape to tightly fit the glass cylinders, reducing the air trapped in the capsule after being sealed.

3.2. The Internally Heated Pressure Vessel

All the experiments of this study have been performed using internally heated pressure vessels (IHPV) at the GeoForschungsZentrum in Potsdam and the University of Göttingen, in Germany. This instrument is very well suited to recreate the conditions of the Earth's upper crust and in particular the temperature and pressure of an average magma storage chamber. An IHPV can keep these conditions for several days with exceptional stability and neglectable temperature gradients throughout the sample length (Holloway, 1971). It allows modifying the temperature and pressure parameters during the experiment, making it the best choice for diffusion and decompression experiments. The main limitation of this instrument are the relatively low maximum pressure capability, due to which it is often replaced by a piston-cylinder apparatus (Holloway, 1971), and the overall complicated pressure control, often leading to pressure leaks.

The two IHPVs used for this study can reach a maximum pressure of 1 GPa and maximum temperatures of 1250 °C and 1500 °C, for the instrument in Potsdam and Göttingen, respectively. IHPVs are usually composed of (1) an outer vessel and (2) a heating system (furnace) placed inside the pressure medium and around (3) the sample holder. The furnace is subject to the same pressure conditions as the samples. The two IHPVs used in this study have a similar overall structure and arrangement, but the instrument of the University of Göttingen allows slow decompression-rate experiments, which are not possible at the laboratory in Potsdam.

Göttingen's IHPV is equipped with an automatic pressure release system, which allows much more precise control of the decompression. The IHPV is connected to a valve by which it is possible to control the opening rate and the width of the opening using a piezo-based system and computer software. This grants precise control on the decompression rate, while the pressure release in Potsdam is made

Figure 9: Internally heated pressure vessel of the GeoForschungZentrum (Potsdam). On the right side of the picture the vessel is shown in vertical working position, while on the left side, the whole pressure control system is visible, with the intensifier at the bottom.

manually by a hand valve, resulting in a more complicated control over the gas release.

The pressure vessel

The vessel is shown in Figure 9, on the right side of the picture. It is a steel vessel arranged in its vertical working position. On the contrary, the cylindrical vessel is tilted on the side when loading or extracting the sample holder, to facilitate the operations. This type of vessel (Harwood) has two openings – at top and bottom of the cylinder – and is cooled by water circulation through the body of the vessel. The IHPV is connected to the pump of the pressure medium by a system of high-pressure valves.

Argon is used as a pressure medium, chosen mainly for two reasons: at high pressure and temperatures, this gas is still able to flow within the system of valves and tubes, and – being inert – it does not react with the mechanics of the machine or with the samples (Holloway, 1971). The pressure control system (intensifier) is located between the membrane compressor and the vessel and is shown in Figure

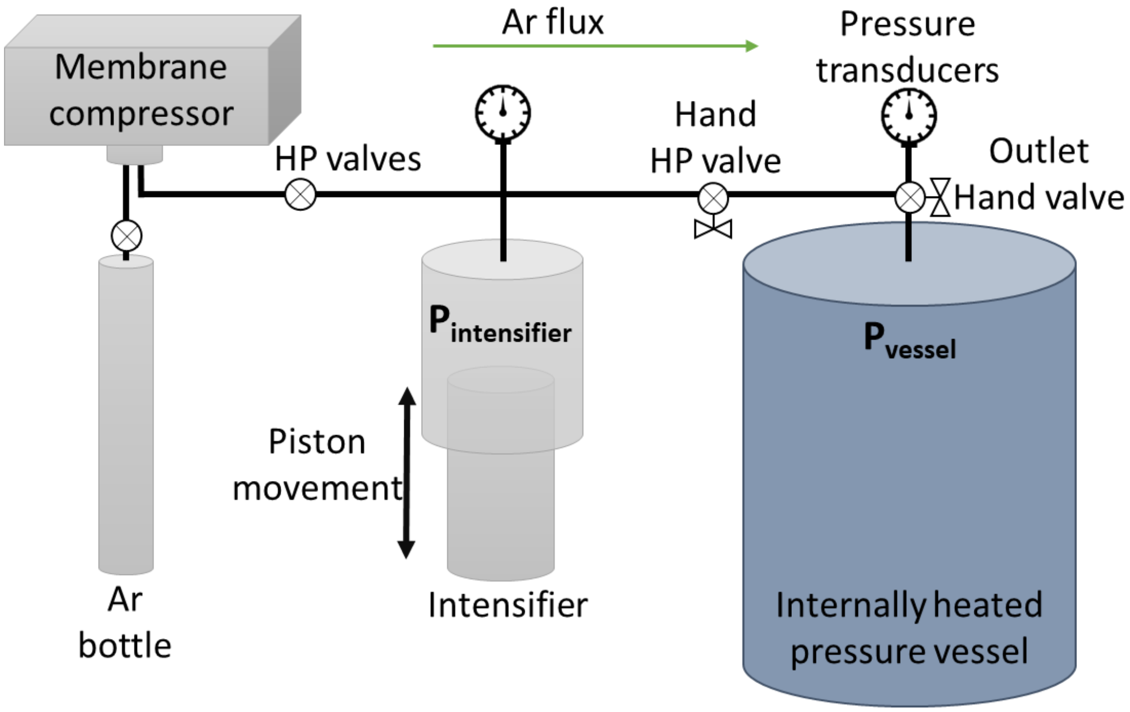

Figure 10: Pathway of the Ar gas from the bottle to the IHPV of Potsdam, through the main components of the pressure system. The two pressure transducers control the pressure in the intensifier and the IHPV.

9 (left side) and Figure 10. The intensifier consists of a separate vessel with a piston that can increase or decrease the space in which the argon is contained, thus varying the pressure in the system. When the valve between the intensifier and IHPV is open, it allows the connection of the two separate vessels, and the movement of the piston inside the intensifier can adjust the pressure inside the autoclave as desired (Holloway, 1971).

Pressure transducers shown in Figure 10 transform the gas pressure of the vessels into an electrical signal and are placed in the IHPV and the intensifier, in order to continuously control the pressure in each part of the system (Cornelius, 2006).

The heating system and temperature control

The heating system is composed of the electrical resistances that generate heat in the vessel, contained by the furnace. During the use of the IHPV, the furnace is completely immersed in argon, as the heating system is inserted in the pressure vessel. The furnace is placed around the sample holder and composed of a ceramic tube, surrounded by the two power leads (shown schematically in Figure

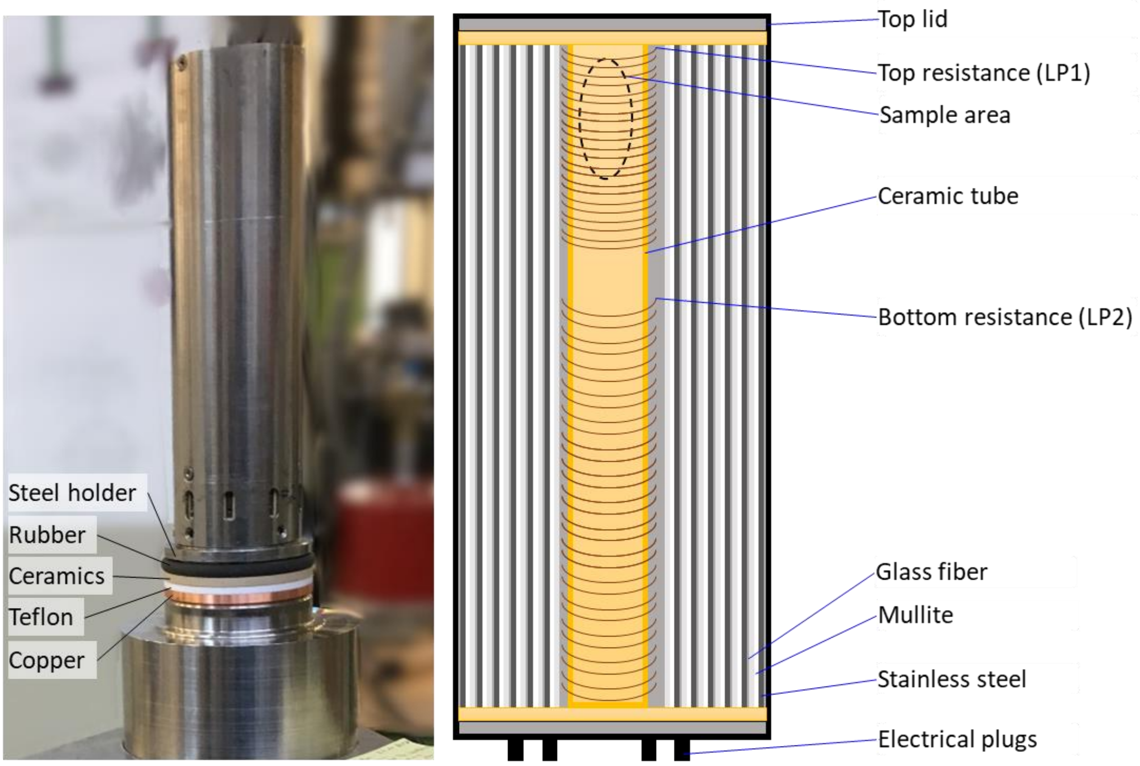

Figure 11: Picture and schematic section of the furnace element with its connection with the sample holder. The dotted area represents the sample placement inside the furnace. The sample holder is inserted in the centre of the furnace.

11). These two windings are made of highly conductive metals, molybdenum for the IHPV in Potsdam and platinum for the one in Göttingen, suited for higher temperatures (1500 °C). The bottom loop (LP2) is longer in size, compared to the top one (LP1), as it needs to provide more heating power to reach the desired temperature at the sample area, which is placed at the top of the furnace.

Around the two power leads, a series of insulation layers (usually six or seven) aims to keep the heat in the interior part of the furnace and reduce as much as possible the heat dispersion to the outside. The insulation layers are composed of mullite wool and fibre, each one of which is closed and tied up by a stainless-steel sheet. Four S-type thermocouples (Pt/Pt-Rh10) are placed in the sample area, two of which (approximately at the top and bottom of the sample) are connected to a Eurotherm PID-controller, allowing to set the power given to the two power leads, as a function of the target temperature in the sample area. The supplementary two thermocouples serve a backup for any malfunction of the primary thermocouples, and as an additional temperature control in the sample area.

The possible fluctuation of the temperature is precisely controlled throughout the entire duration of the experiments. The IHPV of the GeoForschungsZentrum in Potsdam has an overall temperature stability around ± 3 °C per minute, while the IHPV in Göttingen has temperature fluctuations around ± 10 °C per minute.

The sample holders and space capacity

Two different sample holders are available in the Potsdam laboratory are two, arranged to be used for rapid and normal quench, respectively (Figure 12). The two sample holders are composed of a ceramic tube and the electrical connections of the four thermocouples and the two electrical resistances of the heating system. Furthermore, at the base of the sample holder, the pressure seal component is located. The sealing mechanism is visible in Figure 11 and is composed of a series of rings of different materials, which interlock and prevent any gas leakage (kept lubricated by a layer of Molykote applied before each experiment). The combination of rings used for both sample holders is closed by a steel holder and composed by rubber– peek-holder–Teflon–copper, listed in order from top to bottom as in the Figure. Of these, only the peek-holder is re-used, the others are

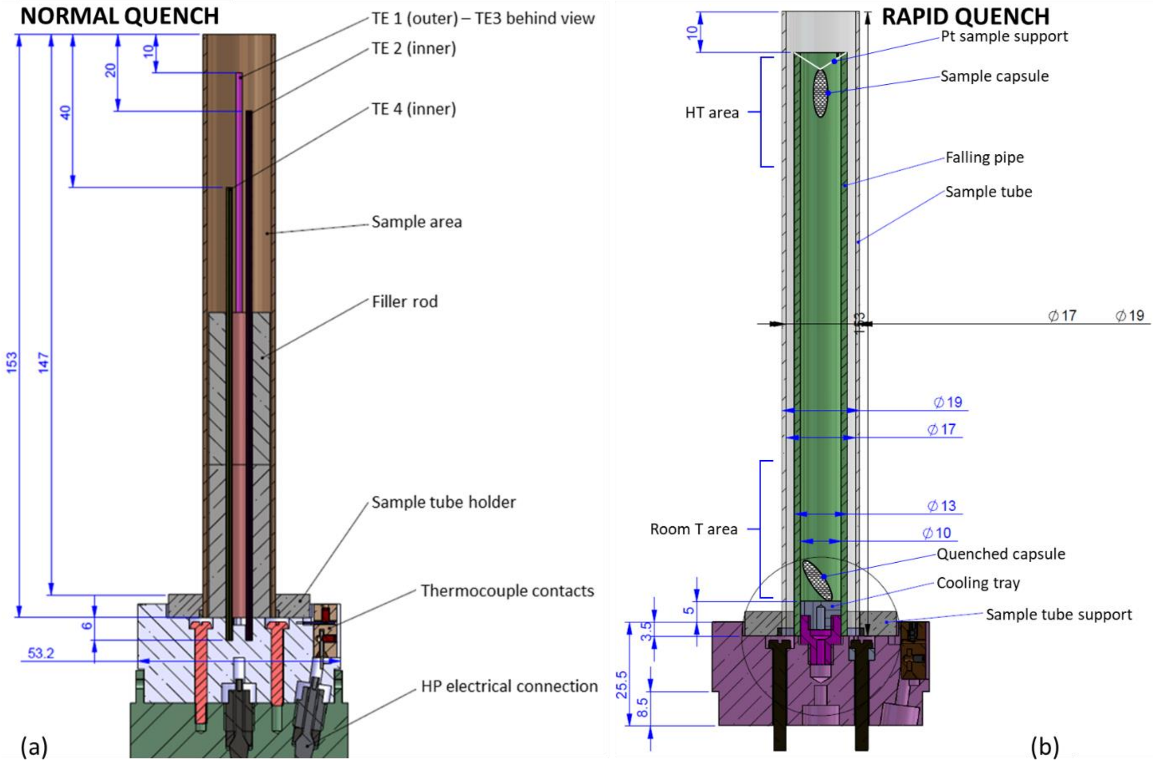

Figure 12: Sample holders of the IHPV at the GeoforschungZentrum in Potsdam (modified drawing after R. Schulz). (A) Normal quench sample holder, with the position of the thermocouples TE1 – TE4. (B) Rapid quench sample holder with the sample position before and after the quench. The fourth thermocouple (TE4, not visible in the figure) is positioned at the base of the sample holder, as a reference to monitor that the bottom area is effectively at room temperature.

going to deform by the pressure during the experiment, hence they are renewed at each new experiment.

The normal quench sample holder (Figure 12A) is provided with a series of ceramic cylinders which fill the space of the sample holder up to the high temperature (HT) area, providing a stand for the capsules inserted in the available space (filler rod in the Figure). The capacity of this sample holder is fairly big, compared to similar instruments. It is possible to insert four capsules with a diameter of 6 mm and a length of 35 mm in this sample holder.

The rapid quench sample holder (Figure 12A) has an additional electrical plug, connected to the circuit for the rapid release of the sample. In this case, two platinum supports keep the capsule suspended in the high-temperature zone, through a thin platinum wire. When the experiment is to be stopped, an electrical pulse is sent to this small circuit, causing the platinum wire to melt at the capsule level. Thus, it falls to the base of the sample holder, in this case empty (Figure 12B), into a room temperature area, but ambient experimental high pressure. The cooling rate of this rapid quench method has been estimated to be around 150 °C/s, which allows preventing the occurrence of any post-quench effects on the samples (Berndt *et al.*, 2002). This sample holder has the space capacity for only one capsule of the same length and diameter as mentioned before (6 mm diameter, 35 mm length).

3.2.1. Diffusion-couple experiments

A set of ten diffusion-couple experiments was performed in an IHPV, using a sample holder prepared for rapid quench, which assured a cooling rate of ca. 150 °C/s (Berndt *et al.*, 2002). Experiments DIFF1 to DIFF5 have been performed at the GeoForschungsZentrum in Potsdam (Germany), while DIFF6 to DIFF13 have been conducted at the Mineralogy department at the University of Göttingen (Germany). The diffusion-couple sample (Figure 8) was pressurized until a target pressure of 300 MPa, then the heating system was activated to reach the target temperature with a heating rate of 30 °C/min or 50 °C/min. Faster heating rates were impossible to apply, because the heating system of the IHPVs are extremely delicate and the risk of rupture of the internal parts of the furnace was too high. During the heating phase, the pressure is kept constant via the activation of the intensifier, which decreases the pressure when this overcomes 305 MPa. After reaching the target temperature, the experiment was either stopped (for 0-time runs) or the conditions were kept constant for both pressure and temperatures, until the end of the experiment.

The chosen temperatures varied between 700 °C and 1250 °C, with run durations between 0 seconds and 24 hours. All experimental run conditions are listed in Table 2 and will be discussed in detail in Chapter 4. The temperature was continuously controlled and registered by three S-type thermocouples (Pt/Pt-Rh) for the entire duration of the runs. Finally, the experiments were stopped with rapid quench. Afterwards, the samples were sectioned lengthwise, and embedded in EpoFix cold set epoxy in a 25.4 mm diameter mould. Each of the mounts was then polished to produce a flat sample with a <1 µm surface roughness, ready for chemical analyses of major and trace elements. Due to the presence of a chemical gradient, the conditions of pressure and temperature above the glass transition trigger the mobilization of lithium and boron between the enriched and the depleted endmembers (Chakraborty, 1995).

3.2.2. Decompression experiments

The decompression experiments were performed using the IHPV of the GeoForschungsZentrum in Potsdam and the IHPV at the Mineralogy department of the University of Göttingen for the fast and slow decompressions, respectively. An initial stage of annealing was necessary to get a complete homogenisation of the water and glass powder inside the capsules. The IHPV was therefore set at 300 MPa and 1000 °C or 900 °C for 48 hours, during which water got dissolved into the molten glass powder. After 48 hours, the pressure was slowly and steadily released, keeping a constant temperature for the entire duration of the experimental run.

In decompression experiments, it is possible to decide what kind of magmatic ascent to reproduce in the laboratory (Figure 13). In general, three main types of decompression path aimed to simulate three different kinds of magmatic ascent: an immediate ascent of the entire magmatic body (single-step), a slower but not constant ascent, with several interruptions (multi-step), or a slow and constant uprising (continuous) (Fiege and Cichy, 2015). Between single-step, multi-step, or

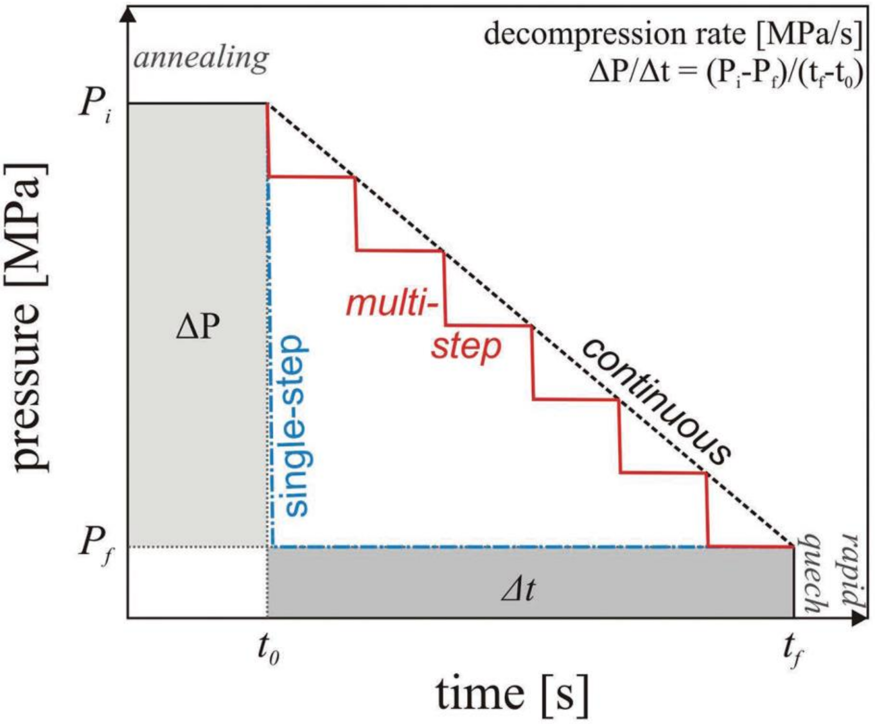

Figure 13: Schematic representation of the three main decompression modes used in this type of experiments: continuous (dashed black line), multi-step (red) or single-step decompression (blue) (Fiege & Cichy, 2015).

continuous decompression, the best suited for this study was continuous decompression, because bubbles can grow as a direct indicator of the decompression rate, which was the main focus of this study (Figure 13).

For the fast decompressions performed at the GeoForschungsZentrum of Potsdam, the pressure release was set using the intensifier to decrease the pressure inside the IHPV with a relatively controlled rate. Before the start of the decompression, the piston of the intensifier was brought in its highest position, at its minimum volume capacity. At the beginning of the pressure release, the high-pressure valve that connected the intensifier with the IHPV was opened, but the lowering system of the piston inside the intensifier was manually closed, which allowed controlling the rate at which the piston moves. Once this situation was set and stable, the pressure release effectively initiated by allowing the piston lowering of the intensifier, which was connected to the IHPV. This procedure granted a semi-automatic control on the decompression rate, as the rate of movement of the piston progressively was increased (or decreased) to adjust the pressure release, when necessary (Fiege and Cichy, 2015).

Once the intensifier piston arrived at its maximum extended position, the pressure was around 100 MPa. Then, the pressure release was continued by manually opening the outlet hand valve of the IHPV, which discharged the argon directly from the instrument. Due to difficulties with the manual pressure release, it was very hard to maintain a continuous decompression with the manual valve, because Ar tends to freeze inside the outlet tubes. For this reason, and for the risk of damaging the sample holder ceramic pieces, the decompression experiments were stopped at a final pressure of 70-78 MPa. Rapid quench was performed in order to suddenly stop the bubble formation process inside the capsule. Afterwards, the heating system of the IHPV was stopped and Ar was completely released from the machine, with a ca. 3 °C/s cooling rate, until room temperature.

This method was used for the fast decompression experiments, with duration of 30 minutes and two hours. For longer runs (five and ten hours) this approach was not applicable anymore, because the decompression rate was too low to be controlled with this technique. The five- and ten-hour decompression experiments were performed at the Mineralogy institute at the University of Göttingen (Germany). The attachment of a completely automatic valve for pressure release allows very slow decompressions (see Section 3.2 for details). Göttingen's IHPV heating system is slightly different from the one in Potsdam, therefore only experiments at 1000 °C were performed, because the instrument does not support lower temperatures (Schmidt and Behrens, 2008; Fanara *et al.*, 2017).

3.3. Analytical techniques

Every sample was mounted in one-inch round epoxy mounts and polished, to get precise measurements of the major elements as well as water contents and lithium and boron concentrations and isotopic ratios. Several different techniques have been employed in the chemical analyses of the samples. Major components and water quantification was done by using an electron microprobe and Raman spectroscopy. Lithium and boron required more sophisticated techniques, as they are trace elements and not accessible by electron microprobe, and the isotopes measurement are often very delicate analyses. In this section, an overview of these techniques as well as an example of Raman data processing will be presented, while laser ablation Inductively plasma mass spectrometry (LA-ICP-MS) and secondary ions mass spectrometry (SIMS) will be compared to evaluate each method's strengths and limitations.

3.3.1. Major elements and water content

Major elements have been analysed via a fully automated JEOL JXA-8200 electron probe micro-analyser equipped with a tungsten filament (with voltage up to 30 kV), an EDXS-detector and five wavelength separate spectrometers, available at the Geoscience department of the University of Potsdam. A fine coating of carbon was necessary to correctly ensure electrical conductivity on the sample surface. During the measurements, a voltage of 15 kV was used, with a current of 15 nA and a beam diameter of 5 µm. Calibration measurements were done on basalt and rhyolite reference glasses obtained from the Smithsonian Institution, synthetic oxides, and reference materials purchased from Astimex Ltd. The analytical counting times were either 10 or 6 seconds for the element peak and 5 or 3 seconds for the background positions. On each sample, five to eight spots of analysis were done, on the border and the core of the sample in order to verify the homogeneity of the sample (Figure 14). Finally, a first estimation of the water content was made by the subtraction of the sum of all major oxides from 100%, assuming that the synthetic glasses do not contain any other undetected components (besides Li and B whose total concentration is < 0.1 wt%).

The dissolved water content played a major role in this study. A potential water gradient between the two diffusion couples could have caused unwanted effects

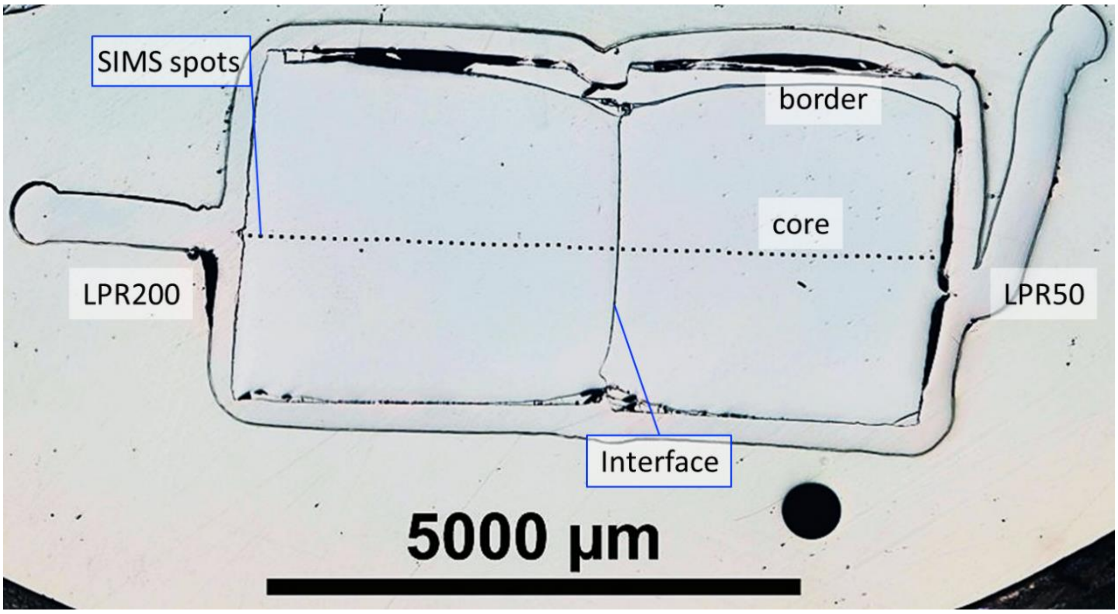

Figure 14: Example of post-diffusion sample after SIMS measurements. Microprobe analyses have been done on the border (close to the capsule) and the centre of the sample, in order to verify any heterogeneity of the samples.

on lithium and boron diffusion processes, because of their H_2O-dependent mobility. Thus, to be sure to pair LPR50 and LPR200 glasses with similar water contents in the diffusion-couple experiments (maximal difference of 0.5 wt%), analyses of the rhyolitic glass were made using micro-Raman spectroscopy across pieces of the starting glasses before the preparation of the diffusion-couple samples using a LabRAM HR 800 Raman spectrometer at the University of Potsdam.

Raman spectra were collected using a 532 nm laser and a grating with 300 lines/mm in the range 100 cm^{-1} to 4000 cm^{-1} with a three-times data acquisition for 30 seconds each. The water content was calculated following the procedure described in Behrens et al. (2006) and Schiavi et al. (2018) for rhyolitic glasses using the intensity of the OH^- bands between 3000 cm^{-1} and 3800 cm^{-1}. Along with

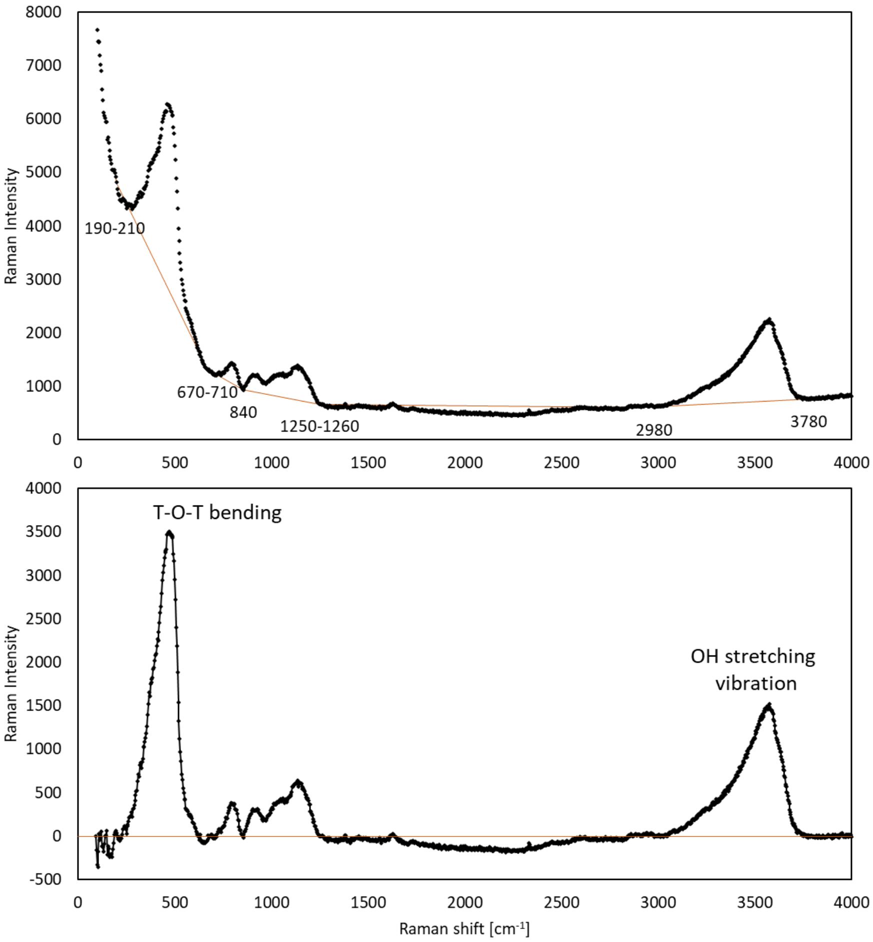

Figure 15: Example of baseline subtraction of one Raman spectrum. The top image shows a raw spectrum after measurement, while the bottom image is the same spectrum, after subtracting the baseline from the signal. The anchor points are taken from Schiavi et al. (2018) where an overview of the entire procedure is reported.

the samples, three reference glasses with known water content were used in order to define a calibration curve.

The baseline was subtracted from the spectra using the anchor points reported in Schiavi et al. (2018) and shown in Figure 15. The area A_{3550} of the OH stretching vibration peak (between 2980 cm^{-1} and 3780 cm^{-1}) was normalized to the area A_{500} of the alumino-silicate region at ca. 500 cm^{-1} (T-O-T bending), between 190 cm^{-1} and 1250 cm^{-1} for rhyolitic glasses assuming that most of the dissolved H_2O is in form of OH^- groups (Behrens *et al.*, 2006; Schiavi *et al.*, 2018).

The water content was then obtained by multiplying the ratio A_{3550}/A_{500} with the calibration coefficient obtained by the correlation of the three reference materials with known water content. Raman spectroscopy is sensitive to the temperature and environmental conditions; therefore, the reference materials have been measured several times during the day, and each day of analysis gave a slightly different correlation coefficient of the reference materials. Each sample was measured three times, and an average value was calculated and reported in this dissertation.

3.3.2. Li and B analysis, LA ICP-MS, and SIMS

Lithium and boron analysis have been challenging, especially for the measurement of their isotopic ratios. Laser Ablation Inductively Coupled Plasma Mass Spectrometry (LA-ICP-MS) and the Secondary Ion Mass Spectrometry (SIMS) of the GeoForschungsZentrum Potsdam (Germany) were the methods of choice for the trace elements analyses. The first technique presents some advantages, especially in terms of sample preparation and costs of analysis, but compared to the SIMS, it lacks in precision, and for trace elements such as lithium and boron, it is more complicated to obtain isotopes measurements, as some tests revealed in the initial stage of this research project.

To have the best results from both techniques, LA-ICP-MS was used as a preliminary study, in order to define what was the most interesting area to analyse. Once the preliminary results were evaluated, SIMS analyses were performed to get more precise measurements of Li and B concentrations, as well as their isotopic ratios.

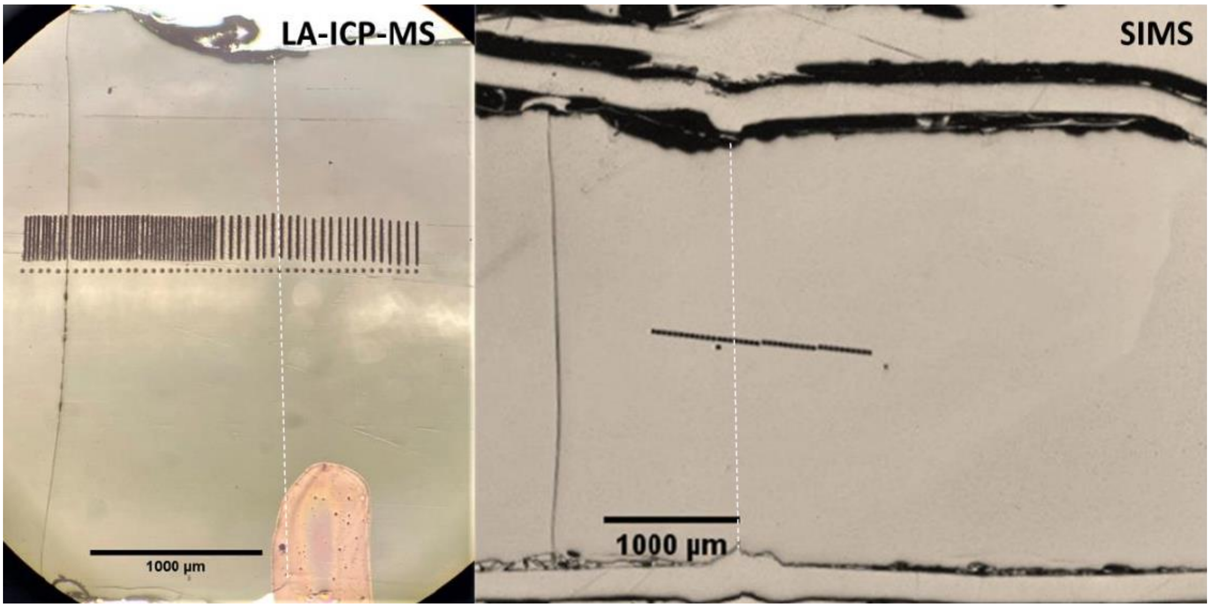

Figure 16: Pictures of LA-ICP-MS analyses (left) and SIMS analyses (right). Note, the smaller size of SIMS measurements compared to the laser ablation traces, performed in line measurements parallel to the interface area (dashed line), in the case of diffusion-couple experiment results.

In order for the LA-ICP-MS to get sufficient analytical precision in the quantification of Li and B, it was necessary to use line instead of spot measurements to have a bigger amount of material reaching the detectors (Figure 16). This generated problems in the analysis of the samples resulting from the decompression experiments, because of the limited space on the sample surface due to formed bubbles. Here, spot measurements were performed, but a minimum beam diameter of 20 µm was necessary in order to obtain sufficient analytical precision, with consequent loss of spatial resolution. In the samples obtained by the diffusion-couple experiments, there was enough space for line measurements (shown in Figure 16) with each line parallel to the interface and perpendicular to direction of the diffusion profile.

Measurements were conducted using the Analyte Excite 193 nm ArF* excimer-based laser ablation (LA) system (Teledyne Photon Machines, Bozeman, MT, USA), coupled to a quadrupole ICP-MS iCAP detector system by Thermo Scientific. The LA-system was equipped with a HelEx II two-volume ablation cell. Helium was used as a carrier gas for aerosol transport from the sample surface to the ICP ion source, having been mixed with Ar as a make-up gas before entering the plasma. Operational parameters of the ICP-MS instrument and LA-unit were tuned for maximum sensitivity, low oxide formation based on the $^{232}Th^{16}O/ ^{232}Th$ ratio and low laser-induced elemental fractionation based on the $^{238}U/ ^{232}Th$ ratio using NIST SRM 610 (Jochum *et al.*, 2011). The isotope ^{29}Si was used as internal standard and the certified reference material NIST610 for calibration of all elements.

Samples were ablated with line measurements parallel to the interface of diffusion on the sample surface, of approximately 250 µm of length and 20 µm wide. Each such profile took 30s with a repetition rate of 10Hz and an energy density of 2-3 J/cm^2 for the laser. The data processing was done using the Iolite™ software (Paton *et al.*, 2011) and the reduction scheme X_trace_elements_IS (Woodhead *et al.*, 2007); a selection was made by visual inspection of the time intervals of the signal used for concentration analysis, which corresponds to the maximum raw signal. Uncertainty estimates for the element's concentrations were based on repeated measurement of the reference materials NIST612 and BHVO-2g and are in general better than ±10 % (95% C.I.). For the lower temperature diffusion-couple experiments, LA-profiles were approximately 700 µm in length were obtained across the interface of the diffusion couple, with step size of 25 µm. For higher temperature experiments, the lithium and boron concentrations were measured along the entire length of the capsule, with step size of 150 µm.

For precise analyses of Li and B abundances, as well as their isotopic ratios, point profiles were determined using the Cameca 1280-HR SIMS at the GeoForschungsZentrum in Potsdam. A total of four SIMS sessions were conducted as part of this study: the exact analytical settings varied slightly between sessions. Prior to analyses, each mount was ultrasonically cleaned in high-purity ethanol prior to argon sputter coating that deposited a 35 nm thick, high-purity gold coating that was needed to assure electrical conductivity. All four analytical protocols used a $^{16}O^-$ primary beam operated in Gaussian mode, with a total impact energy of 23 keV, with 18 cycles per measurement. Absolute abundance values were calibrated using the two endmember synthetic glasses used in these experiments, which served as the calibration materials; these were assigned values for Li (58 and 200 µg/g) and B (180 and 600 µg/g) previously determined by LA-ICP-MS.

Isotopic ratios were not corrected for the instrumental mass fractionation, rather they are reported as delta notation referenced to the starting glass compositions. In order to improve the analytical precision, multi-collection mode was applied to lithium isotope measurements on two samples DIFF1-DIFF2. This modified approach was able to decrease the analytical uncertainty from ±1.2 ‰ to ±0.7 ‰ (1SE) as compared to mono-collection mode. A disadvantage of the static multi-collection approach is that concentration data cannot be obtained as the maximum dispersion of the 1280-HR does not allow for the acquisition of a major element reference mass (e.g., $^{28}Si^{++}$).

The relative variation of the isotopic ratio is expressed as $\delta^{7}Li$ and $\delta^{11}B$, normalized to a reference material. In this study, a relative δ value is reported, related to the reference material used to calibrate the SIMS measurements for lithium and boron concentrations and isotopic ratios. Therefore, the $\delta^{7}Li$ and $\delta^{11}B$ values were calculated based on the bubble-free starting glasses used in the experiments. The measurements made on these two pieces served also as a verification that the two endmembers had the same isotopic ratio, and that there was no analytical drift during the measurement session. The $\delta^{7}Li$ calculation was normalized with a $^{7}Li/^{6}Li$ ratio of 12.087 and δ11B with a $^{11}B/^{10}B$ ratio of 3.900.

Mono-collection Li and B contents, $^{7}Li^{+}/^{6}Li^{+}$ and $^{11}B/^{10}B$ ratios

Mono-collection analyses of Li and B on both diffusion-couple and decompression samples used a primary beam current between 0.2 to 0.4 nA which was focused to a circa 3 µm diameter spot on the polished sample surface. A 150 s pre-sputtering employing a 15×15 µm raster was used to locally remove the gold coating, suppress surface contamination, and establish equilibrium sputtering conditions.

Data acquisition employed a 4×4 µm raster, resulting in a flat-bottomed crater which helps to reduce inter-element ratio drift; this rastering was corrected for using the dynamic transfer capability of the instrument’s secondary ion optics. A 40-eV wide energy window was used to which no offset was applied. The instrument was operated at a mass resolution of M/ΔM ≈ 2000 (10% peak height) and an ETP pulse counting system, to which a synthetic 46 ns deadtime was applied based on a delay circuit in the detector’s preamplifier system. A single analysis consisted of 18 cycles of the peak stepping sequence $^{6}Li^{+}$ (15 seconds per cycle), $^{7}Li^{+}$ (3 s) $^{10}B^{+}$ (25 s), $^{11}B^{+}$ (10 s) and $^{28}Si^{++}$ (2 s). The doubly charged silicon peak at a nominal mass of 14 daltons was used to minimize the range of magnet switching while providing a major element peak at a suitable count rate. Analyses on the enriched endmember synthetic glass, which were used for calibration purposes, yielded $^{7}Li^{+}/^{28}Si^{++}$ and $^{11}B^{+}/^{28}Si^{++}$ ratios 1s repeatability of 0.44% and 0.95%, respectively, which are reasonable estimates for the data quality under these analytical conditions. The mean uncertainty for the $^{7}Li^{+}/^{6}Li^{+}$ and $^{11}B^{+}/^{10}B^{+}$ ratios on the enriched endmember glass (1SE of the 18 cycles) were 0.13‰ and 0.11‰, respectively. A single measurement took approximately 21 minutes.

Mono-collection B concentration and $^{11}B^{+}/^{10}B^{+}$ ratio

Analyses of B and B isotopes were performed on the long diffusion-couple experiments and employed a Gaussian ~10 nA $^{16}O^{-}$ primary beam which was focused to a circa 10 µm diameter at the polished sample surface. The 90 s pre-sputtering employed a 25 × 25 µm raster whereas the analyses used a 20 × 20 µm raster. A 50 V energy window was used without applying any energy offset. The mass resolution of the instrument was set at M/ΔM ≈ 2500 (10% peak height) and the ETP pulse counting system was used for ion detection. A single analysis consisted of 18 cycles using the peak stepping sequence $^{10}B^{+}$ (10 seconds per cycle), $^{11}B^{+}$ (2s) and $^{28}Si^{++}$ (1 s). The repeatability on n = 20 determinations on the enriched endmember glass had 1s repeatability for the $^{11}B^{+}/^{28}Si^{++}$ and $^{11}B^{+}/^{10}B^{+}$ of 0.13% and 0.06‰, respectively. These values provide a rough indication of the overall data quality. The typical count rate on the $^{28}Si^{++}$ mass station was 2×10^{5} counts per second and a single analysis took roughly 7 minutes.

Mono-collection Li concentration and $^{7}Li^{+}/^{6}Li^{+}$ ratio

Mono-collection measurements of Li concentration and isotopes were conducted on diffusion-couple experiments and employed a Gaussian ~4 nA $^{16}O^{-}$ primary beam which was focused to a circa 10 µm diameter at the polished sample surface. A 90 s pre-sputtering was employed in conjunction with a 25 × 25 µm raster while the analyses used a 20 × 20 µm raster. A 50 V energy window was used without applying any energy offset. The mass resolution of the instrument was set at M/ΔM ≈ 1900 (10% peak height) and the ETP pulse counting system was used for ion detection. A single analysis consisted of 18 cycles using the peak stepping sequence $^{6}Li^{+}$ (10 seconds per cycle), $^{7}Li^{+}$ (2 s) and $^{28}Si^{++}$ (1 s). The repeatability on n = 12 determinations on the enriched endmember glass had 1s repeatability for the $^{7}Li^{+}/^{28}Si^{++}$ and $^{7}Li^{+}/^{6}Li^{+}$ ratios of 0.31% and 1.40‰, respectively. These values provide a rough indication of the overall data quality. The count rate on the $^{28}Si^{++}$ mass station was 5×10^{4} counts per second and one analysis took ca. 7 minutes.

Multi-collection $^{7}Li^{+}/^{6}Li^{+}$ ratio

For many applications the Cameca 1280-HR instrument can commonly achieve analytical uncertainties of better than ± 1‰. To improve $^{7}Li^{+}/^{6}Li^{+}$ isotope ratio uncertainties analyses were repeated on the multi-collection Li and B profiles on 2 selected diffusion-couple samples using the multi-collection capability of this instrument (DIFF1 and DIFF2). The main disadvantage of the static multi-collection approach is that it does not allow for the measurement of a major element mass station (i.e., $^{28}Si^{++}$), meaning that no concentration data are obtained in this mode. This fourth and final analytical series used a ~3 nA $^{16}O^{-}$ primary beam that was focused to a circa 6 µm diameter on the polished sample surface. A pre-sputter was made for 90 s using a 20 × 20 µm raster prior to the analyses, which employed a 10 × 10 µm raster. A 50 V energy window was used without using any energy offset, and the instrument was operated at a mass resolution of $M/\Delta M \approx 2100$, which is sufficient to eliminate all significant isobaric interferences. Data were collected in EM-EM static multi-collection mode with the $^{6}Li^{+}$ count rate determined using the L2 position and the $^{7}Li^{+}$ count rate determined using the H^{2} position. Magnetic field drift was effectively eliminated using an NMR field controller. Before each analysis, automatic calibrations of both EM voltages were conducted. Under these conditions, the obtained $^{7}Li^{+}$ count rate was of 1×10^{4} counts per second on the enriched endmember glass. A single such analysis consisted of 80 individual integrations each lasting 7.5 seconds, leading to a total analysis time of 10 minutes per determination. Multi-collection provided repeatability for $^{7}Li^{+}/^{6}Li^{+}$ of ± 0.04‰ (1s) on n = 12 determinations on the enriched endmember glass; this is a reasonable estimate of this method's overall analytical uncertainty, and it indicates that the quality of the multi-collection data was circa 3 times better than was the case for the corresponding mono-collection analyses.

4. Li and B diffusivity and isotopic fractionation in hydrous rhyolitic melts

This section reports lithium and boron chemical diffusion experiments in hydrous rhyolitic melts at a pressure of 300 MPa, in the temperature interval of 700 °C to 1250 ˚C. These results are necessary for using these elements as potential tracers of dynamics in magmatic processes, such as fluid exsolution, magma mixing or differentiation, at the typical conditions down to a 10 km deep magma chamber (Huppert and Woods, 2002; Zhang *et al.*, 2010; Watson, 2017). Because these elements are fractionated significantly by the exsolution of a gas phase, the time-window of diffusion constrains the duration of the related magmatic processes such as of magmatic ascent and degassing. Hence, the established diffusivities are the basis for potential geochemical tracers of degassing-related processes.

4.1. Data processing and modelling

Diffusion coefficients (D) have been calculated using a solution of Fick's second law, for two semi-infinite diffusion couples (Crank, 1975), in the following equation describing the concentration C at a certain distance x from the diffusion interface:

$$\mathrm{C(x,t)} = \frac{1}{2}\cdot(\mathrm{C_1}-\mathrm{C_2})\,\mathrm{erf}\!\left(\mathrm{x}/(2\sqrt{\mathrm{Dt}})\right)+\mathrm{C_2} \tag{9}$$

where C_1 and C_2 are the initial concentrations of each side of the diffusion couple and t is the duration of the experiment, while erf denotes the "error function" (Zhang, 2008). The larger the value for D the faster will be the motion of the given atomic species in the diffusing medium (Figure 17A). Equation 9 was used to determine the diffusion coefficient of both boron and lithium. In the case of run DIFF13, the diffusion process reached the end of the capsule, and Fick's law had to be solved in a different way, because the boundary conditions differed from the other runs (equation 9).

$$C(x,t) = \frac{1}{2}(C_1 - C_2)\left(\operatorname{erf}\left(\frac{h-x}{2\sqrt{Dt}}\right) + \operatorname{erf}\left(\frac{h+x}{2\sqrt{Dt}}\right) + \operatorname{erf}\left(\frac{h+2l-x}{2\sqrt{Dt}}\right) + \operatorname{erf}\left(\frac{h-2l+x}{2\sqrt{Dt}}\right)\right) + C_2$$

10

Here, C1 is the initial concentration of the low-Li endmember, l is the total length of the couple, and h is the length of the low-Li endmember (Zhang, 2008).

We investigated the temperature dependence of the diffusion using an Arrhenius equation (5), already explained in more detail in Chapter 2.2. Lithium data processing needed a further step because significant diffusion already occurred during the initial heating ramp due to the high mobility of Li, indicated by the zero-time experiment (Figure 18). During the heating ramp, D is not constant and changes with varying temperature and time. To better describe the diffusion of lithium in the experiments, equation 9 was solved for $\overline{Dt}$, a product of diffusivity and time (Shewmon, 1963; Zhang, 2008). $\overline{Dt}$ is then solved with the time integrated diffusivity:

$$\overline{Dt} = \int_0^t D(\tau)d\tau$$

11

in which the diffusion coefficient D is a function of time and integrated over the entire duration of the experiment (Table 2). Time-dependent diffusion coefficients are derived from the heating history of the experiment, in combination with a pre-exponential factor (D_0) and an activation energy (E_a) of diffusion from the Arrhenius relations.

$$D(\tau) = D_0 \exp\left(\frac{-E_a}{RT(\tau)}\right)$$

12

In equation 12, $T(\tau)$ is the heating history. In practice, $\overline{Dt}$ of all Li diffusion experiments are fitted simultaneously for the best E_a and D_0 minimizing the weighted sum of the squared residuals, correcting the values obtained using equation 9 and equation 10. It should be noted that this correction tends to affect experiments conducted at higher temperature more towards lower diffusivity values, for the same heating rate and duration.

Isotopic fractionation was modelled by calculating independently the diffusion coefficients for the concentration profiles of the two isotopes. By relating the two

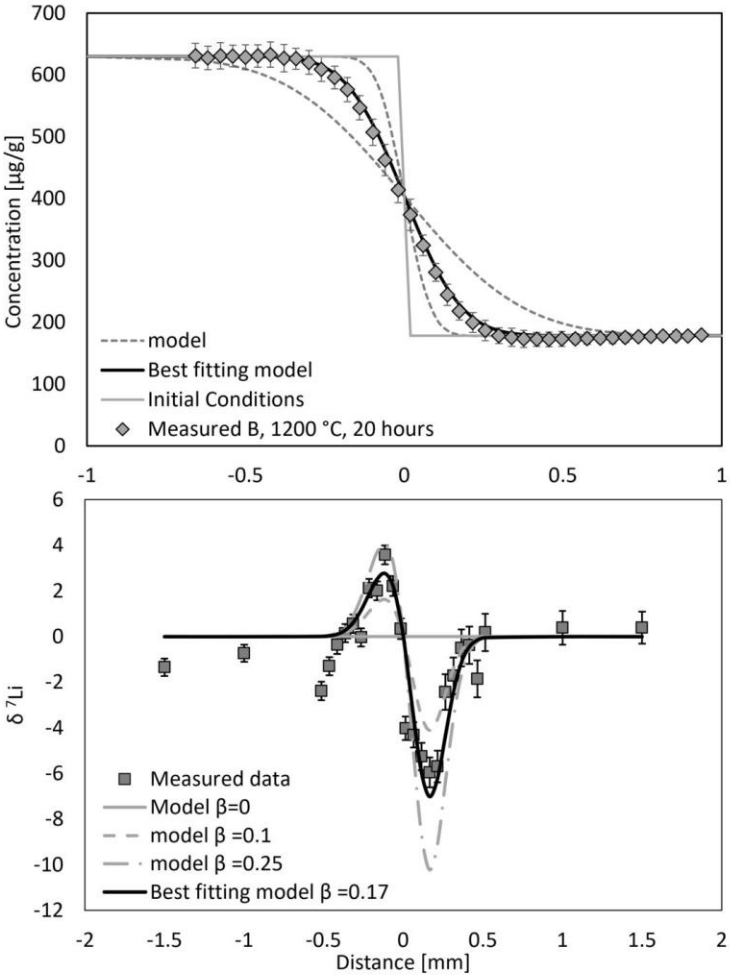

Figure 17: Example of model fitting of a concentration profile (A) and an isotopic fractionation profile (B). The grey solid line in both plots represents the initial profile, while the dotted lines show intermediate profiles as a function of variable D, for the concentration profiles, and β for the isotopic fractionation model. The black line reports the best fit line, and the interface is placed at distance 0.

diffusion coefficients, the coefficient β was obtained using equation 8, illustrated in Chapter 2.2 (Richter *et al.*, 2003). Using this approach, the profiles of two isotopes can be used for solving both diffusivity and β. The effect of β on the δ^7Li is shown in Figure 17B, going from a value of 0, when there is no difference between the diffusivities of the two isotopes, to a value of 0.25, where the amplitude of the sinusoidal curve increases. The length of the profile affected by isotope fractionation is a function of the time-window during which the diffusion process is active.

All curve-fitting described above (Figure 17A and Figure 17B) was done using the programming language Python[1] by minimisation of the weighted sum of the squared residuals, in which the weights correspond to a reciprocal of the squared

---

[1] https://www.python.org/

uncertainty ($1/\sigma_{se}^2$). Furthermore, the Monte Carlo integration method for the error propagation was used to propagate the uncertainty of measurements to the final fit parameters. This is performed by repeating the curve fit and allowing a variation of concentrations with random sampling of a Gaussian distribution based on the observed experimental standard deviation (e.g., Anderson 1976) including the analyses of the major elements before and after the experiments. The small error given by their standard deviation demonstrates that the overall composition of the samples remains constant even after the experiments. The homogeneity of the samples has been verified by repeated measurements traversing from the core to the rims and the complete length of the glass cylinders.

4.2. Results

Measurements of lithium concentrations in two diffusion couple experiments are shown in Figure 18A. The two runs DIFF1 and DIFF2 were both performed at 700 °C for 0 seconds and 30 minutes, respectively. The length of the diffusion profiles reflects the different durations of the two experiments, where the longer profile is from the longer duration run.

Table 2: experimental conditions and diffusion coefficients for the diffusion-couples

Sample	T [°C]	Duration[2] [s]	Heating rate [°C]	D_{Li} [m²/s]	β_{Li}	D_B [m²/s]
DIFF1	700	0 (785)	50	$1.23\times10^{-10} \pm 8\times10^{-11}$	0.17 ± 0.02	-
DIFF2	700	1800 (785)	50	$7.57\times10^{-11} \pm 4\times10^{-11}$	0.18 ± 0.02	-
DIFF3	800	1800 (905)	50	$3.50\times10^{-10} \pm 5\times10^{-11}$	0.15 ± 0.02	-
DIFF5	1000	0 (1145)	50	$8.67\times10^{-10} \pm 2\times10^{-10}$	0.19 ± 0.04	-
DIFF10	1200	0 (2205)	30	$1.44\times10^{-9} \pm 5\times10^{-10}$	0.15 ± 0.02	-
DIFF13	1050	900 (1905)	30	$9.46 \times10^{-10} \pm 2\times10^{-10}$	0.20 ± 0.02	-
DIFF6	1000	86400 (-)	30	-	-	$2.4 \times 10^{-14} \pm 3 \times 10^{-15}$
DIFF7	1100	72000 (-)	30	-	-	$6.0 \times 10^{-14} \pm 9 \times 10^{-15}$
DIFF8	1200	72000 (-)	30	-	-	$1.5 \times 10^{-13} \pm 1 \times 10^{-14}$
DIFF12	1250	72000 (-)	30	-	-	$2.6 \times 10^{-13} \pm 2 \times 10^{-14}$
Activation energy E_a [KJ/mol]				57 ± 4		152 ± 15
Pre-exponential factor D_0 [m²/s]				1.53×10^{-7}		3.80×10^{-8}

---

[2] Numbers in brackets report the heating ramp time, which was summed with the duration of the experiment where the temperature was kept constant. DIFF10 and DIFF13 have significantly higher heating ramp times, because of the lower heating rate used during the experiment

Significantly, DIFF1 shows that a diffusion profile is already present in an experiment that was immediately stopped after reaching the target temperature (zero-time experiment), indicating that the diffusion process started during the heating ramp, before reaching the final run-temperature (from 50 °C to 700 °C). Possible analytical convolution effects were considered not significant using the SIMS instead of the LA-ICP-MS analysis method, having a significantly narrower beam size (3 µm and 20 µm, respectively). This considerably reduces the error relative to the amount of matter analysed, and the effect of analytical convolution that could be generated by this type of analysis (Bradshaw & Kent, 2017; Jollands, 2020).

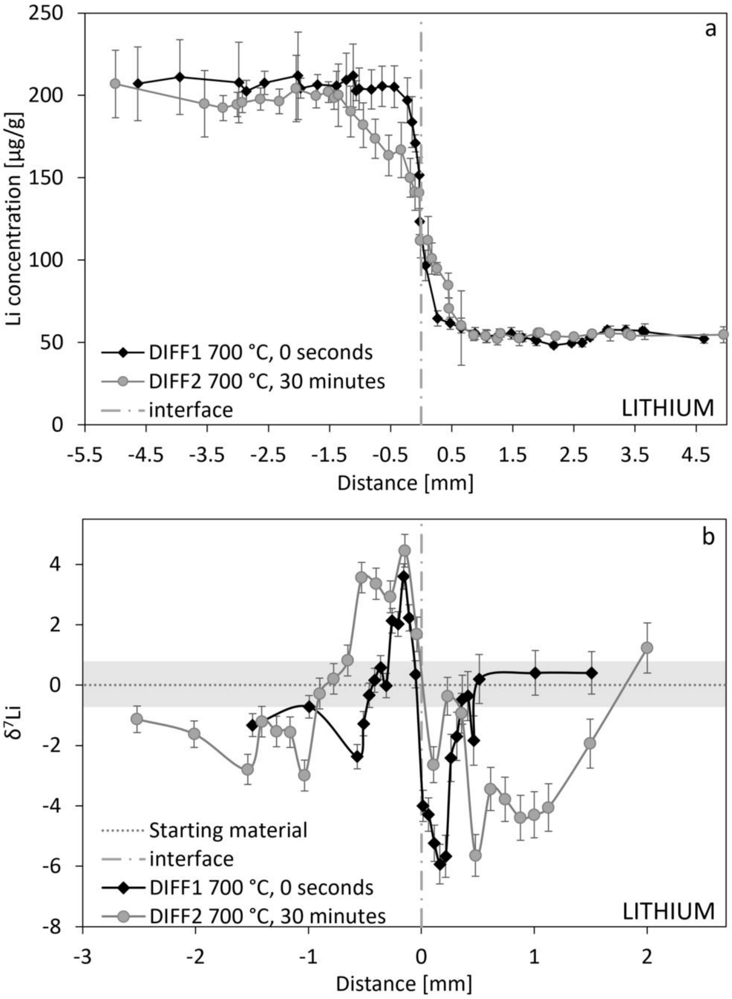

Figure 18: (a) SIMS lithium concentration profiles of the samples DIFF1 and DIFF2, shown in black and grey, respectively. The dashed vertical line represents the original contact surface between the two glasses. The only difference between the two experiments is the duration, being 0 seconds for DIFF1 and 30 minutes for DIFF2. (b) SIMS δ^7Li isotope profiles between the two experiments show that the wider sinusoidal shape is a result of the diffusion progression. The grey area represents the uncertainty of δ^7Li of the starting material.

Lithium diffusion not only is extremely fast (Richter et al., 2003; Holycross et al., 2018), but also starts at low temperature. Taking this diffusion character into consideration, diffusion coefficients are determined and reported in Table 2, and the lithium data yielded an activation energy E_a of 57±4 kJ/mol and a pre-exponential factor D_0 of 1.53×10^{-7} m^2/s (complete diffusion profiles of all samples are shown in Appendix A1).

The diffusion-induced isotopic fractionation is shown in Figure 18B, where the δ^7Li of the samples DIFF1 and DIFF2 are shown. The significantly different mobilities of the two isotopes results in a sinusoidal curve, which had also been reported by Richter et al. (2003) and Holycross et al. (2018). In this study β values

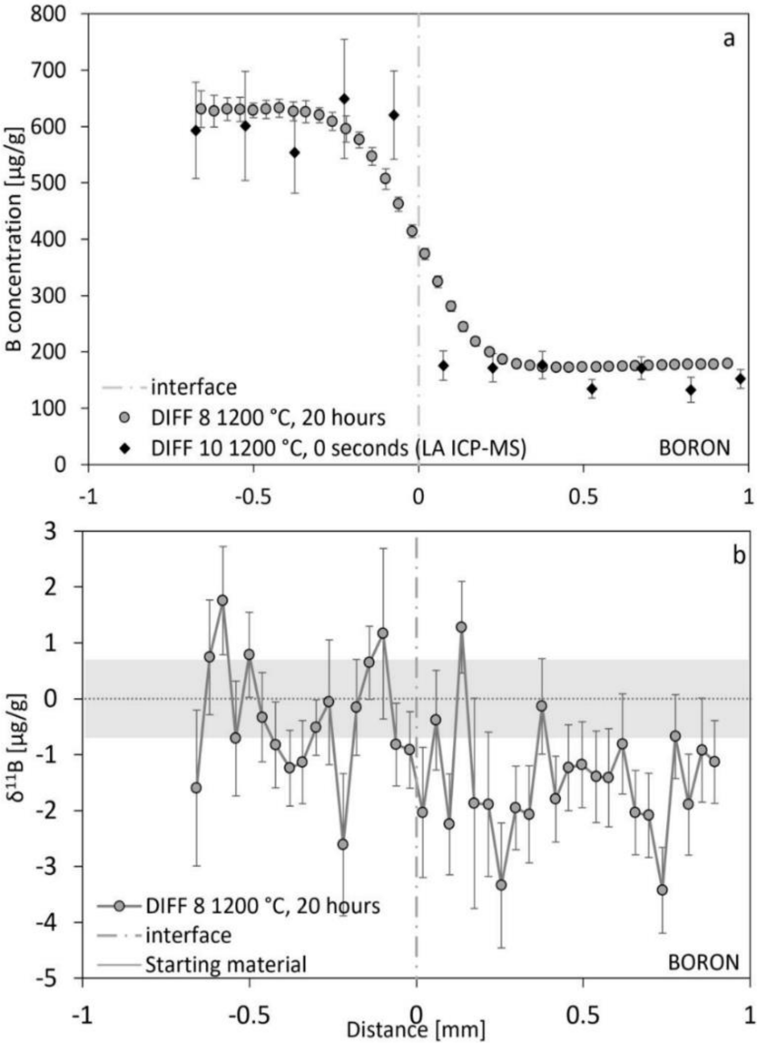

Figure 19: (a) Boron concentration profile of two experimental runs, DIFF8 and DIFF10, with respective durations of 24 hours and 0 seconds, both performed at a temperature of 1200 °C. SIMS measurements were not done for DIFF10. The results of Laser Ablation ICP-MS detected no diffusion, and therefore high-resolution SIMS analysis were considered unnecessary. (b) δ^{11}B isotope profile of the sample DIFF8 analysed by SIMS. The grey area represents the average value of the starting material, used as reference during the measurement sessions. There is a slight decrease in the δ^{11}B in the right part of the profile, corresponding to the low concentration endmember.

were calculated, resulting in the range 0.15 – 0.20 (Table 2), following equation 8. The range of isotopic variation is constant regardless of the experimental parameters (Figure 18B), because it is only controlled by the β coefficient. As it was the case for the concentration profiles, the length influenced by the diffusion (i.e., diffusion front) changes with the duration of the experiment. The longer the run duration, the further the spread of the sinusoidal curve along the length of the capsule.

In contrast to the behaviour observed for lithium, boron is a significantly slower moving element. Figure 19A shows the results of two different diffusion-couple experiments, both at 1200 °C, with duration of 0 seconds and 24 hours, respectively. Differently from lithium, the length of the diffusion profile is visibly shorter, and the zero-time experiment produced no diffusion in the sample. With this observation, it was ascertained that the heating ramp of the sample did not affect the diffusion of boron. Overall, the results on boron at all conditions resulted in an activation energy of 152 ± 15 kJ/mol and a pre-exponential factor of 3.80×10^{-8} for the Arrhenian relation (Table 2)

The isotopic results of B show profiles that are not as distinct as those for lithium isotopes. In Figure 19B no clear trend is recognized and instead, the right-hand side shows a very slight decrease of $\delta^{11}B$. Note that the boron diffusion flux was from left to right (from the high-concentration endmember on the left, to the low-concentration endmember on the right).

Experiment DIFF13

The experiment DIFF13, performed at 1050 °C for 15 minutes was the result of a machine malfunction. The experiment was planned to be for boron diffusion, at 1150 °C for 24 hours, but during the heating phase the temperature topped at 1050°C and the heating system showed a malfunction after 15 minutes during which the temperature remained stable. It was not possible to continue this experiment, therefore it was interrupted to not damage the internally heated pressure vessel.

The time duration and temperature of this experiment was not planned, and the experiment was certainly too short to produce any diffusion for boron. Nevertheless, it was long enough for triggering lithium diffusion. Indeed, a diffusion

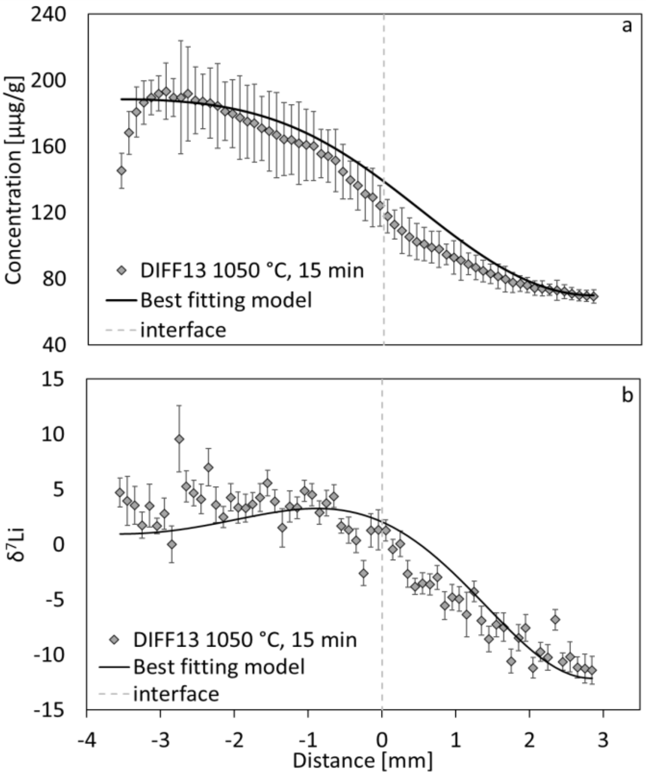

Figure 20: Concentration profile (a) and δ^7Li profile (b) of the experiment DIFF13. The black line is the best fitting model, while the dashed line represents the interface between the two endmembers. The left edge of the concentration profile presents a steep decrease in the lithium concentration values. This can be caused by the interaction with the Pt capsule. This effect was not detected in any other experiment.

profile was visible (Figure 20), and the determination of the diffusion coefficient was still possible, but the time and temperature of the experiment caused lithium diffusion to reach the end of the capsule. In this case, the semi-infinite model used for the other profiles was incorrect, and the concentration profiles were modelled following a different version of the concentration equation (10). The sinusoidal trend in the isotopic ratio was hardly recognisable, as it was stretched to the length of the entire capsule. By modelling the two isotopes separately, it was possible to obtain a β value using the same method as for the other profiles.

4.3. Discussion

4.3.1. Lithium and boron diffusivities

Figure 21A and Figure 21B shows an Arrhenian diagram documenting the temperature dependence of the diffusion coefficients for lithium and boron as determined in this study. Clearly lithium is a significantly faster diffusing element than boron. In the silicate composition used in this experiment, boron acts as a network former, usually present in tetrahedral or trigonal coordination with oxygen (Dell and Xiao, 1983; Angeli *et al.*, 2010; Bista *et al.*, 2016). Its bonds are similar to silicon in terms of strength; therefore, a large amount of energy is needed to first break bonds prior to commencing the diffusion process. Conversely, lithium resides in the interstices of the silicate network, and hence diffusion can occur even at very low temperatures below the glass transition.

In addition, water in silicate melts is a very efficient network modifier of the melt structure (Mysen and Richet, 2019), facilitating the rupturing of oxygen bonds between network-forming ions, which leads to an increased mobility of both Li and B. In Figure 21A and Figure 21B it is apparent that the diffusivity studied here is higher than that measured in dry systems (Jambon and Semet, 1978; Cunningham et al., 1983; Baker, 1992; Chakraborty et al., 1993).

<u>Lithium.</u> On the Arrhenian diagram (Figure 21A) the data form a linear trend except for one outlier at 700°C from run DIFF2. It is unclear why this experiment at 700°C did not fit the overall pattern, as no irregularities were detected during run DIFF2. Generally, data at 700°C have a higher uncertainty due to the stronger impact of the heating ramp on the overall diffusion. If the value of DIFF2 is an outlier, the activation energy for Li diffusion in hydrous rhyolite is 57±4 kJ/mol from linear regression, including the datum in the regression would yield an activation energy of 65±6 kJ/mol. It was concluded that 57±4 kJ/mol is likely the true activation energy, since it is more coherent with the systematics compared with previous experiments, for example the relation of the activation energy to the water content, explained below.

In Figure 21A this work is presented alongside the results from Cunningham et al. (1983), Jambon & Semet (1978), and Holycross et al. (2018). Of these three studies, the first two focused on anhydrous melts, while only Holycross et al. (2018) investigated Li diffusion in hydrous silicate melts. The activation energy reported in this dissertation is indeed lower than the two anhydrous studies (90 ± 24 to 84 ± 12 and 72 ± 4 to 96 ± 3 kJ/mol from Cunningham et al., 1983 and Jambon & Semet, 1978, respectively). Furthermore, the activation energy is higher than that reported for hydrous rhyolite, given by Holycross et al. (2018), which results in 39±3 kJ/mol at 6 wt% H_2O. This difference is coherent with the expected effect of H_2O on the diffusion process and is related to the change of melt structure with increasing H_2O. It is therefore expected that lithium diffusion is highly sensitive

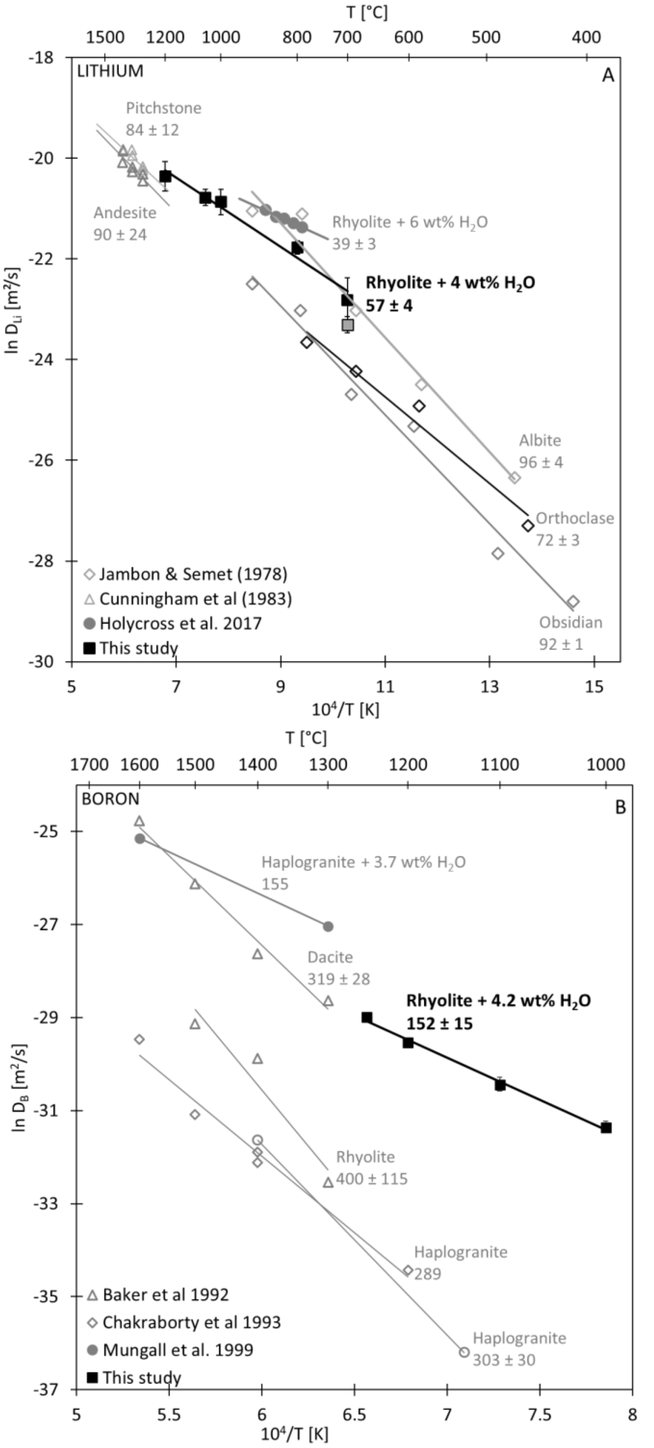

Figure 21 Arrhenius relations of lithium (A) and boron (B) diffusivity of this study, compared to the available data on lithium mobility in silicate melts. All data reported with empty symbols are showing studies performed on dry silicate melts while filled circles represent data from (A) Holycross et al. (2018) and (B) Mungall et al. (1999) investigating wet rhyolitic glasses with a H_2O content of 6 wt%. and 3.7 wt%, respectively. Activation energies reported for each dataset highlight that in hydrated silicate melts, the diffusion of lithium and boron is enhanced and proceeds faster than in the case of a dry matrix.

to the water content of the melt system.

Compared to other trace alkaline elements, lithium has the smallest ionic radius, and this leads to a very fast diffusion rate. For instance, trace level rubidium with a considerably larger radius, has been determined to have an activation energy of 127±2 kJ/mol in dry rhyolite (Zhang et al., 2010), with a diffusivity that approaches that of boron at a given temperature, rather than that of lithium. Water lowers rubidium's diffusion coefficient but does not affect its activation energy value. In contrast to lithium, water dissolved in a silicate melt produces a vertical shift in the Arrhenius relation of Rb, decreasing only the pre-exponential factor of Rb (Zhang et al., 2010), but remaining almost constant in terms of activation energy.

Boron. The diffusion results have been compared with previous studies of Le Losq et al., (2012), Baker (1992), Mungall et al. (1999) and Chakraborty et al. (1993); these are plotted in the Arrhenius diagram in Figure 21B. As compared to the result on hydrous melts reported by Mungall et al. (1999), the activation energy value of this study differs only by 3%. Mungall et al. (1999) performed experiments at 1 GPa, while these experiments were conducted at 300 MPa. This may explain both the ca. one order of magnitude disparity between the absolute D values and the significant difference in the pre-exponential factor of the Arrhenian fit (3.80×10^{-8} vs 2.51×10^{-7}). Despite this overall agreement, it is noted that Mungall's study only reports data obtained at two temperatures, and thus a comprehensive evaluation on the differences between the two datasets is not possible.

Through the comparison with the studies of Baker, (1992) and Chakraborty et al. (1993), it is clear that boron activation energy decreases strongly with increasing water content in a system, which is similarly to the case for lithium (Figure 21). Boron is a network former and coexists in silicate melts in either trigonal or tetrahedral coordination. The trigonal coordination is likely the dominant species in highly silicic melts, likely accommodating an extremely high percentage of the total boron. Schmidt et al. (2004) verified that the presence of water enhances boron tetrahedral coordination species from 2% to 6% in metaluminous silicate melts. Nevertheless, a significant decrease in the activation energy of boron is observed in the presence of water, meaning that the change in coordination of boron is less important than is the decrease of the viscosity of the melt by the water content (see below). These results have been compared with the study of Chakraborty et al. (1993), where boron diffusion was investigated in a borate-silicate glass couple. That study shows strongly asymmetric profiles, related to the interdiffusion of boron and silicon in opposite directions. Because boron was a major element in that study, the mass flux of boron going in one direction has to be balanced by a silicon flux in the opposite direction. In contrast, concentration dependent diffusivity was not observed in these experiments (i.e., strongly asymmetric profiles were not found), presumably because boron is only a trace element: the trace quantities of B were too insignificant to change the bulk melt structure. Furthermore, no interdiffusion of Si was noticed in this study, as was the case for Chakraborty et al. (1993), because here the melt compositions of the diffusion couple were identical except for B.

4.3.1.1. Impact of water concentration

Water content has a major influence on both lithium and boron diffusion in silicate melts. Therefore, the water effect was investigated in more detail related to their diffusivity, which mostly involves shifts in the activation energy. The main focus of this section is whether a quantitative relationship between water content, melt composition and lithium and boron mobilities can be defined.

Ross et al. (2015) investigated lithium conductivity in aluminosilicate glasses. They stated that Li diffusion is so fast because it creates a percolation path that does not affect the structure of the silicate melt. At every jump of one Li cation to another site, an interstitial void with a negative charge potential is created and this is immediately occupied by another lithium positive cation. This could be facilitated if the melt is hydrated, as water is known to disrupt the short-range order of the glass (Le Losq et al., 2015).

Based on the available studies of the effect of melt composition on the lithium diffusivity (e.g., Ross et al., 2015), the activation energy was plotted as a function of NBO/T, which represents the number of non-bridging oxygens per tetrahedral cation (Figure 22A). This value was calculated following Mills et al., (2014) and it approximately describes the degree of polymerization of a glass. Water is well known to be a network modifier in silicate melts, generating non-bridging oxygens in the silicate structure, thereby increasing the NBO/T value. However, it has to be kept in mind that this value represents a simplified model that sorts cations according to simple rules. Furthermore, the ratio of molecular H_2O to OH^- groups in silicate melts is temperature dependent, which is not accounted for in the calculation procedure (Stolper, 1989).

In Figure 22A a scatter is seen in the available data from the various studies. Within the scatter, the obsidian of Jambon & Semet (1978), the pitchstone of Cunningham et al. (1983) and the two rhyolites by Holycross et al. (2018) and this study form an exponential trend. The activation energy decreases exponentially with increasing NBO/T, which is related to the water content. This trend appears to be valid only for melts with similar compositions. It is likely that the approach

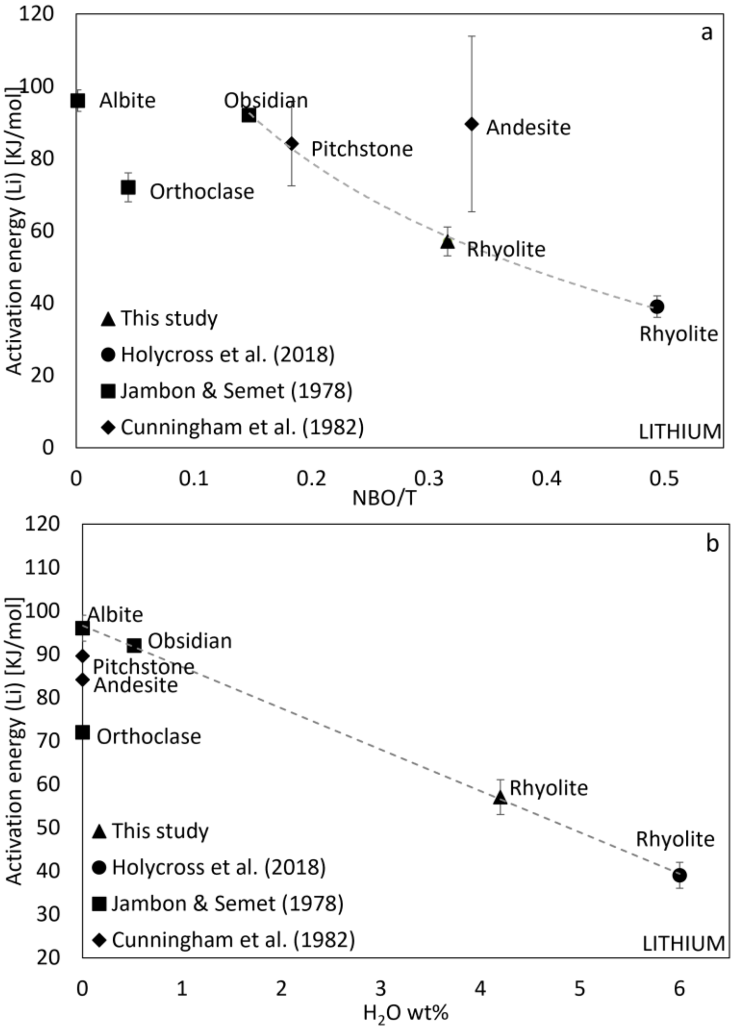

Figure 22: (A) Activation energy of lithium diffusivity as a function of the composition of the glass, with respect to NBO/T values. For melts with significant compositional differences, there is a scatter in the dataset. (B) Activation energy of lithium as a function of the water content of the studied glasses. For glasses with the same composition, the activation energy decreases linearly with the increase of water concentration. In dry conditions, the major element composition of the glasses causes a scatter in the activation energy values.

based on the concept of NBO/T does not adequately account for significant differences in major elements, as highlighted by the misalignment of the datapoints with strongly dissimilar chemical composition (albite, andesite, orthoclase).

As an alternative, the activation energy of lithium was plotted against the water content (Figure 22B). Figure 22B shows that the activation energy of lithium diffusion correlates linearly to the water content of the melt. This property is particularly evident for the obsidian, the two rhyolites and the anhydrous albite glass. However, for those cases employing dry silicate melt, there is a spread of the datapoints with a significant variability in the reported activation energies. This is because even if lithium does create a percolation pathway, as proposed by Ross et al. (2015), the bulk composition of the host medium nonetheless will play a significant role in lithium diffusion, especially when no water is dissolved in the melt. In addition, there could be some uncertainty related to the analytical precision of the major element measurements in the dry melts. Further, water contents have not been reported for all data considered in comparison to this study, leading to possible uncertainties, though the observed scatter is too large to be explained solely by such an effect.

The diffusivity of boron determined experimentally in this study was compared with values determined by the Eyring relation, using a jump distance of 0.3 and the viscosity calculated with the models described by (Schulze et al., 1996) and (Giordano et al., 2008). Figure 23A shows the Arrhenius relation of the three datasets, showing that overall, the experimental results are in good agreement with the two sets calculated from the viscosity models. The diffusivity obtained using the viscosity calculated according to Schulze et al. (1996) results in similar linear trend and similar activation energy (164 kJ/mol). A small shift is noticeable between the two datasets (difference ln D = 0.5) which might be attributed to the differences in the composition of the two glasses: haplogranitic in the case of Schulze et al. (1996) and rhyolitic for this study (Table 1).

Using the viscosity calculated according to Giordano et al. (2008), the diffusivity data are in good agreement at high temperature (1200 °C – 1250 °C) but the model deviates with a steeper slope and consequently a higher activation energy at lower temperatures (Figure 23A). The model of Schulze et al. (1996) was calibrated using a set of hydrous haplo–granitic samples, which were very close to the rhyolitic composition of this study, while the model of Giordano et al. (2008) was calibrated using a wide spectrum of compositions.

Nonetheless, the good agreement of these results with the Eyring equation (6) allows us to consider boron diffusion as primarily controlled by the viscous flow dynamics (Mungall, 2001), and thus the activation energy determined for the viscosity can be used for boron diffusion, as well as its relation to the water content of the silicate melt (Schulze et al., 1996). Figure 23B shows the activation energy of boron diffusivity determined by both this study and existing literature as a function of water content and compares this diagram with the corresponding data

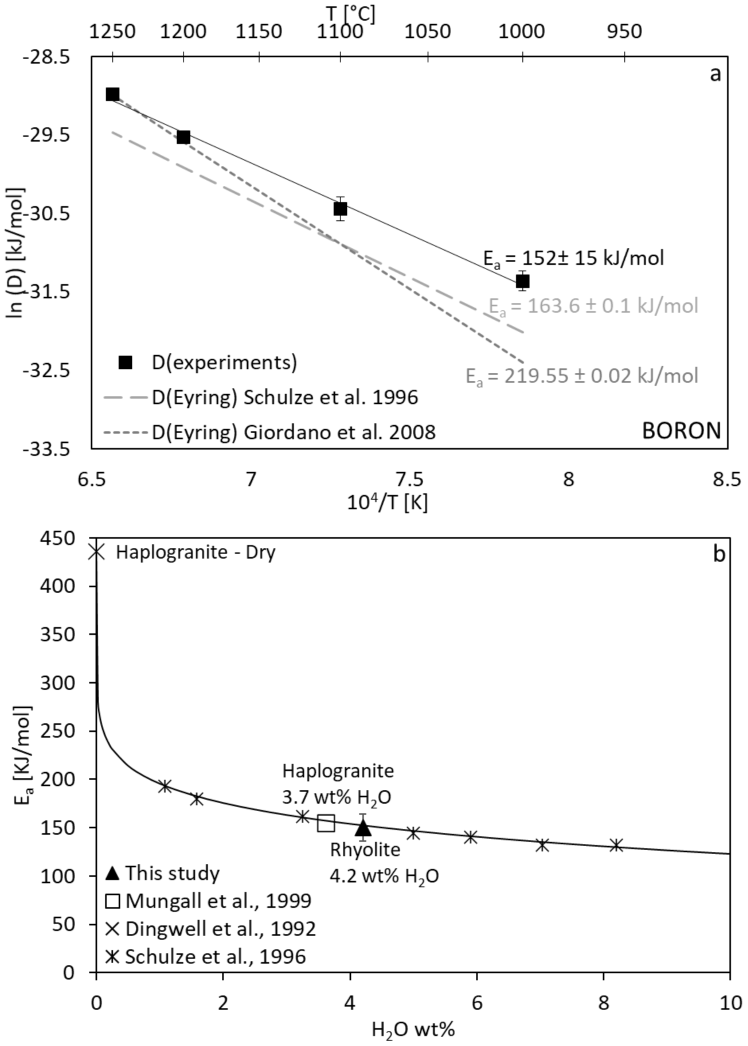

Figure 23: (A) Arrhenius relation of this study in comparison with the values obtained by the Eyring equation. Two different viscosity estimations were used, by Giordano et al. (2008) and Schulze et al. (1996). (B) Boron activation energy as a function of water content. The overall agreement of the two models (especially Schulze et al. 1996), with the experimental data indicates that boron diffusion is a process of viscous flow (Mungall, 2001) and allows to compare E_a with E_a from Schulze et al. (1996). The data from this study and from Mungall et al. (1999) show exceptional agreement with the plot from Schulze et al. (1996).

of Schulze et al. (1996). Figure 23B reports that the two datasets are in an exceptionally good agreement. The two points of this study and Mungall et al. (1999) corresponding to measured diffusivities lie perfectly on the trend line defined by Schulze et al. (1996), confirming that the presence of water strongly affects the mobility of boron, and that B diffusion is limited by viscous flow, especially for water contents below 1wt%, while for increasing water concentrations, the effects on boron mobility is still significant, but less pronounced.

4.4. Isotope fractionation

As introduced in Chapter 2.2, due to their mass difference, isotopes of an element diffuse at different rates in the same medium, generating isotopic fractionation. The diffusion-couple experiments determined β values between 0.15 to 0.20 for Li but detected no significant isotope fractionation for boron (i.e., incalculable β values). When Li diffuses, ^{6}Li moves faster than ^{7}Li, resulting in a low δ^{6}Li on the low-concentration, and an elevated δ^{7}Li for the high concentration side of the profile (Figure 19B). At the edges of the two endmembers, far away from the interface area, the isotope ratios remain undisturbed. Thus, the diffusive fractionation generates a sinusoidal curve for the isotope ratio across the interface, where β values can be determined by fitting equation 8.

Figure 24 reports the coefficient β as a function of the diffusivity of the element normalized to the diffusivity of silicon, to compare lithium with several other cations, such as Ca, Mg and Fe (Watkins et al., 2009, 2017; Holycross et al., 2018). D_{Si} was calculated following (Baker and Bossányi, 1994). The β values are lower than those determined previously by Holycross et al. (2018), and Richter et al. (2003) but higher than was the case for many other elements.

It is generally considered that the more freely an element can migrate in a medium, the closer β approaches the value for ideal gas of 0.5 (Richter et al., 2003). Because lithium is a small cation which does not bond with the tetrahedral network, it is coherent to find that the β values of all three studies (including this) were higher than for other cations, even though the experiments used quite different designs. For example, the first report of β was determined by a diffusion couple experiment with a natural rhyolite and a lithium-doped natural basalt, performed under dry conditions at 1.2 – 1.3 GPa, 1300 – 1350 ˚C (Richter, 2003). That study reported β = 0.215, which is distinctly higher than the results of this study (from 0.15 ± 0.02 to 0.20 ± 0.02). The different experimental designs are suspected to be the main cause of the disparity. Furthermore, in Richter et al. (2003) multi-component exchanges occur simultaneously with Li diffusion due to the basalt–rhyolite couple. Silicon is likely one of the diffusing species for a basalt–rhyolite couple, and therefore the value of D_{Li}/D_{Si} should have varied during the progress of diffusion. That means, the β point for Li reported by Watkins et al. (2003) would have shifted from lower to higher values (Figure 24).

In this study, the diffusion within the couple is only driven by the chemical potential gradient of Li (i.e., both halves of the diffusion pair had the same matrix composition) reaching almost the condition of a tracer or even self-diffusion process. The study of Holycross et al. (2018) conducted similar experiments to this study and reported a β value of 0.228. A notable difference between the two experimental setups was the content of initial water dissolved in the silicate melt: 4.2 wt% for this study and 6 wt% for Holycross et al. (2018). While the differences between the isotope diffusivities is explained by differences of melt properties due to temperature and water content, we are not aware of any model relating the

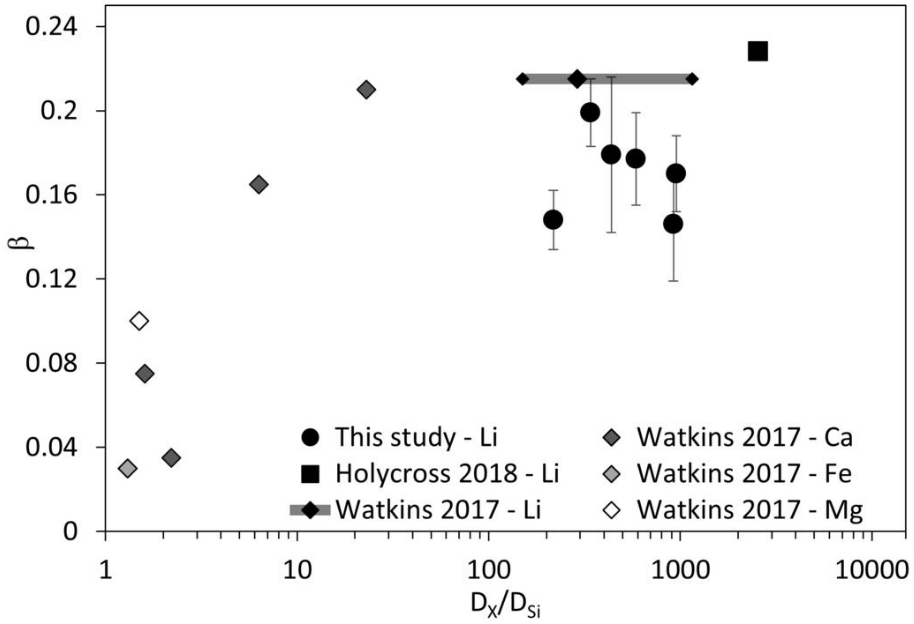

Figure 24: β coefficient of an element X as a function of its diffusivity, normalized to the silicon diffusivity (plot modified after Watkins et al., 2017; Holycross et al., 2018). D_{Si} was calculated using the method of Baker and Bossányi (1994). For the study by Richter et al. (2003), Watkins took an average value of the diffusivity of silicon, as it migrates from higher to lower value, during the progress of diffusion between rhyolite and basalt. In this plot, the likely range for Si diffusivity is indicated, with the black diamond symbols at both ends.

isotopic fractionation factor and melt properties. For example, the β values reveal no correlation with temperature. The discrepancy in the beta values seems likely be due to the difference in water content, suggesting that increasing water content facilitates the mobilization of ^{6}Li stronger than ^{7}Li, causing a greater effect on the isotopic ratio (Figure 24).

The boron isotope data from these experiments show a different scenario compared to lithium. No sinusoidal trend in the isotopic ratio was detected (Figure 19B). Instead, a slight decrease in the isotopic ratio is observed on the side with lower B content in three of the four runs (see isotopes profiles, Appendix A1). Possible effects related to irregularities in the starting glasses or in the sample analyses were excluded, as repeated measurements of the two reference materials were made after every five measurements of the samples (both SIMS and LA-ICP-MS). Furthermore, no matrix or drift effects of the measuring instruments were recognized, and it was verified that the two endmembers had a uniform isotopic ratio before the experiments. Lastly, this slight decrease in boron isotopic ratio was observed only for experiments in which diffusion had occurred. In zero-time experiments, the isotopic ratio remains constant throughout the entire profile.

We interpreted the cause of this difference to be a combined effect of diffusive isotope fractionation and equilibrium isotope fractionation between trigonal boron and tetrahedral boron, rather than a lack of diffusive fractionation. It is shown that the difference in diffusivity of trigonal and tetrahedral boron explains the concentration dependent diffusivity (Chakraborty et al.1993) and trigonal boron diffuses faster in the melt. Equilibrium isotope fractionation between trigonal and tetrahedral boron favours heavy boron (i.e., ^{11}B) which is associated with trigonal coordination. Putting all this together, in the B diffusion experiments, the side of low B concentration receives a flux of B. The faster moving trigonally coordinated B has heavier isotopic composition. Yet, due to diffusive fractionation, the lighter trigonal species potentially move faster than the heavier one. Considering that tetrahedral B for albite melts has been estimated around 6% in hydrous conditions (Schmidt et al., 2004), the isotope profiles might result from the cancellation of the isotopic signature across the diffusive interface, combining the faster moving trigonal B (mostly ^{11}B) with normal diffusive fractionation favouring the light isotope migration. Thus, the data from this study do not show a distinct isotope fractionation. Quantitative modelling of such a complex scenario is not presented here as there are too many unconstrained parameters, but this clearly warrants future attention.

Lack of boron isotopes fractionation was previously discussed by Chakraborty et al (1993). Alternatively, one can simply consider that the isotopic fractionation might have a different time window compared to the diffusion rates of boron. The experiments performed during this study may have been too short or too long if the isotopic fractionation takes place at different rates than the elemental diffusion. In this case, the isotopic fractionation is hardly visible because the system is either almost completely homogenised or fractionation did not occur yet. Considering boron slow diffusivity, the most likely conclusion is that isotopic fractionation has not occurred yet. Alternatively, it has occurred in the closest area to the interface, and SIMS measurements were too distant to detect its effects. However, the final equilibrated state of this experiment is the complete isotopic homogenization for a uniform concentration, and the isotopic homogenization of the starting diffusion couple was verified. Because the transient states that were monitored by this study do not show significant isotopic fractionation, the effect of the isotopic fractionation during B diffusion can be considered as small and undetectable.

4.5. Summary and application to degassing systems

Lithium and boron are fluid-mobile components in magmas stored at depth, and they passively participate in the dynamics of bubble nucleation and growth, which may trigger and define the volcanic eruption style. In this study, diffusion-couple experiments were performed to better constrain self-diffusion of lithium and boron in hydrous silicate melts. From the evaluation of the results, lithium and boron diffusivity were confirmed to be significantly influenced by the concentration of water in the system.

Lithium diffusion is extremely fast starting at temperatures below 700 °C. Its diffusivity is negatively correlated to the concentration of H_2O in the silicate melt, (Figure 22B) while lithium isotopic fractionation seems to be affected additionally by the diffusion of the major elements in the silicate melt. The coefficient β calculated by the model fitting is slightly lower than what has been previously

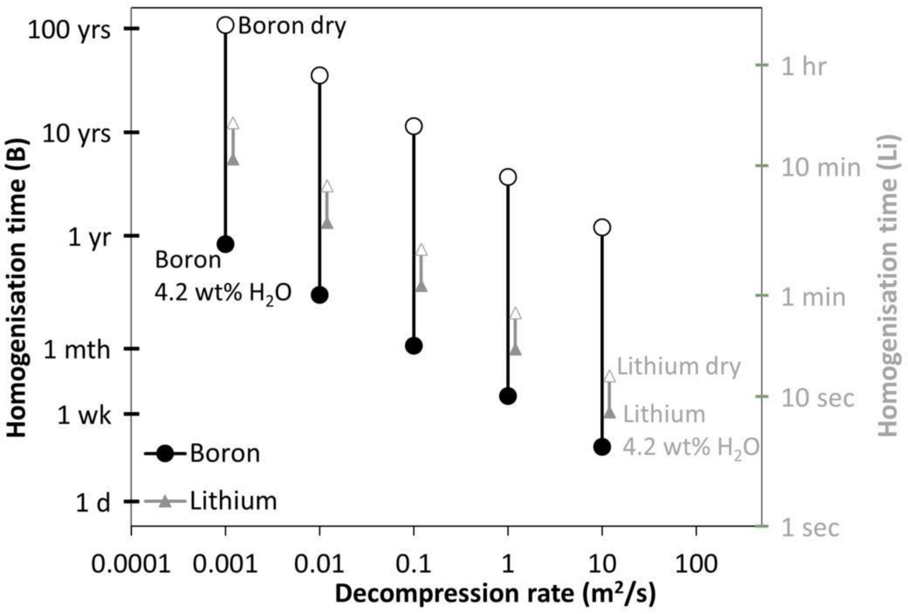

Figure 25 Homogenisation times of lithium (grey triangles) and boron (black dots) for different decompression rates of a magma at 1000 °C and with a water concentration of 4.2 wt% (full symbols) or in dry conditions (open symbols). These points represent an approximate time that the system needs in order for the diffusion of lithium and boron to lead to complete homogenization during magmatic degassing.

published; the observed differences are presumably due to very different experimental setup (Richter et al., 2003) or the different water content (Holycross et al., 2018).

Boron diffusion occurs at slower rates, compared to lithium. When it is a major constituent of the glass composition, boron is strongly influenced by silicon interdiffusion, as the mass flux of the diffusion reaction needs to be maintained in both directions (Chakraborty et al., 1993). When boron is present as a trace element the diffusion of silicon in the opposite direction can be neglected. Boron diffusion is mainly controlled by the structural position of boron in the silicate network, namely whether it is in tetrahedral or trigonal coordination with oxygen. Even though the presence of water enhances the amount of tetrahedrally coordinated boron species, the effect on the structural position of boron is negligible compared to the impact of the decrease in viscosity by dissolved H_2O in the silicate melt, which facilitates diffusion as B mobility is controlled by viscous flow.

The very slight change in the isotopic ratio of boron isotopes seems to be related to the diffusion process, but the interpretation of these observed results is still unclear. Several scenarios have been proposed to explain the results shown in this study, but no modelling of the observed data has been done. Further investigations will be required to get a complete picture of the dynamics of this process. Based on the timescale of the diffusion process, boron isotopes could still be useful to record degassing phenomena and slow-moving fluid migration inside a magma chamber despite no clear isotopic signature was recognised in these data.

With the information of our diffusion study, it was possible to estimate timescales of lithium and boron diffusion in hydrous or dry rhyolitic melts. In Figure 25, the magma temperature was fixed at 1000 °C and approximate homogenisation times of Li and B were calculated due to diffusion in a decompressing magma. The homogenisation time can be considered as the maximum time where any diffusion effects may be retained and modelled. This time-window changes depending on the decompression rate applied to the system: as the decompression rate increases, the distance between nucleated gas-vesicles decreases and therefore the space available for diffusion is shorter. Having significantly different diffusion coefficients, lithium and boron were combined to observe a wider range of process timescales: from seconds to hours for lithium, and from hours to weeks or months for boron.

These timescales can be used as a starting point for further investigation, which will be the main focus of Chapter 5 of this dissertation. The behaviour of lithium and boron could be related to decompression-induced degassing and magmatic ascent, and they could be used to develop a speedometer for volcanic ascent rates. Watson (2017) started to examine this topic, performing a series of numerical simulations on the behaviour of several volatile species during bubble nucleation and growth. While boron was not considered in that study, Watson (2017) reported important work on lithium incorporation in bubbles during magma degassing. Based on the conclusions of this work, Watson's numerical simulation is accompanied with this experimental investigation, using lithium and boron as indicators of magma ascent rate and degassing.

Decompression experiments performed at different decompression rates will provide information about how lithium and boron behave during volatile exsolution and if any isotopic fractionation takes place during bubble nucleation and growth. The ability to associate the decompression rate (and indirectly the magma ascent rate) with the chemical distribution of these two elements in the melt between growing bubbles, would lead to the development of a precise speedometer applicable to erupted products of highly silicic volcanoes, so that lithium and boron will serve as an additional tool for tracing magmatic ascent and degassing rates prior to volcanic eruptions.

5. Li and B fractionation during decompression-driven degassing

In this section the potential use of lithium and boron as geochemical tracers of volatile component fractionation during magmatic ascent in volcanic systems is presented. Using the starting synthetic glasses of the two series LPR50 and LPR200, a series of isothermal decompression experiments at different decompression rates was performed at 900 °C and 1000 °C. Decompression was performed with a duration of 30 minutes, two, five and ten hours, starting from an initial pressure of 300 MPa terminating at final pressures of 70-77 MPa. The results of lithium and boron concentration and isotope variations were related to the decompression rates of the experiments, showing a relation between trace element exsolution and the nucleation and growth of bubbles.

5.1. Bubble Number Density (BND) calculation and experimental decompression rates

The Bubble Number Density (BND) is a numerical definition of the bubble number and distribution in the sample. It defines the number of bubbles per unit volume. Instead of measuring each bubble separately, the BND can be calculated following Gardner et al. (1999), via the evaluation of the size and quantity of all bubbles together.

$$\mathrm{BND} = \frac{\mathrm{N_T}}{\mathrm{V_T}} = \frac{\Phi_\mathrm{M}}{\sum\left(\frac{\mathrm{n_i}}{\mathrm{N_T}}\mathrm{V_i}\right)} \tag{13}$$

In equation 13 n_i is the number and V_i is the volume of the bubbles of a specific diameter i; N_T is the total number of bubbles, a function of the bubbles volume fraction Φ_M. Finally, V_T is the sum of V_B and V_M: the volume of the bubbles and the melt, respectively. Subsequently, the obtained values were normalized to the volume of the liquid phase, as it is assumed that it remains constant despite the gas expansion within the silicate melt.

We calculated this value on a series of 18 BSE images taken on each sample and at different magnifications: nine photos were taken on a horizontal section of the capsule, while the other nine were taken by cutting the sample lengthwise (vertical cut), so as to have an overall view of the appearance of the sample in the three dimensions. Each set of nine figures was composed of one picture at magnification ×45, three pictures at ×80 and five pictures at ×150, in order to be able to evaluate the same sample, both as a whole and in detail with increasing magnification. This method was applied to avoid truncation effects, given by the fact that the use of two-dimensional photos certainly involves an approximation of the real number and size of bubbles (Armienti, 2008).

Following the method of Noguchi et al. (2008), the program imageJ[3] was used to select the area and enhance the greyscale of the picture to emphasize the bubbles with respect to the sample glass. After having scaled the image in µm, the bubbles surface was selected and the particles were analysed obtaining a list of highlighted bubble areas, as well as the total count of the selected particles in the analysed surface. Afterwards, program CSD corrections[4] was used to convert the obtained surface values into volume entities. This program allows to enter the circularity of the inserted particles (values between 0 and 1, for angular and spherical particles, respectively), as well as the total area of the image and the list of the single particles obtained by the imageJ evaluation. It has originally been created for the determination of the crystal size distribution in natural samples, but the same procedure can be applied to bubbles in a glass sample (Higgins, 2000).

Using this method, the final result is the volume occupied by bubbles in the selected area, grouped by similar size of the particles. The bubble number density is then calculated by the sum of the aforementioned values, scaled in m^3. This procedure has been repeated for each image at every magnification, and the obtained values have been confronted to each other, to the picture series of the other cut direction of the same sample, and finally to the other samples as well. With this method, a general evaluation can be done on what is the most common bubble size in the sample, and how this is distributed in the analysed image.

---

[3] https://imagej.nih.gov/ij/

[4] http://www.uqac.ca/mhiggins/csdcorrections.html

5.2. Results and discussion

5.2.1. BND, water loss and equilibrium/disequilibrium degassing

An overview of the decompression path of each experiment is shown in Figure 26, where the global decompression rate and duration of each experiment are reported. The dataset contains a total of 7 decompression experiments: three with duration of 30 minutes (two at 900 °C and one at 1000 °C), two with a two-hours decompression (900 °C and 1000 °C), and the two longer experiments of five and ten hours were performed at 1000°C only. After 48 hours of annealing, the decompression was initiated until reaching 70-75 MPa, and interrupted by an isobaric rapid quench, with cooling rates around 150 °C/s (see Chapter 3.2 for details).

The decompression rates shown in Figure 26 report values corresponding to the full duration of the decompression, between 300 MPa and the quench pressure. It has been discovered that decompressing magmas tend to have a precise nucleation pressure, as a function of the melt temperature (Mourtada-Bonnefoi and Laporte 2004; Hamada et al.2010). This occurs because bubble nucleation is triggered only when the supersaturation pressure is sufficiently large, between the total pressure and the water saturation pressure, which is a function

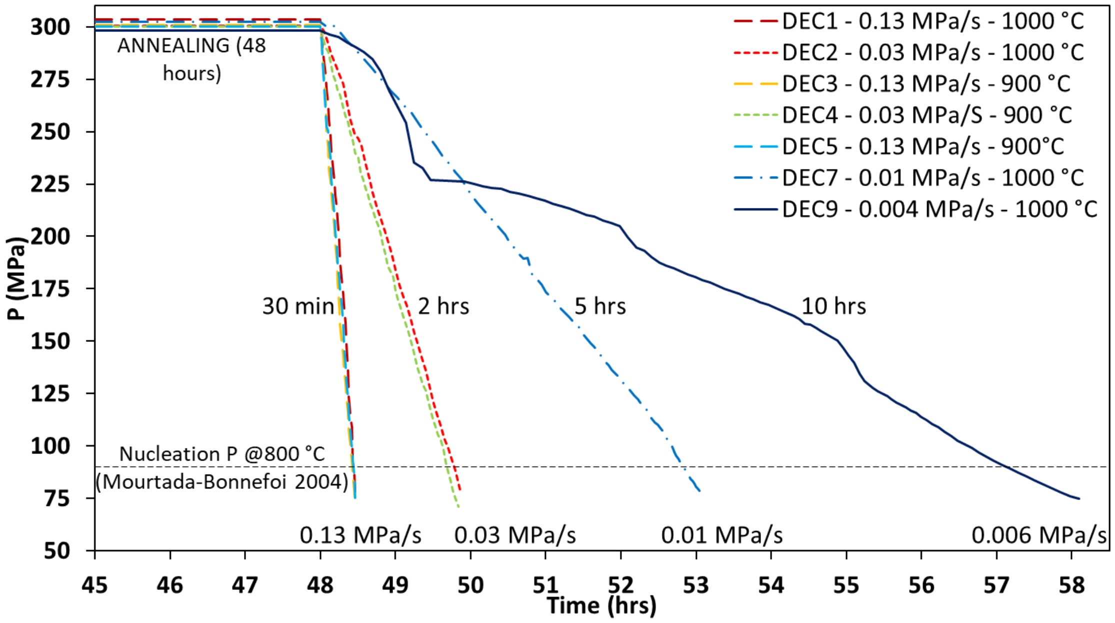

Figure 26: decompression path of the executed experiments during this study. During experiment DEC9 (10 hours), a pressure drop occurred in the initial stage of the decompression, which was overall not effective on the sample result.

of the melt temperature. Longer decompression rates create a lower supersaturation pressure of the gas in the melt, facilitating bubble growth. On the contrary, a faster decompression generates a higher supersaturation pressure of the gas phase in the melt, creating more bubble nucleation sites (Nowak *et al.*, 2011).

Table 3: BND of each sample (horizontal and vertical cut of the capsule) with the experimental conditions of each run. P_i - P_f and H_2O_i H_2O_f are the initial and final experimental pressure and water content, respectively. The experimental decompression time is given by t expressed in minutes, at temperature T. $Log_{10}BND$ are the logarithm of the average BND values in m^3. Values in brackets are the standard deviation errors.

Sample	**P_i (MPa)**	**P_f (MPa)**	**t (min)**	**Dec rate (MPa/s)**	**T (°C)**	**Log_{10} BND (m^3)**	**H_2O_i (wt%)**	**H_2O_f (wt%)**
LPR200_DEC1_horizontal	303.6	77.9	29	0.118	1000	13.13(0.10)	4.67	3.0(0.3)
LPR200_DEC1_vertical						13.12(0.12)		
LPR50_DEC1	303.6	77.9	29	0.118	1000	Heterog	3.64	1.1(0.1)
LPR200_DEC2	300.4	77.3	111	0.038	1000	Heterog	4.37	1.9(0.2)
LPR50_DEC2_ horizontal	300.4	77.3	111	0.038	1000	12.43(0.18)	3.85	3.1(0.2)
LPR50_DEC2_vertical						12.51(0.18)		
LPR50_DEC3_ horizontal	300.9	70	28	0.114	900	13.45(0.09)	4.07	3.1(0.3)
LPR50_DEC3_vertical						13.38(0.12)		
LPR200_DEC4	300	71	110	0.035	900	Heterog	3.93	1.7(0.4)
LPR50_DEC4_ horizontal	300	71	110	0.035	900	12.86(0.05)	4.86	3.0(0.3)
LPR50_DEC4_vertical						12.89(0.06)		
LPR200_DEC5_ horizontal	300	75.2	28	0.151	900	13.61(0.14)	3.81	3.1(0.1)
LPR200_DEC5_vertical						13.60(0.06)		
LPR50_DEC5_horizontal	300	75.2	28	0.151	900	13.89(0.09)	4.19	3.1(0.1)
LPR50_DEC5_vertical						13.77(0.05)		
LPR50_DEC7_ horizontal	302.5	75.6	5 06' hrs	0.015	1000	11.47(0.34)	3.91	2.9(0.1)
LPR50_DEC7_vertical						11.51(0.19)		
LPR50_DEC9_ horizontal	298.4	74.8	10 06' hrs	0.0044	1000	11.26(0.04)	3.92	3.0(0.1)
LPR50_DEC9_vertical						11.04(0.23)		

Rhyolitic melts at 800 °C have a bubble nucleation pressure around 90 MPa, while the same melt composition at 700 °C starts nucleating bubbles at around 55 MPa (Hamada *et al.*, 2010). No data are available for higher temperature systems; therefore, there is no precise determination of the nucleation pressure in the case of this experimental set (900 °C and 1000 °C). However, this does not generate major problems here, because of the choice to perform continuous decompression experiments. Assuming that the nucleation pressure will increase with increasing temperature, the decompression rates reported in this section were calculated in the pressure gap between 100 MPa and the quench pressure. These calculated decompression rates are reported in Table 3 and remain overall similar to the values of the entire decompression experiment but describe more precisely the bubble nucleation and growth phase during the experimental run.

The experiment DEC9 had a less constant decompression path than the other experiments (Figure 26). An IHPV malfunction lead to a pressure drop in the initial stage of the decompression, but through the solubility model of (Newman and Lowenstern, 2002), it was estimated that the water dissolved in the liquid phase

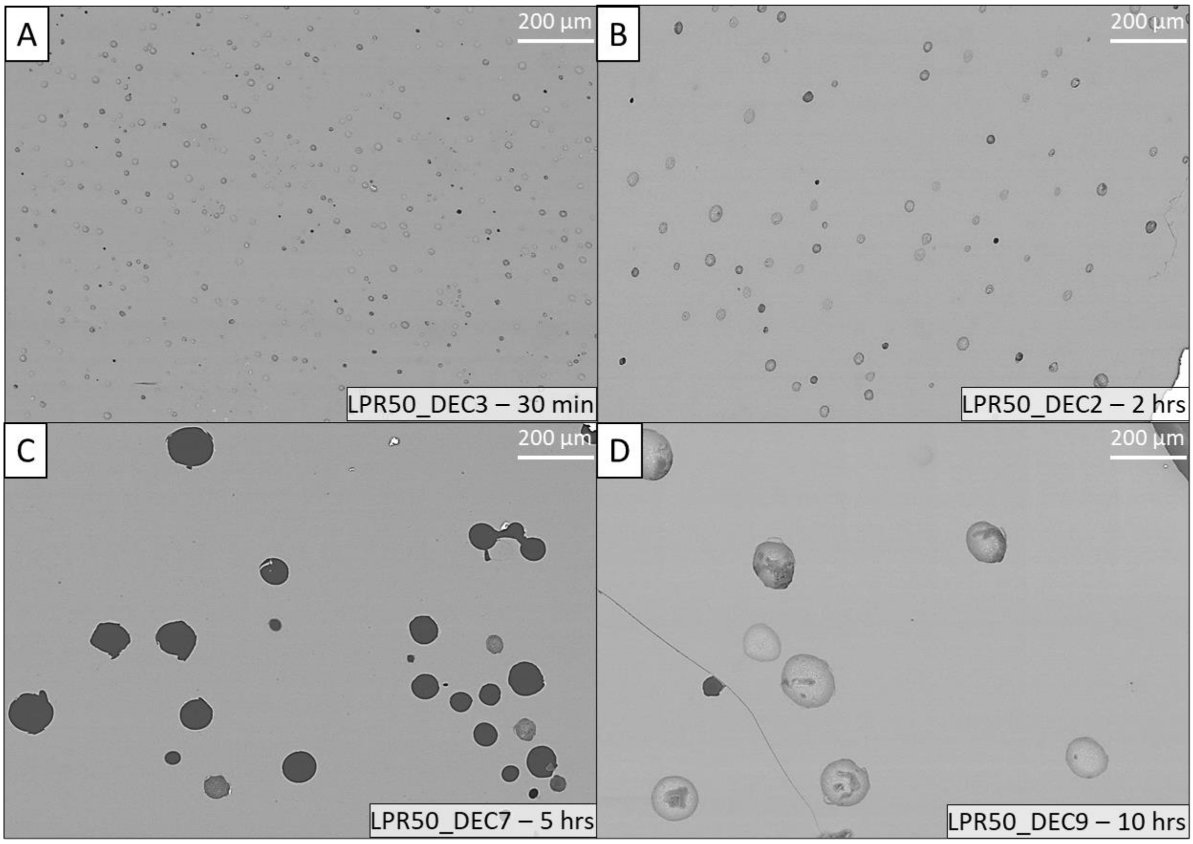

Figure 27: Example of four different samples with different decompression rates (specified in Table 3). The bubble size increase with decreasing decompression rate, while their number is higher for faster decompressions.

did not start to nucleate bubbles yet. Therefore, the pressure drop did not have an effect on water exsolution.

Table 3 reports the total pressure (initial and final values) and temperature parameters, along with the initial and final water contents and the BND results. The BND results reported in Table 3 are the logarithm value of each sample series average in m³ (single values are reported in Table A2.3 in Appendix A.2). A distinction has been made between front and side pictures, in order to compare the BND in the vertical (lengthwise) and horizontal (width) section and evaluate the three- dimensional distribution of the bubbles. The difference between the horizontal and vertical BNDs is generally very small, within the standard deviation error of the average values per each sample.

Along with the evaluation of the decompression paths and the BND of the experimental runs, many interesting observations could be done regarding the texture of the samples after the decompression experiments. High resolution backscatter electron images highlight that the bubble number and distribution vary as a function of the decompression rate used in the experimental runs, as shown in Figure 27. In this figure, the decompression time of the experiments progressively increased from picture A to D and shows an increase of the bubble size and a decrease of bubble number. In Figure 27C where a five-hour decompression is shown, it is noticeable that some bubbles appear to be coalescent. This was a polishing effect, where the glass between the bubbles broke. In this case, the bubbles have been counted separately during the BND calculation.

Samples with spherical bubbles, homogeneously distributed in the glass were interpreted as successful results of the performed experiment (Figure 27). In these

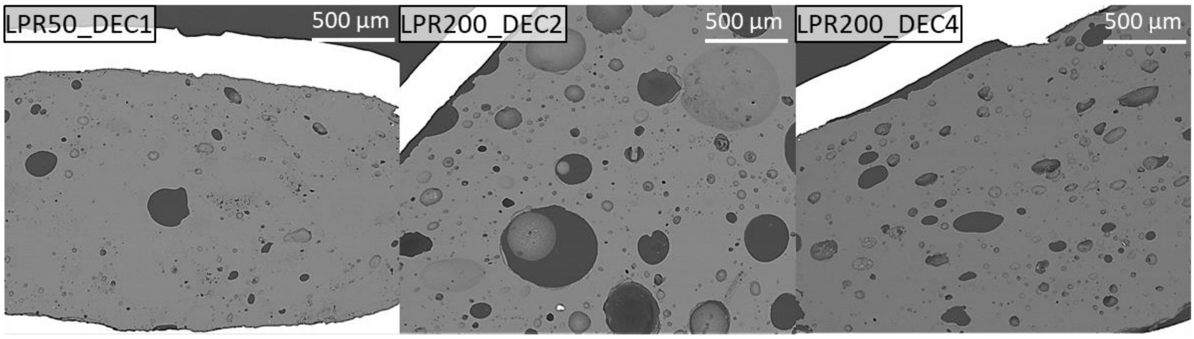

Figure 28: Backscattered electron images of the samples LPR50_DEC1, LPR200_DEC2 and LPR200_DEC4, where a probable contamination of acetone during the sample preparation phase caused the occurrence of heterogeneous bubble nucleation.

cases the bubble nucleation was caused solely by decompression-induced degassing, with no secondary bubble nucleation events or no pre-existing bubbles prior to the decompression (Mourtada-Bonnefoi and Laporte, 2002). A few samples encountered problems most likely during the sample preparation. For instance, a small amount of air may have been trapped in the capsule before it was sealed. Thus, the atmospheric N_2 trapped in the capsule at the initial stage of the experiments may have altered the bubble nucleation process (Gardner *et al.*, 1999; Mourtada-Bonnefoi and Laporte, 2002), causing the bubbles to be heterogeneously distributed and with different sizes. This is the case for samples LPR50_DEC1, LPR200_DEC2 and LPR200_DEC4 shown in Figure 28, where clearly the bubbles are heterogeneously distributed and caused by different nucleation events (Mollo *et al.*, 2017). Most likely, the pre-existing bubbles started to grow as soon as the decompression initiated and become significantly bigger than expected from homogeneous nucleation, while smaller bubbles nucleated during the decompression.

This study only focused on homogeneous bubble nucleation, as it is critical to be able to understand volcanic systems in simplified manner. Obviously, the BND calculation would have been significantly affected by the changes induced by the presence of an earlier population of bubbles before the decompression occurred, as well as the lithium and boron diffusion during their exsolution process. For this reason, these samples were not considered in the analysis of lithium and boron,

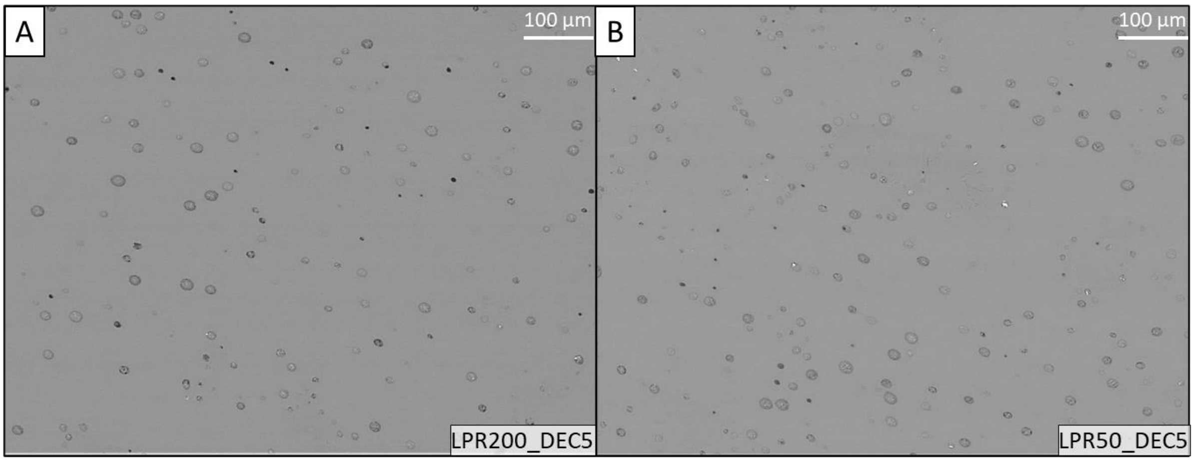

Figure 29: Comparison between enriched and depleted starting glass materials after the decompression at the same conditions of pressure and temperature. No differences have been noticed by the visual evaluation of the samples, and the BND results have the same order of magnitude and similar values.

but some evaluation was done on their water content after the decompression, which will be presented in the next paragraph.

Additionally, we compared the results of the decompression experiments on the two different sample series used for these experiments, which are shown in Figure 29. The aim was to verify if the different concentration of Li and B in the starting glasses causes any variation in the bubble nucleation and growth process during decompression. The sample series LPR50 and LPR200 respectively indicate the depleted (LPR50: Li and B contents 60 µg/g and 180 µg/g) and the enriched starting glasses (LPR200: 200 µg/g Li and 600 µg/g B). The two different concentrations of Li and B did not seem to generate any effect on water exsolution, as the bubble number and distribution looks identical from the observation of the texture of the samples in Figure 29. This was further confirmed by the comparison of the BND of the two samples, reported in Table 3. The average $\log_{10}$BND values for the two samples of the experiment DEC5 are 13.61 ± 0.14 (LPR200) and 13.60 ± 0.06 (LPR50). The difference between the average values of the two datasets remains within the standard deviation errors, suggesting that the concentration of Li and B do not affect the dynamics of bubble nucleation and growth during the decompression, when present as trace elements.

Finally, a comparison has been made between the experiments performed at 900 °C and at 1000 °C, here presented in Figure 30. The samples shown in the figure both belong to the LPR50 series, with identical chemical composition (LPR50-DEC4 and LPR50_DEC2). The experiments that produced these results were performed with similar decompression rates of 0.038 MPa/s and 0.035 MPa/s

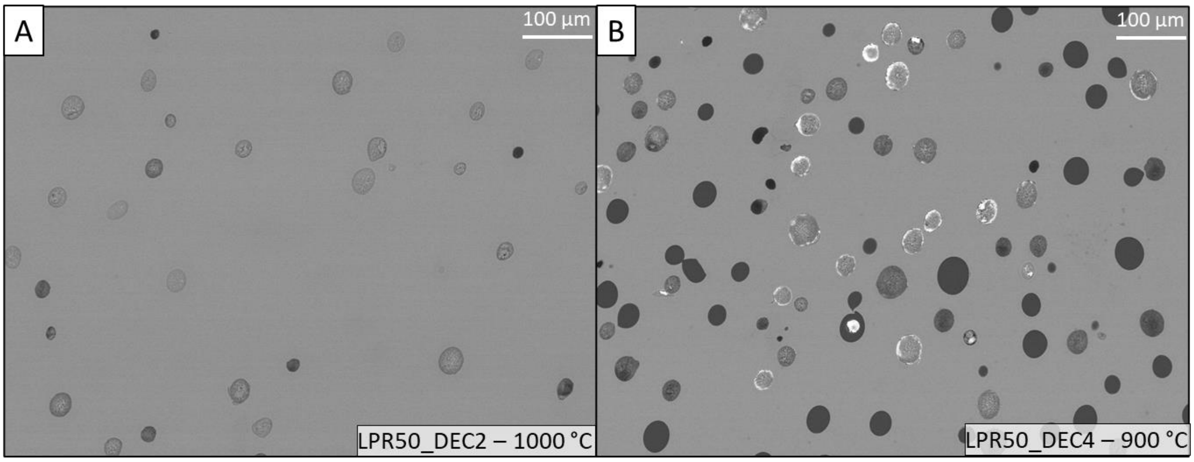

Figure 30: Comparison between two samples of the series LPR50 at the same magnification after experiments performed at the same decompression rate but 1000°C (A) and 900°C (B). The size of the bubbles is overall similar, but their number is significantly higher for the low-temperature experiment.

and a quench pressure of 77.3 and 71 MPa, for the DEC4 and the DEC2 experiments, respectively. The sole difference between the two runs was the experimental temperature: 900 °C (DEC4) and 1000°C (DEC2). From the observation of the two pictures in Figure 30A and Figure 30B, the two samples present an overall similar bubble size, but the bubble number and distribution is significantly higher for the experiment performed at 900 °C, shown in Figure 30B. Coherently with this observation, the $\log_{10}$BND calculated for the experiment performed at lower temperature presents values that are approximately 0.5 higher compared to the high-temperature experiment (Table 3). This confirms that the temperature has a key role in the dynamics of bubble nucleation and growth during decompression-driven degassing.

In order to better understand the dynamics of degassing occurred during decompression experiments, we assess the evolution of the water content dissolved in the samples, before and after the decompression experiments. The initial water content (H_2O_i) given in Table 3 has been calculated from the weight of the starting glass powder and the distilled water inserted in the capsule before the experiment, because it was impossible to properly measure the water content in the glass before the decompression. We estimated a general error of ± 0.2 wt%, given by the potential water or powder loss during the procedure of preparation of

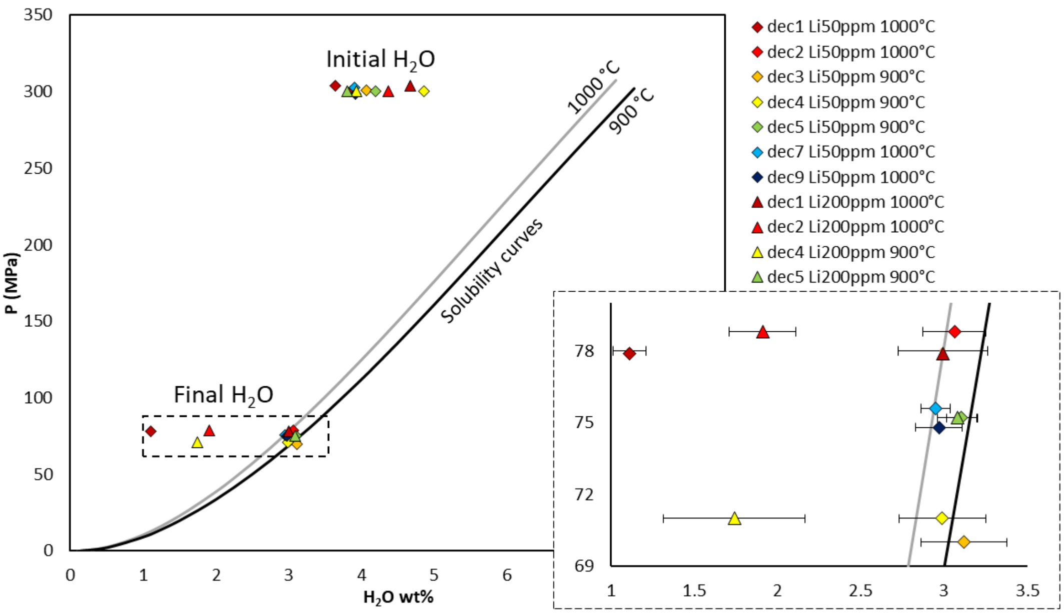

Figure 31: Water loss during the decompression experiments. All samples (except the three contaminated samples) contain a final water concentration which is consistent with the solubility curves at run temperature and indicates equilibrium degassing (solubility curves calculated using the model from Newman and Lowenstern, 2002).

the sample, before the capsule was welded and sealed. The water content after the decompression (H_2O_f) has been measured by repeated Raman analyses and the average values are reported in Table 3. These water contents are overall consistent with those determined by the method by difference of the sum of the major elements from 100%. These electron microprobe analyses confirmed the overall constant chemical composition of the glasses after decompression experiments and are reported in Table A2.1 in Appendix A2. The difference between the two water content estimates remains within ±0.5 wt%, which is overall compatible with the standard deviation of the results by Raman technique.

Starting from an initial water content between 3.6 wt% and 4.4 wt%, the final water concentration of the different decompression samples is exceptionally consistent. Looking at the samples with homogeneous bubble distribution, the final H_2O contents ranges between 2.9 wt% and 3.1 wt%. On the contrary, samples with a heterogeneous number, size, and distribution of vesicles (Figure 28) have a final water concentration significantly lower, between 1 wt% and 2 wt%. Figure 31 shows the initial and final water content of each sample at the corresponding initial and final pressure, as well as the solubility curves for a rhyolitic melt at 900 °C and 1000°C (Newman and Lowenstern, 2002). The final water results of almost all samples are close to their solubility curves at the experimental temperatures, which demonstrate that their degassing occurred at equilibrium. The samples that showed evidence of pre-existing bubbles before the occurrence of the decompression (Figure 28), have a water content that deviates from the solubility curves, with a major loss of water (Figure 31). These samples could be the result of disequilibrium degassing, affected by the trapped air in the capsule (Figure 28). The pre-existing bubbles would start growing as soon as the decompression starts, with volatile exsolution in a phase of the decompression where no bubbles should normally be present, in homogeneous nucleation conditions.

5.2.1.1. Bubble number density as an indicator of decompression rates

Bubble number density values of this study are consistent with the existing literature on homogeneous bubble nucleation and water exsolution processes, that shows that the BND is a direct function of the decompression rate (Mourtada-Bonnefoi and Laporte, 2004; Hamada et al., 2010). This confirms that the BND can be a good indicator of the decompression rate of an ascending magma, if this undergoes a slow and consistent ascent along the volcanic conduit.

We considered previous studies on the experimental determination of the relation between BND and decompression rate (Mourtada-Bonnefoi and Laporte, 2004; Hamada et al., 2010), and the numerical simulation of the BND evolution with the decompression rate (Toramaru 2006). Figure 32 reports our results in relation to the experimental data of Mourtada-Bonnefoi and Laporte (2004) and Hamada et al. (2010), as well as the numerical model of Toramaru (2006).

The experimental studies focused on homogeneous bubble formation in a rhyolitic melt during decompression runs at different rates, at the temperatures of 700 °C and 800 °C. The study of Hamada et al (2010) represents a continuation of the research conducted by Mourtada-Bonnefoi and Laporte (2004), therefore they applied a very similar experimental setup. They used a rhyolitic composition similar to the one employed here, and doped their starting glass with an initial H_2O content of 6.6 wt% (Hamada et al., 2010) and 7 wt% (Mourtada-Bonnefoi and Laporte, 2004), having initially supersaturated conditions. They used a pressure

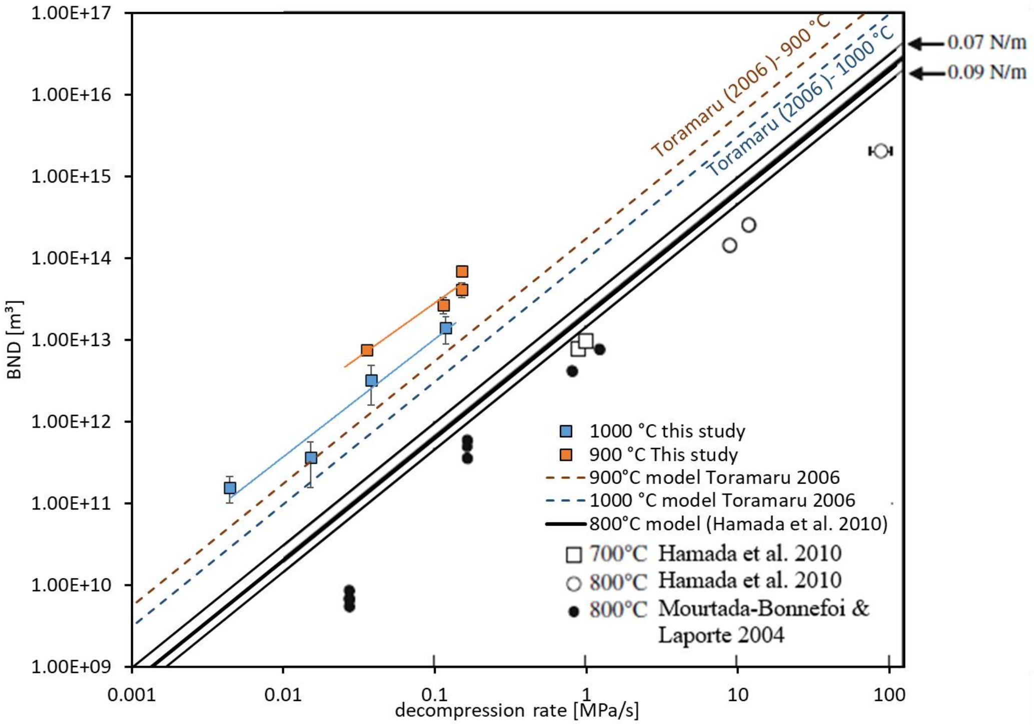

Figure 32: Experimental datasets of BND values as a function of the decompression rate (coloured squares, this study) in comparison with the numerical simulation of Toramaru (2006) and the experimental data from Hamada et al (2010) and Mourtada-Bonnefoi and Laporte (2004). Plot re-designed from Hamada et al (2010).

range between 280 and 30-75 MPa, with decompression rates ranging from 10 to 90 MPa/s (Hamada et al., 2010) and 0.2 to 1 MPa/s (Mourtada-Bonnefoi and Laporte, 2004).

The temperature has a strong effect in decompression experiments because its variation changes the water saturation pressure and consequently, the dynamics of bubble nucleation and growth. Higher temperatures lead to higher water saturation pressures, and the bubble nucleation process occurs later during the decompression, with a drop in the BND values. In fact, our data plotted in orange and blue in Figure 32 for the 900°C and 1000 °C experiments, respectively, show higher BND values for lower temperatures. However, our dataset has significantly higher values compared to the BND values reported by Mourtada-Bonnefoi and Laporte (2004) and Hamada et al. (2010), although their experiments were performed at 700°C and 800°C.

This can be explained because experimental temperature is not the only difference between this study and the compared literature. Initial water content plays a major role in the bubble nucleation process, because water diffusion through the melt is the main controlling parameter for bubble nucleation and growth (Toramaru, 1995). The major concentration difference between the 4.2 wt% initial water content of our study and the 6.6-7 wt% water content used by Mourtada-Bonnefoi and Laporte (2004) and Hamada et al. (2010) is the main cause of the offset between our experimental data and their results. The initially water-saturated conditions of the literature experiments affect the supersaturation pressure evolution during decompression. Furthermore, the higher water content causes an increase in the saturation pressure as well as water diffusivity. The combination of these effects significantly changes the dynamics of bubble formation, and the final BND values reflects these differences between this study and the compared literature.

In order to better compare our results with Hamada et al. (2010), the model of Toramaru, (2006) was applied to the experimental pressure and temperature conditions of this study. This model aims to numerically simulate the BND variation with respect to the decompression rates. Following Toramaru (2006), the BND values were calculated with equation 14, for a range of possible decompression rates dP/dt.

$$\mathrm{BND} = 34 * \mathrm{C_{sat}} * \left(\frac{16\pi\sigma_{LB}^3}{3\ \mathrm{kTP_{sat}^2}}\right)^{-2} * \left(\frac{\Omega_L \mathrm{P_{sat}}}{\mathrm{kT}}\right)^{-1/4} * \left(\frac{\mathrm{P_{sat}^2 kT\ C_{sat} D_{H_2O}}}{4\ \sigma_{LB}^2 |\mathrm{dP/dt}|}\right)^{-3/2} \tag{14}$$

In this equation, C_{sat} is the water content (defined as the number of molecules per unit volume) at saturation pressure P_{sat} (calculated with the model Volatilecalc, (Newman and Lowenstern, 2002) and temperature T in Kelvin. The equation also includes the Boltzmann constant k, the diffusion coefficient of water D_{H2O}, the volume of water in the melt Ω_L (fixed at 3×10^{-29}) and the surface tension σ_{LB}, which is a parameter extremely complicated to be experimentally determined (Bagdassarov et al., 2000). In Figure 32, Hamada et al. (2010) varied this value between 0.07 and 0.09 N/m, while Toramaru (2006) used a fix value at 0.08 N/m in the numerical simulation (thin lines and thick black line in Figure 32, respectively).

The two-coloured dashed lines in Figure 32 represent the application of the model with the chosen parameters of temperature, pressure, and water content of this study case. We chose a σ_{LB} value of 0.07 N/m, following Bagdassarov et al. (2000) and Mourtada-Bonnefoi and Laporte (2002). Compared to Hamada et al. (2010) and Toramaru (2006), only the parameters of temperature, D_{H2O} and C_{sat} were modified in our calculation, adapting these values to the experimental conditions of our study. The value of D_{H2O} for a water content of 4.2 wt% (average value of the initial water concentration in our experiments) was calculated following Zhang and Behrens (2000), and it was determined to be 3.48×10^{-11} m^2/s at 900 °C, and 5.88×10^{-11} m^2/s at 1000 °C.

Despite the slope of the model from Toramaru (2006) being in good agreement with our experimentally determined BND values, a significant underestimation of the modelled BND is observed by about one order of magnitude. In the numerical simulation, there is no certainty on the absolute value of some parameters, due to the difficulty of having direct measurements (for example the surface tension). Furthermore, some parameters were calculated using additional numerical models, leading to a general approximation of the involved parameters. Consequently, the displacement of the two models at 900 °C and 1000 °C with respect to the experimental results of this study may be caused by an artifact of the numerical model.

The direct relation between the BND and the decompression rates (hence the ascent rate of a degassing magma) allows to relate the behaviour of Li and B with the BND, creating a meeting point between the dynamics of bubble formation and the diffusion of lithium and boron around them.

5.2.2. Behaviour of Li and B in decompression samples

5.2.2.1. Detection of Li and B in the gas phase

Bubble nucleation and growth is mostly controlled by water exsolution and diffusion, while lithium and boron are to be considered as incorporated into the bubble during the degassing process by chemical partitioning. Currently no methods are known to exactly quantify Li and B contents in gas bubbles of volcanic products, hence a verification was necessary in order to demonstrate that the two elements are exsolved into the volatile phase during decompression. For this reason, a depth profile analysis was attempted, in order to reach and open a sealed bubble that was close to the surface of the sample. LA-ICP-MS analyses were attempted on different bubbles, and Figure 33 shows an example of the result. Here the lithium and boron raw signal of the ICP-MS analysis is plotted against the time of data acquisition. Between 50 and 140 seconds, the signal of the sample glass is visible, losing some intensity as the laser was going in depth into the glass.

Around 100 seconds, a clear and strong spike in the signal of lithium and boron is noticeable. This spike corresponds to the moment when the laser reached and opened the gas bubble. It is unclear whether this spike is related to Li and B trapped into the bubble in gas form, or whether it is a deposit of Li and B on the walls of the bubble, but it is certainly related to Li and B exsolution process during the bubble nucleation and growth phase. This spike is not quantifiable, as the raw signal of both elements goes back to the glass signal almost immediately (ca. 5 seconds). This may be due to the quick release from the bubble, when in gas or liquid form, or to the very small thickness of a potentially precipitated Li and B layer on the bubble walls.

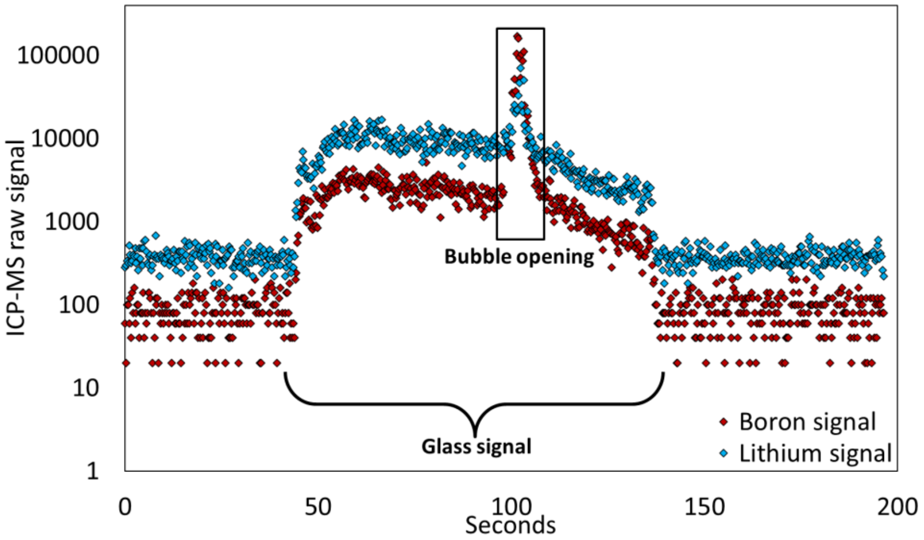

Figure 33: Raw signal of lithium and boron at the LA-ICP-MS, as a function of the time of data acquisition. The plot confirms that the two elements enter the bubbles during magmatic degassing, which is primarily controlled by water.

This procedure was only possible for the longer decompression runs, as the size of the bubbles allows an easy recognition of the vesicles close to the surface, and because the short runs present very small bubbles, with an average diameter of 15-20 µm, that would be too small compared to the ICP-MS laser size. Figure 33 confirms that lithium and boron do not change the dynamics of bubble formation but are partitioned into the bubbles during decompression. This will then be visible in the glass around the bubbles, which will be affected by the diffusion of volatiles into the bubbles during their growth.

5.2.2.2. Lithium and boron as a function of the decompression rate

Lithium and boron measurements (Figure 34) have been conducted on the LPR50 sample series, having the most complete set of samples and decompression rates, in contrast to the LPR200 series.

Profile measurements have been attempted, going from the bubble meniscus to an ideally homogeneous glass portion, possibly as far as possible from other bubbles in order to avoid interferences with neighbouring bubbles. Two different bubbles per sample have been measured, in the attempt of estimating the reproducibility of results, and lithium and boron concentrations have been plotted together in Figure 34. In this case, the locus in the diffusion profiles, or distance from the bubble meniscus are not considered, but all data were clustered together, in order to make general observations of our results with respect to decompression time of each experiment.

Generally, Figure 34A shows a positive correlation between the concentration range of the elements, with on the decompression time of the experiment for both Li and B datasets. The fastest decompression run presents the highest concentration range for both elements, with a decrease of the range as the experimental decompression time increased. The isotopic ratios are reported in Figure 34B, and similarly to the isotopic results reported for the diffusion study (Chapter 4), they are presented as δ values normalized to the starting glass values used as reference for SIMS measurements. Both elements have therefore an initial value of 0, while positive δ values indicate a higher relative concentration of the heavy isotope, while negative values refer to a generally lighter isotopic signature.

Figure 34B shows that the different samples are characterized by a wider range of values, with less clear trends compared to the concentration results. The 30-minutes decompression has globally depleted values of δ^{7}Li and δ^{11}B with ranges -8 to +4 and -8 to 0, respectively. Samples from the two- and five-hour decompression runs have similar isotopic results, with generally higher δ^{7}Li and δ^{11}B values compared to the 30-minutes experiment. The δ^{7}Li values are in the range -1 to +4 (two-hour run) and -1 to +9 (five-hour run) and δ^{11}B values vary between -4 and +4 for both experiments.

The ten-hour decompression run shows the heavier isotopic signature for boron, with a δ^{11}B ranging between -3 and +6, but the lithium isotopic signature shows a tendency to converge to the values of the reference material, with δ^{7}Li values between -2 and +7. In general, the two datasets are characterized by a clear decrease in the isotopic ratio for the fastest decompression, with a progressive increase in the isotopic ratio, as the decompression rate of the experiment decreases.

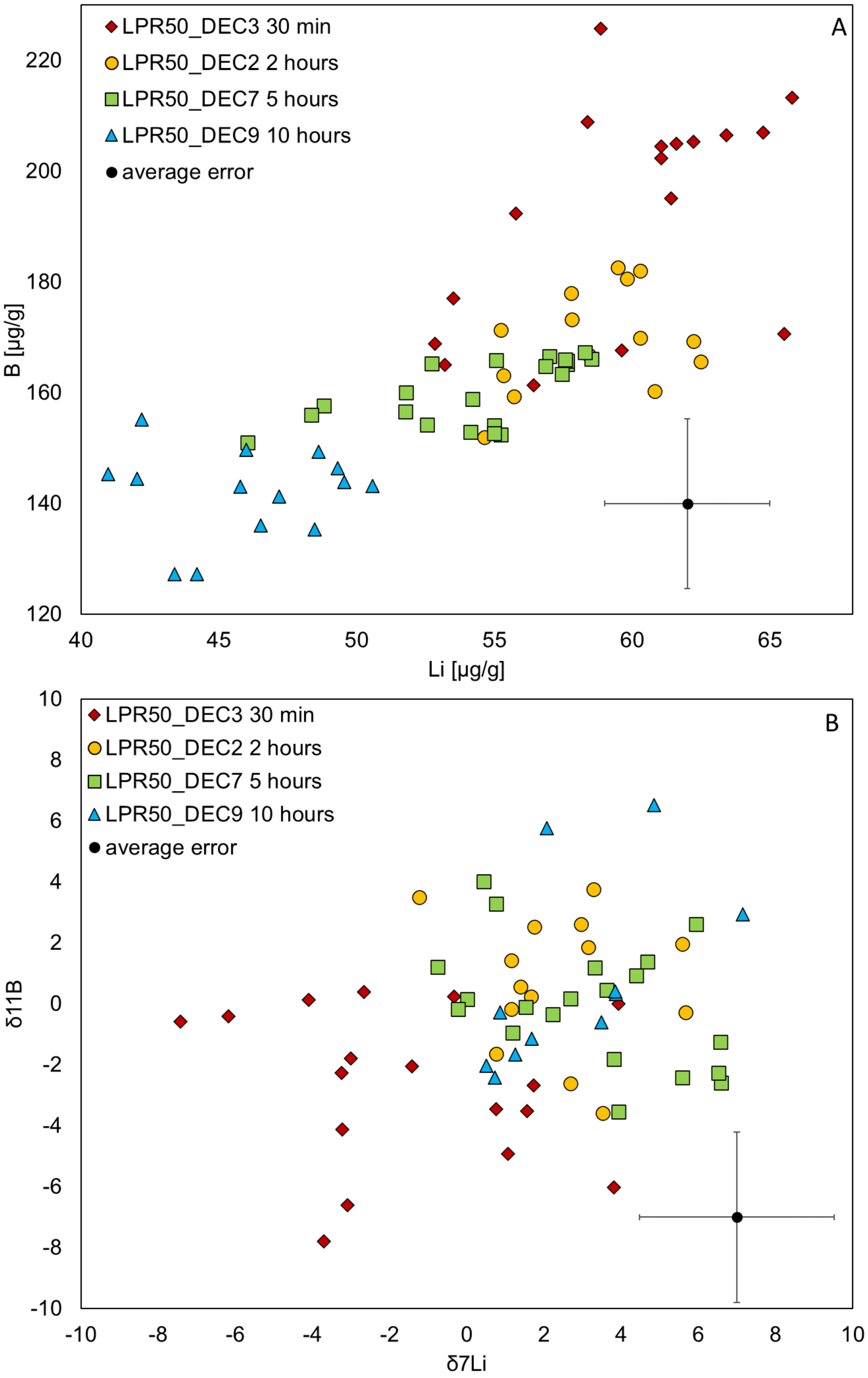

Figure 34: Concentration (A) and Isotope (B) data measured by SIMS of Lithium vs. Boron, reported as a function of the different decompression times. The black circle represents the average value of analytical error for Li and B contents as well as their δ values.

In order to better interpret these results, we plotted in Figure 35 the concentration and isotopic ratios of Li and B of the different experiments with respect to the BND experimentally determined in the previous section (Chapter 5.2.1. Table 3), in order to make a direct comparison between the Li and B concentration and isotopic range and the BND determined for each decompression experiment.

Figure 35A reports the relative elemental concentration variations normalized to the value of the starting Li and B concentration before the experiment. The two concentration datasets report a similar trend of Li and B behaviour, undergoing a progressive depletion with decreasing BND values. As the BND is directly dependent on the decompression rate in our experimental runs (Figure 32), this observed behaviour of lithium and boron is consistent with the dynamics of volatiles exsolution. During the decompression-driven degassing, as the melt continuously loses volatile components which partition into the gas phase, the samples with extended time for bubble growth show stronger sign of diffusive transport for Li and B to exsolve into the gas bubbles during their growth.

The tendency for Li and B to decrease the overall concentration in the residual melt with decreasing BND seems to be stronger for boron than for lithium. The slower diffusivity of boron in silicate melts, compared to lithium, causes a stronger effect on the overall concentration of the samples as indicated by a steeper slope in Figure 37A. Considering that the final water content of the glasses after decompression has a very narrow range between 2.9 wt% and 3.1 wt% (Table 3), the variability of the lithium and boron concentrations is not likely to be related to a major difference in the final water content. This implies that this progressive decrease of B and Li concentration with decreasing decompression rates is mainly caused by bubble growth, melt-fluid partitioning at the melt-bubble interface and diffusive transport of the two elements towards the bubble.

Figure 35B shows the general trend of the δ^{7}Li and δ^{11}B in the different samples, as a function of the experimentally determined BND values. In general, a tendency of the isotopic signature to become heavier with increasing decompression time is observed. Thus, longer decompression experiments (thus lower BND) have increasing isotopic ratios. This suggests that as the gas bubbles grows, the two light isotopes ^{6}Li and ^{11}B are preferentially fractionating into the gas phase.

The values of δ^{7}Li shown in Figure 35B progressively increase from the 30 minutes to the two hours decompression runs, but they remain overall constant from the two-hour to the ten-hour decompression experiments. This may be caused by an initial stage of homogenisation of the lithium isotopic ratio in the samples, or by the interaction of the Li fractionation process occurring

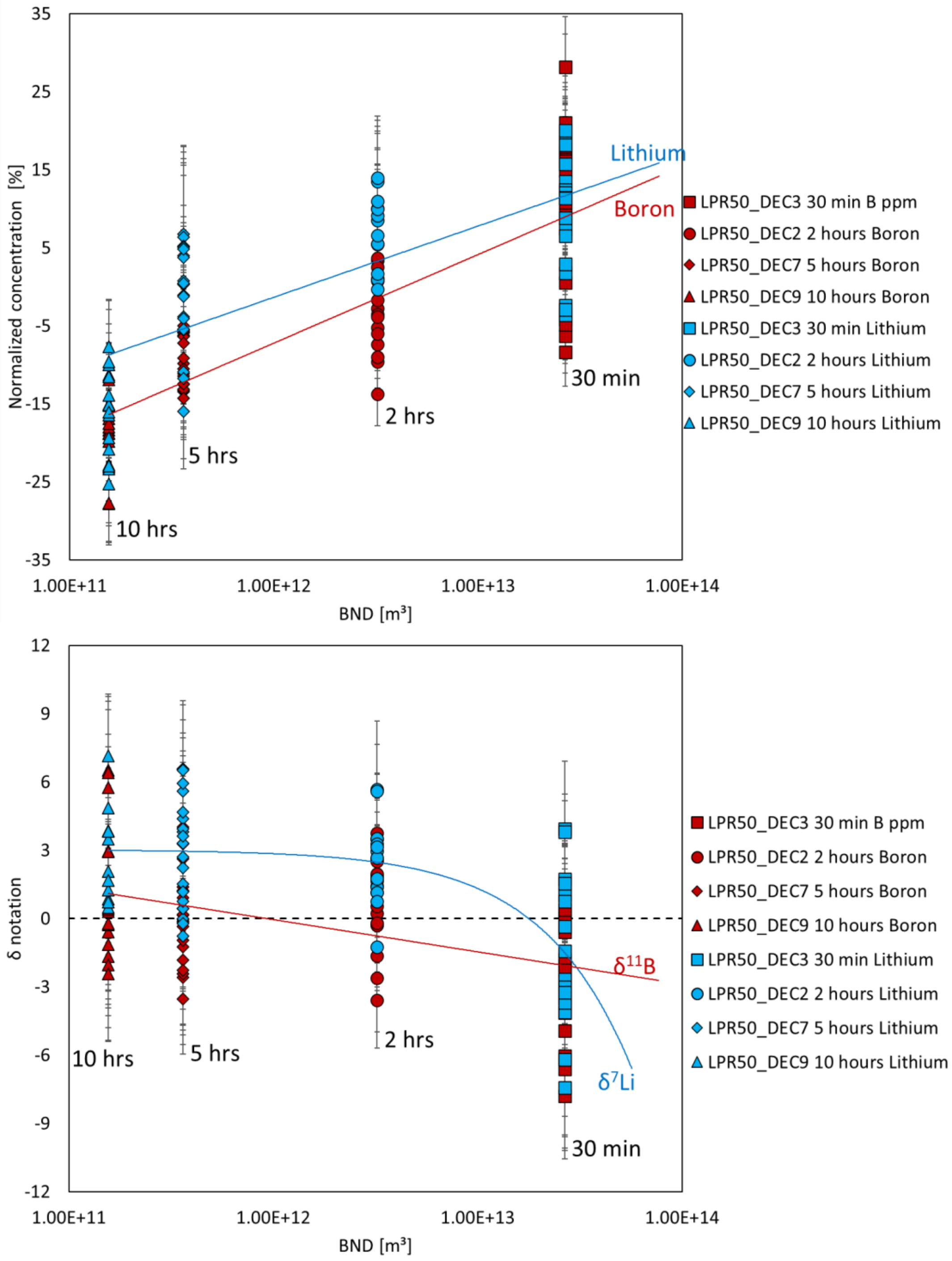

Figure 35: elemental concentration normalized to the average value of the starting material (top) and isotopic ratios (bottom) in form of relative δ notation of lithium and boron on the decompression BND.

simultaneously between several growing neighbouring bubbles. With longer decompression times, the δ^7Li values should progressively go back to the starting material initial value (in this study always 0 ± 1), as homogenisation is reached in the whole melt and the gas and melt phases are in equilibrium.

On the contrary to lithium, the δ^{11}B dataset shows a somehow more linear progressive increase of the average value with decreasing BND values. This is a further confirmation that boron isotopic fractionation occurs at slower rates compared to lithium. With smaller decompression rates and longer experimental times, Boron will likely follow the same trend as lithium, slowly reaching back the starting material initial isotopic ratio in longer times.

5.2.2.3. Elemental partitioning and isotopic fractionation during the bubble nucleation and growth process

Lithium and Boron measurements have been collected performing profile analyses of different bubbles per each decompression sample. The concentration and isotopic ratio profiles of the series LPR50 have been plotted together in Figure 36, in order to evaluate their behaviour as a function of the distance from the bubble meniscus.

The concentration profiles of Li and B are shown in Figure 36A and Figure 36B, respectively. It is immediately noticeable that one profile has a completely different trend from the others, and this corresponds to the fastest decompression experiment performed in this study (30 minutes). The profiles of the 30-minutes decompression show a clear increase in the concentration of Li and B in the melt close to the bubble meniscus. It is notable that the enrichment at the interface extends as a halo towards the surrounding melt (ca. 100 µm) and that it corresponds to 32% and 35% (Li and B, respectively) of the initial concentration of the two elements prior to decompression. This similarity in the percentage of enrichment is an indication that this accumulation is most likely generated by the kinetics of the bubble nucleation phase, more than a diffusion process from the host unaltered melt.

Figure 36C and Figure 36D show the δ^7Li and δ^{11}B profiles corresponding to the concentration profiles of Figure 36A and Figure 36B. At the same time as the

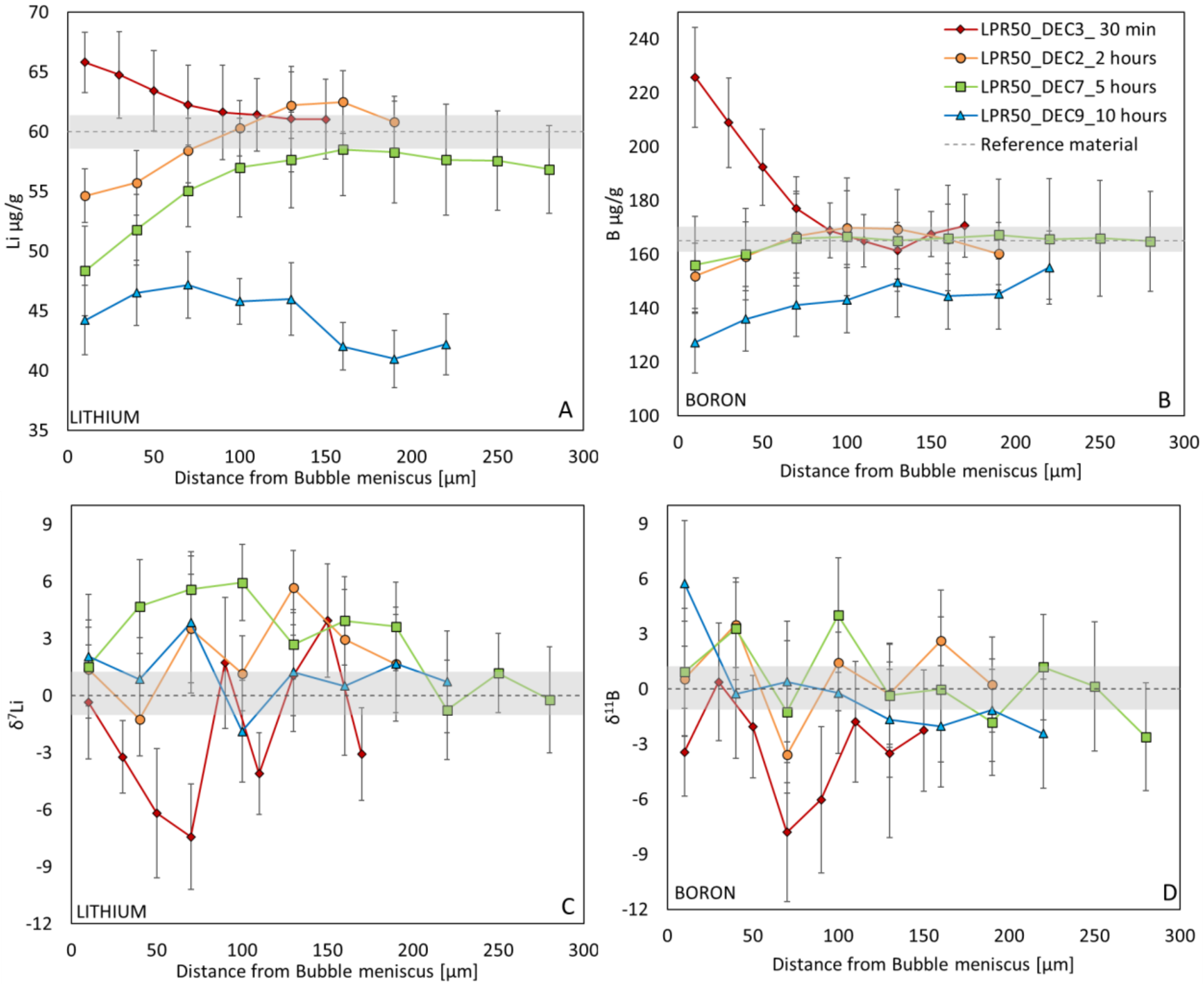

Figure 36: lithium and boron concentration profiles (A and B) and isotope ratio profiles (C and D) expressed in δ notation, in proximity of a bubble, whose meniscus is placed at distance 0 in the diagram. The four profiles show Li and B behaviour at each decompression performed in this study: 30 minutes (red), two hours (yellow), 5 hours (green) and 10 hours (blue).

concentration of Li and B increases, it is possible to observe a decrease in the isotopic ratio of both elements during the 30-minute decompression experiment.

For the decompression runs that lasted two, five and ten hours, (DEC2, DEC7 and DEC9, respectively) a decrease in Li and B concentrations is noticeable in the melt at the bubble-melt interface. This is visible especially for lithium in the profiles of the two- and five-hour experiments, where the direction of the diffusion profile is opposite than the 30-minute decompression run. Furthermore, the five-hour decompression run shows an overall depletion of the entire profile, given by a general depletion in Li in the whole melt during a longer phase of bubble growth. Simultaneously, an increase of the δ^7Li value is noticed in Figure 36C when the growth of the bubble becomes dominant, and the surrounding melt is characterized by lithium depletion (Figure 36C). The isotopic profiles of the experiments performed with a two- and five-hour decompression show an increase in the δ^{7}Li value which is moderate for the two-hours experiment, and more pronounced the five-hour decompression run, as the elemental diffusion of lithium progresses, and the concentration profile of lithium is progressively more depleted.

Boron concentration profiles shown in Figure 36B highlight a decrease in boron concentration going from the starting host melt to the bubble-melt interface, clearly imputable to a diffusion process of boron inside the bubbles. However, the two- and five- hour decompression experiments look very similar in the boron concentration profiles of Figure 36B. The extension of the diffusion profile is very small, and an overall depletion in the concentration is not present. Boron isotopic profiles of the two- and five-hour decompression runs reported in Figure 36D show an increase in the δ^{11}B values, compared to the 30-minute experiment. However, the values of the profiles are generally ranging around the value of the starting material (δ^{11}B = 0 ± 1). This is consistent with the concentration profiles in Figure 36B, where the effect of the diffusion process is significantly less evident both in terms of length of the diffusion profile and depletion of B at the bubble-melt interface, compared to the initial B content.

Ultimately, the ten-hour decompression run shows a non-monotonous profile for lithium, with a general depletion of its concentration (Figure36A). Analytical errors of the measurements are similar to the ones of the other concentration profiles; hence the overall depletion of the entire dataset must be related to the dynamics of growth of the bubbles, with slow decompression rates. The corresponding δ^{7}Li profile of the ten-hour decompression run shows a comparable isotopic signature with the starting material average (Figure 36C).

The boron concentration profile of the ten-hour run shows a similar overall depletion as lithium, but the profile shows a monotonically decreasing trend, from the unaltered host melt to the bubble-melt interface. The profile of δ^{11}B for the ten-hour experiment shows an evident increase in its value for the point of measurement closest to the bubble meniscus. The increase of δ^{11}B has very short extension in the length of the profile, which is probably caused by the slower diffusivity of boron. Measurements with a smaller distance between the data points

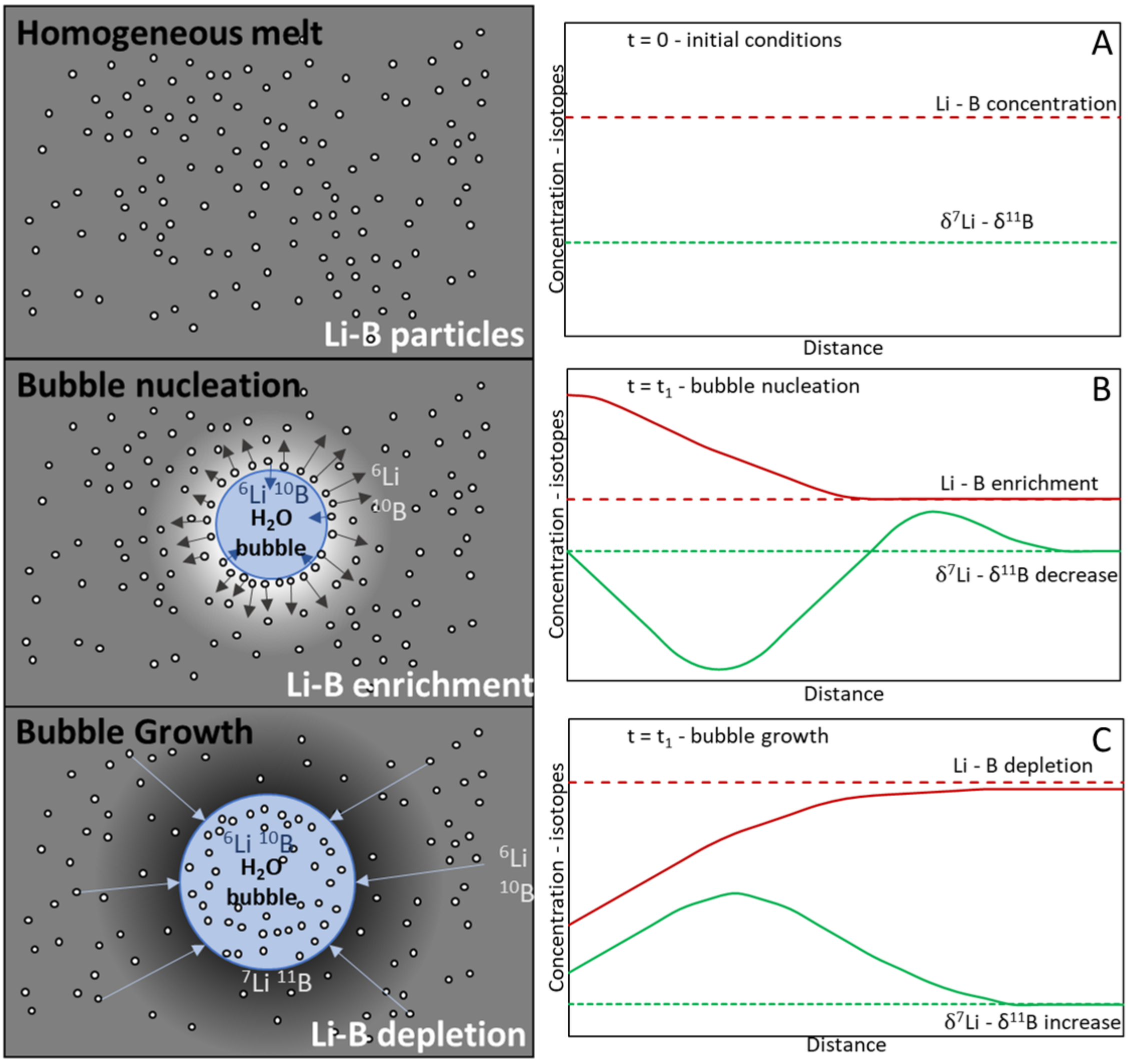

Figure 37: Summary of lithium and boron behaviour during the formation phases of bubbles in a decompressing silicate melt. (A) the initial melt at magma chamber conditions has an ideally homogeneous distribution of Li and B in the silicate melt. (B) When bubble nucleation occurs, during magmatic decompression, Li and B are pushed around the surrounding area. (C) When the bubble growth allows Li and B to diffuse into the bubble, a depletion of their concentration occurs.

would be necessary to further evaluate these profiles, as especially isotopic fractionation can have very small extension in terms of distance, hence some information might have been lost by the choice of the analytical setup.

In Figure 37, the main steps of the process of bubble nucleation and growth are schematically represented and summarize the progression of the process and the evolution of Li and B concentration and isotopic ratios. We start from an ideally homogeneous melt (Figure 37A), where the initial Li and B concentration is constant and the δ values are equal to 0. Here, the bubble nucleation is strongly dependent on the supersaturation pressure, and it occurs when the internal free energy of a bubble nucleus overcomes the free energy of the surface tension that prevents the separation of two phases (e.g. Gonnermann and Manga 2012).

We suggest that the initial enrichment in Li and B concentration in the area surrounding the bubbles, for the fast decompression experiment, is related to the dynamics of bubble nucleation, in its initial phase. The occurrence of a sufficiently high supersaturation pressure triggers bubble nucleation and water separates from the silicate melt into a gas phase, generating a bubble-melt interface. The initial volume expansion of the nucleated bubble causes a rapid advance of the bubble-melt interface. The growth rate of the bubble is faster than the diffusion of Li and B as well as partitioning into the fluid. Consequently, the lithium and boron in the melt adjacent to the bubble are rather pushed by the advancing bubble-melt interface than partitioned into the gas bubble, creating the accumulation noticed in Figure 36A and Figure 36B for the experiment DEC3.

Such an element accumulation at the interface has been observed in nature and laboratory experiments in the case of crystal growth in silicate melts (e.g. Tiller and Ahn, 1980; Watson and Liang, 1995). In that case, the incompatible elements which do not partition into the growing crystal accumulate at the melt-crystal interface, as the crystal progressively grows in its size. The chemistry of the crystallization process generates a depletion in certain elements and simultaneous enrichment of other components at the crystal-melt interface, depending on what is partitioning into the crystal during its growth(Watson and Müller, 2009). In the case of bubble growth during magmatic decompression, the process is driven by the kinetics of the bubble nucleation and growth. At the initial stage, the growth rate of the bubble is faster than the diffusivity of Li and B, hence an enrichment of the two elements close to the bubble is generated by the advancing bubble-melt interface (Figure 37B).

The simultaneous decrease in the δ^7Li and δ^{11}B in the 30-minute experiment has been interpreted as the combination of two processes of diffusion occurring simultaneously (Figure 37B). One diffusion process (initially minor) occurs from the melt to the newly formed gas phase, with Li and B partitioning into the bubble. The second process of diffusion takes place from the initially enriched melt close to the bubble to the unaltered melt, because of the sudden appearance of a Li and B concentration gradient between the bubble-melt interface and the unaffected melt. In this second event of diffusion from the bubble-melt interface to the host melt, ^{6}Li and ^{10}B diffuse faster into the melt, and simultaneously start fractionating into the growing bubble, generating a decrease in the δ^{7}Li and δ^{11}B values at the bubble-melt interface.

As the bubble volume expansion proceeds (Figure 37C), the growth rate of the gas bubble decreases, and the diffusive transport and melt-fluid partitioning take over as rate-limiting factors for the element distribution halo corroborated by the advancing interface. The area surrounding the bubble will be more affected by the elemental partitioning of Li and B into the bubble, generating a concentration depletion in the surrounding melt area. At this stage, the diffusion process of Li and B will be only going towards the bubble, as the melt halo is depleted in the two trace elements, compared to the starting host melt concentration.

While the initial accumulation phase was mainly controlled by the kinetics of the melt-bubble interface formation and the volume expansion of the bubble, this second phase is diffusion-dominated (Figure 37C). Here, the different mobility of the two elements starts to be evident, as the decompression time increases. While lithium diffusion is confirmed to be particularly fast, in the case of boron, the expectation was to notice some evidence of diffusion only for the longest experiment, considering the results obtained by the diffusion-couple experiments, previously discussed in chapter 4.3.1. Having observed a diffusion profile already after the two-hour decompression experiment it seems that boron partitioning between fluid and melt during bubble formation is a fast process, compared to the sole process of diffusion in a steady system. Hence, boron migration from the melt to the vapor phase is facilitated by the water exsolution process, during the nucleation and growth of the bubble. However, boron concentration and isotopic profiles of the two- and five-hour experiments are very similar, suggesting that boron diffusion is anyway slower than lithium’s and the general depletion of the overall concentration in the melt takes longer times compared to lithium.

In this phase of bubble growth, the isotopic ratios progressively increase because diffusive isotopic fractionation occurs between the melt and the gas phase, and the lighter isotopes (especially ^{6}Li) fractionate into the bubble. Hence, a gradual increase in the isotopic ratio will be observed, which is more evident for lithium compared to boron, where the isotopic ratio remains overall constant around the starting value in the case of the two- and five-hour decompression runs.

Ultimately, after a certain time, equilibrium will be reached between melt and gas phase, and the lithium and boron systems will be homogenised, with a constant but depleted concentration in the melt. The homogenised isotopic ratio might have the same value as before the decompression or, most likely, it might be higher than the starting isotope ratio, because of the preferential partitioning of the light isotope into the bubble. When homogenisation is reached, diffusion profiles are no longer visible in the melt. After the ten-hour decompression experiment, lithium seems to be already close to homogenisation and/or shows composite profiles overlapping with the ones generated by nearby bubbles that are close to the plane of the analysis. The slower diffusivity of B causes a slower process of homogenisation between the boron in the bubble and the surrounding melt. While lithium has already reached equilibrium concentration, boron exsolution is still an ongoing process, and the diffusion is still proceeding in its evolution for reaching equilibrium between bubble and melt.

Surprisingly, the two elements show the same behaviour despite having very different diffusivities and timescales. However, lithium is confirmed to have a faster mobility than boron, in agreement with the results of the diffusion-couple experiments presented in Chapter 4.2. In fact, in Figure 36A and Figure 36B the extension of the halo affected by lithium diffusion in the melt is approximately three times longer than the melt area affected by boron diffusion. The observations made in chapter 4.3 regarding boron isotopic fractionation during diffusion-couple experiments were not equally found in the samples obtained from decompression experiments. Whether the coordination and structural role of boron has an effect on its diffusion process into the growing bubbles, this does not seem to be visible in the final result. The concurrent water diffusion and partitioning into the bubbles during nucleation and growth could have a major effect on both concentration and isotopic behaviour of boron, which interact with the normal isotopic fractionation process.

5.3. Modelling Li and B in degassing magmas, preliminary considerations

The mathematical definition of the dynamics of bubble growth is an extensively studied topic of the last decades in volcanological research. Several models have been published, which try to correlate the dynamics of bubble formation with chemical partitioning or isotopic fractionation of different elements. Most of these models consider all volatile components as equally causing bubble growth, or only discuss a specific volatile component, such as H_2O or helium (e.g. Prousevitch et al. 1993; Proussevitch and Sahagian 1998; Gonnermann and Mukhopadhyay 2007). Among the different models, Watson (2017) well summarized the dynamics of the process, distinguishing between volatile components, which actively affect bubble growth (such as water and carbon dioxide) and passive components that are partitioned into the bubble during its volume expansion. In fact, active and passive volatile components need to be mathematically explained differently, because the first group has a significant effect on the dynamics of bubble growth and the diffusion process. On the contrary, the second group is only transported by diffusion (or advection, if the bubble is moving), with no direct effects on the vesiculation process. In order to evaluate whether the data of this study are applicable to the model of Watson (2017), a verification of the boundary conditions

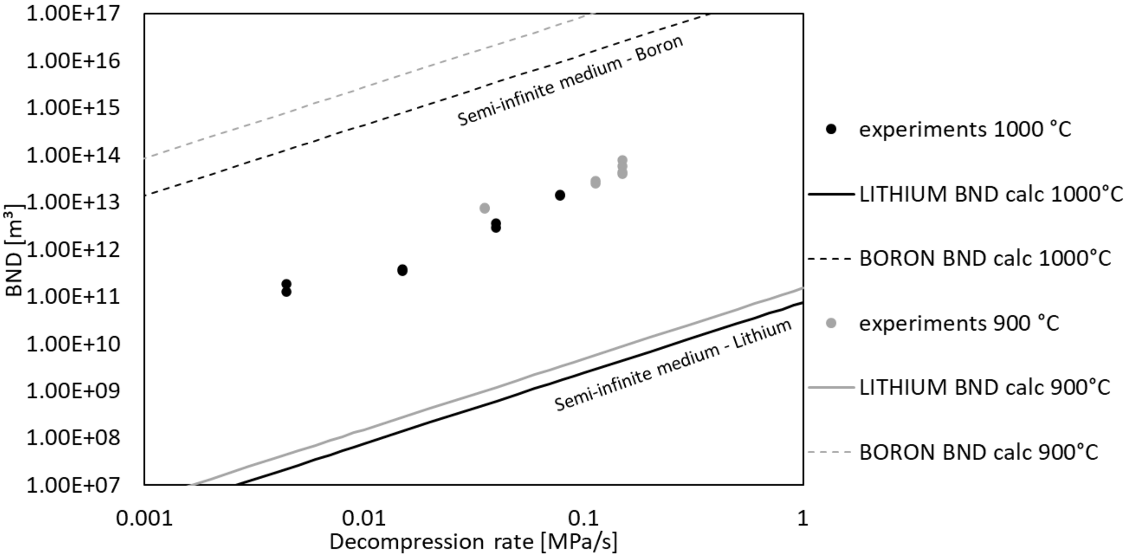

Figure 38: Decompression samples in relation to the limit of the semi-infinite medium approach, the dataset is placed in conditions where it is possible to use the semi-infinite medium boundary conditions for boron (dotted lines) but not for lithium, as the diffusion length is longer than half of the average distance between the bubbles.

of the model was necessary, especially focusing on the assumption that the melt can be considered a semi-infinite medium.

The semi-infinite medium assumption can be assessed by comparing two length scales, knowing the diffusion coefficients of Li and B in hydrous rhyolites: one is the expected diffusion length of the element, and the other is the half length of the average distance between one bubble wall to another. The average distance between bubble walls was calculated by taking the cubic root of the reciprocal value of BND, assuming that bubbles have a spherical volume around a nucleus. The diffusivity values obtained by the diffusion-couple experiments of this study were used in order to calculate an expected length of the diffusion profiles for the duration from the moment of nucleation to the quench. Li and B have clearly very different diffusion profile length, given the three orders of magnitude difference between the two diffusion coefficients (see Chapter 4.2, Table 2).

Figure 38 compares the length scales in units of BND; note that high BND corresponds to shorter length. The diffusion length scale is calculated for the duration of the decompression from ca. 90 MPa to the quench pressure (71-77 MPa), and the length is converted to BND. The lines of Figure 38 represent the case when the half-distance between bubble walls is the same as the diffusion length, at 1000°C and 900 °C. It is noticeable for lithium, that measured BND values plot above the model diffusion line at both temperatures. This indicates that the distance of the diffusion profile is longer than the half distance between bubbles. Boron shows the opposite situation, where the diffusion length is shorter than the half-distance between bubbles.

Figure 39 summarizes the different behaviour of lithium and boron in degassing magmas. Boron results represent most likely to be the only effect of the growth process of one bubble in the proximity, as the melt affected by boron diffusion never approaches the half distance between vesicles in the chosen decompression rates of this study (Figure 39A). In contrast, lithium profiles in our runs show interferences from the bubble growth process of neighbouring bubbles (Figure 39B). This is in good agreement with our concentration profiles of lithium and boron, as lithium has stronger effects of general depletion of the whole dataset, compared to boron that clearly shows such behaviour only for the ten-hour decompression run (DEC9).

The model of (Watson, 2017) is based on the initial boundary conditions of a semi-infinite model, where it is assumed that the diffusion profile is unaltered from other diffusion processes coming from other vesicles. In this study, this could be applied to boron system (Figure 39A), but not to lithium, as it must be considered that the observed profile is the result of the interaction of several bubble growth processes.

A second model was published with the same purpose of relating volatile components (H_2O-CO_2) to the process of bubble nucleation and growth during degassing (Yoshimura, 2015). In his study, Yoshimura (2015) presents a one-dimensional model in a plane sheet, where the melt-bubble interface is fixed, and the distance between two bubbles is considered as constant. The dynamics of bubble growth is not described by this numerical simulation, because it only describes the evolution of a generic volatile component with increasing decompression time. Yoshimura (2015) simplified the model by not considering the dynamics of expansion of the bubble itself, but only focusing on the loss of volatiles from the melt phase.

In the model, a generic ascending magma has initial concentration C_i^{ini} of the volatile component i. At time t=0 the generation of the bubble-melt interface will modify the volatile content to a new concentration C_i^{int}. The evolution of the concentration of the volatile component along the distance 2L between the two

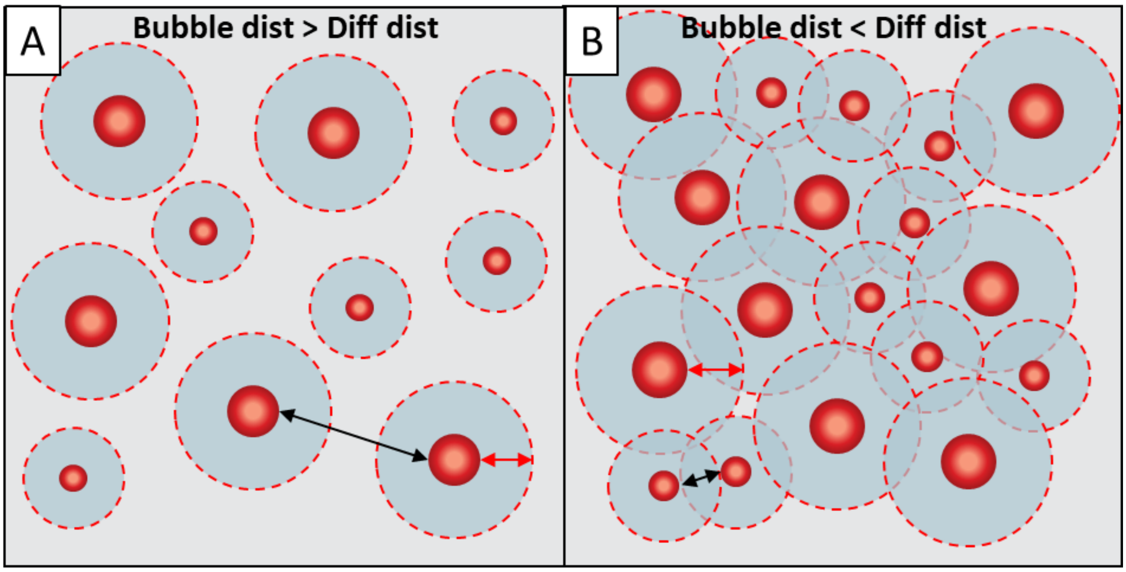

Figure 39: Sketch of the conditions where the boundary condition of the semi-infinite medium is applicable. In the left case, the distance between bubbles is longer than the diffusion profile, while in the second case, non-monotonous profiles are obtained, because they get interferences from the neighbouring bubbles around the studied one.

bubbles (where the two bubble-melt interfaces are placed at -L and +L) is described as follows (Yoshimura 2015):

$$C_i = C_i^{int} + \left(C_i^{ini} - C_i^{int}\right) \frac{4}{\pi} \sum_{n=0}^{\infty} \frac{(-1)^n}{2n+1} \exp\left[-(2n+1)^2 \pi^2 \left(\frac{Dt}{4L^2}\right)\right] \cos\left[\frac{(2n+1)\pi}{2} \frac{x}{L}\right] \quad 15$$

Where n are integer numbers (0, 1, 2…), C_i is the concentration of the volatile species at the position x and time t, while D_i is the diffusion coefficient of the studied volatile component.

This numerical simulation is applicable for different volatile species, as it mainly depends on the initial and interface concentration of the components and its diffusion coefficient at a given temperature. Using the software R-project[5], we applied this model to our system and to the single isotopes (^{6}Li, ^{7}Li, ^{10}B and ^{11}B), in order to reproduce the evolution of the concentration and the δ^7Li- δ^{11}B with increasing decompression time, as shown in Figure 40. In this figure, the model displays the half distance between the bubble walls, and the interface is placed at value 1 of the normalized distance. Only lithium is represented because it provided a more precise final concentration of homogenisation. Boron diffusion was slower, and it is unclear whether the value at the bubble-melt interface for the ten-hour decompression run could be noted as the final homogenisation concentration. Thus, boron final concentration was an approximate estimation, while lithium system provided a more precise post-diffusion concentration.

This model, different from Watson (2017), assumes that the diffusion process will be affected by elemental diffusion from a bubble positioned at the opposite side with respect to the direction of the process. What is not accounted for, is the initial phase of enrichment of the trace elements close to the interface area that is noticed in the profile results of our short decompression runs, as this was never observed before in the type of experiments performed in this study. Hence, the model does not consider this option. Furthermore, the element concentration at the interface is fixed for a simplification of the model, but the data presented in this study show that the concentration at the interface increases in the early bubble nucleation and growth phase and continuously decreases later until reaching the equilibrium concentration.

---

[5] https://www.r-project.org/

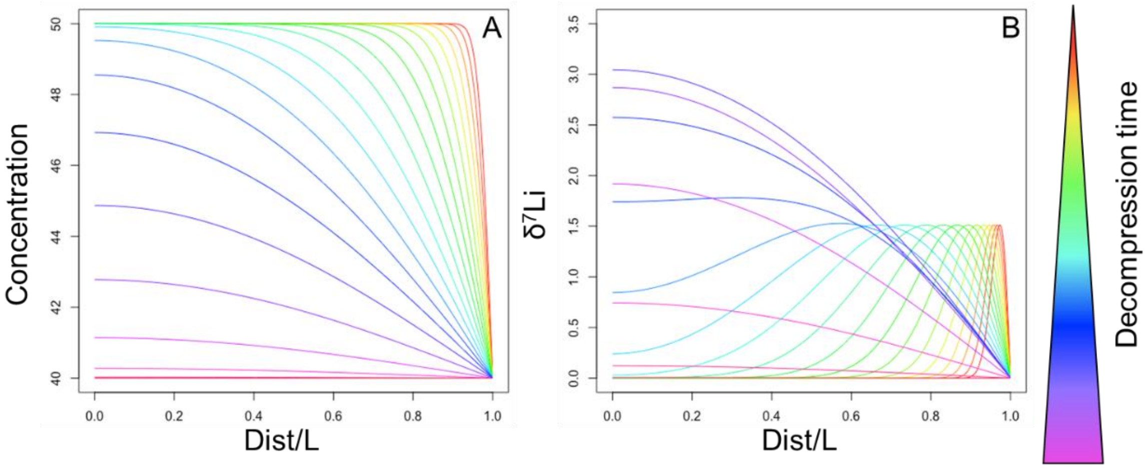

Figure 40: model of Yoshimura (2015) applied to the development of concentration and isotopic ratio of lithium during the bubble growth. The bubble meniscus corresponds to the Dist/L = 1 in the horizontal axis.

A modification of the model of Yoshimura (2015) is now in development, in order to give a better description of the data presented in this chapter. Figure 40A shows the continuous Li depletion in the melt, undergoing progressive general decrease of the concentration as the decompression time increases. At the same time, Figure 40B reports the variation of Li isotopic ratio. In this case, a sharp increase in the δ^7Li values close to the interface is highlighted, and this peak gradually widens as the decompression progresses. As the isotopic ratio continues to change, it starts decreasing by the interaction with the opposite diffusion process, until it reaches homogenisation and goes back to the initial value.

This model is still under further development, and several considerations have to be made in order to create a sufficiently precise simulation that is capable of describing the results observed in this study. The initial enrichment of the Li and B concentration and simultaneous depletion of the δ^7Li and δ^{11}B must be incorporated in the model. Hence, the concentration of Li and B at the melt-bubble interface cannot be fixed but has to vary with time and bubble growth progression. Furthermore, the effects of the initial phase of diffusion back in the unaltered melt have to be included in the model. Nonetheless, this is a good starting point to develop a very precise tool that uses Li and B exsolution process as a proxy to trace magmatic ascent rates.

5.4. Summary of decompression experiments

This chapter focused on the magmatic degassing process, in an attempt to correlate the behaviour of lithium and boron with the dynamics of magmatic ascent and decompression-driven degassing in volcanic systems.

Our first observations on the texture of the different samples showed that indeed the bubble size and distribution of the different samples is a function of the decompression rate. The temperature has been found to have a significant effect on the BND results, because it affects the saturation pressure at which a free fluid phase is formed, necessary to generate a saturation overpressure that leads to bubble nucleation sites. All the successful experiments have a final water concentration that agrees with the solubility curves at the run temperatures, meaning the degassing process in this study occurred at equilibrium.

Applying the model of Toramaru (2006) on the use of BND as a direct indicator of the decompression rates, the experimentally determined BND values have the same relation to the decompression rate as shown by the numerical simulation. A shift of the experimental data towards higher BND is noticeable, and probably caused by small artifacts in the model, as some parameters were either estimated or recalculated by other models.

Lithium and boron SIMS results show a progressive decrease of the concentration with decreasing decompression rates, meaning that longer decompressions get progressively more depleted in trace elements as the bubble size increases. This is consistent with a general idea that the more the bubbles expand their volume, the more the silicate melt will lose trace elements by diffusion and partitioning into the bubbles. Profile measurements of Li and B from the bubble meniscus to an ideally unaltered melt meniscus, show that the fast decompression runs present a trace element accumulation towards the bubble area, while longer decompression show a depletion in Li and B getting closer to the vesicle. The longest conducted decompression run shows that Li is approaching homogenisation, while boron still shows a consistent depletion profile. The results on the isotopic ratios show a general decrease in the Li and B isotopic ratio for the fast decompression, followed by a progressively heavier ratio for slower decompression runs.

We suggest that this behaviour is related to the sudden separation of the gas phase from the liquid phase, with an immediate creation of an interface. During the bubble nucleation phase, the melt particles that were replaced by the gas bubble were pushed around the newly formed interface, generating a passive enrichment between the area surrounding the bubble. The sudden occurrence of a chemical gradient between the melt at the bubble interface and the initial melt initiates a diffusion process in the opposite direction, causing a decrease in the isotopic ratio, as ^{6}Li diffuses faster than ^{7}Li. B isotope results show comparable results to Li, suggesting that in a decompressing system, boron isotopic fractionation is mainly controlled by the kinetics of bubble growth and the fluid-melt partitioning process, rather than the sole diffusion progression, as discussed in Chapter 4.

As the bubble growth proceeds, Li and B start to partition into the bubble, and progressively decrease their concentration in the melt area surrounding the vesicle, inverting the diffusion process: from the unaltered melt to the bubble area.

A first attempt of modelling was made in order to explain the results observed in this section, but the interaction of the selected bubble area with other neighbouring diffusion processes makes it difficult to realistically set the boundary conditions of the diffusion process (Yoshimura, 2015; Watson, 2017). Furthermore, no existing model consider an initial phase of accumulation of trace elements close to the bubble nucleation area, as this behaviour was never observed before.

6. Conclusions and Outlook

This study focused on the use of lithium and boron behaviour as a geochemical tracer during magmatic decompression-induced ascent in volcanic systems.

The results of our diffusion-couple experiments show that lithium and boron diffusivity is significantly enhanced by the presence of water in rhyolitic melts, with Lithium being an extremely fast-diffusing species and boron considerably slower, because of the different structural position in which the two elements are located and bonded in the silicate melt structure. Lithium was found to have an evident isotopic fractionation, caused by the fact that ^{6}Li diffuses faster than ^{7}Li in silicate melts. The B isotopes were more difficult to interpret, as no clear isotopic fractionation was observed. Several hypotheses have been proposed, but further studies and new diffusion-couple experiments would be necessary to clearly define what are the factors playing a role in boron diffusive isotopic fractionation.

Decompression experiments performed in homogeneous degassing conditions showed that the experimentally determined BND values are directly proportional to the magmatic decompression rate. Li and B show a progressive decrease of their concentration with decreasing decompression rates, indicating that depleted systems tend to have a slower ascent, compared to volcanic products generally enriched in Li and B.

Comparing the profile measurements of each experiment, an increase in the Li and B concentration is noticeable for the fastest runs, which was attributed to the nucleation process, with a sudden formation of a gas bubble that pushed Li and B around the newly formed interface. This causes the occurrence of an inverse diffusion process, from the bubble meniscus to the homogeneous melt. Longer decompressions show a depletion of Li and B close to the melt/gas interface, attributed to the progressive diffusive and kinetic transport of Li and B from the unaltered melt to the gas phase.

The lithium profile after a ten-hour decompression experiment shows evidence of homogenisation or interaction between multiple neighbouring bubbles. Slower decompression rates would hardly show a distinct diffusion profile because, because this would be affected by several processes of bubble growth, or by complete homogenisation (when diffusive transport is the rate-limiting factor). Therefore, lithium could be mainly used for fast decompressions, generally higher than 0.1 MPa/s. Conversely, boron can be suited for significantly small decompression rates, as the results observed in this study seemed to be far from homogenisation of its system in our decompression experiments.

Numerical models have been applied to this system, but several modifications are currently being studied, in order to better reproduce our observed results. The best suited model which works for this system is not suited to describe the initial phase of accumulation of Li and B observed for the fast decompression, and it would cause an underestimation of the temporal evolution of the concentration, if used for the slow decompressions. Furthermore, it will serve as basis to develop a series of modifications which will allow to accurately describe the experimentally observed results if this study and will help to better constrain the behaviour of trace elements in ascending magmas.

Open questions and further improvement suggestions

The results of this study provide a very good starting point to continue to develop a tool to trace the magmatic ascent, by the study of the diffusion of Li for fast ascent, and B for slow ascent. Lithium and boron are not easy to measure, but the constant advance in the analytical techniques has been incredibly fast in the last decades and could help in the future to get more precise analyses of Li and B concentration and isotopes. Several aspects of this study can be improved in order to get a more complete knowledge of this theme and allow to develop a more precise geochemical tracer for magmatic ascent in volcanic systems. Decompression and/or diffusion-couple experiments with longer or shorter duration could give new insights and additional information when combined with our results. Moreover, it would be interesting to carry out a similar research study on basaltic systems and compare our results with systems that have a different chemical composition and lower degree of polymerization.

Finally, It is incredibly rare that natural volcanoes erupt products that underwent homogeneous degassing, with no crystals and homogeneously distributed bubbles. Commonly, pre-existing bubbles or minerals affect the dynamics of bubble nucleation and growth during decompression (e.g., Cichy, 2011; Cichy et al., 2011). Several studies state that bubble nucleation is a mostly heterogeneous process (e.g. Shea 2017), hence the findings of this study give a great initial starting point to continue developing this method, but are still simplified in comparison to natural systems. Oxide crystals as well as CO_2 can be added to the starting materials, in order to modify the bubble nucleation and growth process, and most likely the response of Li and B to heterogeneous degassing, as shown by the failed decompression experiments (Figure 28) in this study. Moreover, several aspects of boron isotopic fractionation are still unclear and not well constrained. Hence, further diffusion-couple experiments with longer durations as well as studies on the interaction between diffusion and fluid-melt partitioning at the interface would be needed in order to better constrain all steps and clearly understand the dynamics. The use of numerical models can be of great help, as they can provide information about parameters that are difficult to characterize using a purely experimental approach.

Finally, lithium and boron contents in volcanic systems are still not well constrained up to these days. It is therefore complicated to evaluate what is the state of degassing of the erupted products, without knowing what the initial content of lithium and boron was. Thus, it would be important to carry on an extensive study on the pre-eruptive concentrations of lithium and boron in different volcanic systems, through the study of melt inclusions or embayments. In conclusion, lithium and boron can be used as a complementary support to the study of the BND in relation to the decompression rate in degassing magmas. These elements constitute a promising tool to precisely trace ascent rates and degassing related processes in volcanic systems.

7. Reference list

Acevedo, F. C. (2020). The role of nano- to millimetre sized crystals on the dynamic evolution of shallow silica-rich magma: Implications for volcanic eruptions. München, Ludwig-Maximilians-Universität. 10.5282/edoc.26507

Anderson, G. M. (1976). Error propagation by the Monte Carlo method in geochemical calculations. *Geochimica et Cosmochimica Acta* **40**, 1533–1538. 10.1016/0016-7037(76)90092-2

Angeli, F., Charpentier, T., De Ligny, D. & Cailleteau, C. (2010). Boron Speciation in Soda-Lime Borosilicate Glasses Containing Zirconium. *Journal of the American Ceramic Society* **93**, 2693–2704. 10.1111/j.1551-2916.2010.03771.x

Armienti, P. (2008). Decryption of Igneous Rock Textures: Crystal Size Distribution Tools. *Reviews in Mineralogy and Geochemistry* **69**, 623–649. 10.2138/rmg.2008.69.16

Armienti, P., Perinelli, C. & Putirka, K. D. (2013). A New Model to Estimate Deep-level Magma Ascent Rates, with Applications to Mt. Etna (Sicily, Italy). *Journal of Petrology* **54**, 795–813. 10.1093/petrology/egs085

Bagdassarov, N., Dorfman, A. & Dingwell, D. B. (2000). Effect of alkalis, phosphorus, and water on the surface tension of haplogranite melt. *American Mineralogist*. De Gruyter **85**, 33–40. 10.2138/am-2000-0105

Baker, D. R. (1992). Tracer diffusion of network formers and multicomponent diffusion in dacitic and rhyolitic melts. *Geochimica et Cosmochimica Acta* **56**, 617–631. 10.1016/0016-7037(92)90086-X

Baker, D. R. & Bossányi, H. (1994). The combined effect of F and H_2O on interdiffusion between peralkaline dacitic and rhyolitic melts. *Contributions to Mineralogy and Petrology* **117**, 203–214. 10.1007/BF00286843

Behrens, H., Roux, J., Neuville, D. R. & Siemann, M. (2006). Quantification of dissolved H_2O in silicate glasses using confocal microRaman spectroscopy. *Chemical Geology* **229**, 96–112. 10.1016/j.chemgeo.2006.01.014

Behrens, H. & Haack, M. (2007). Cation diffusion in soda-lime-silicate glass melts. *Journal of Non-Crystalline Solids* **353**, 4743–4752. 10.1016/j.jnoncrysol.2007.05.178

Berndt, J., Liebske, C., Holtz, F., Freise, M., Nowak, M., Ziegenbein, D., Hurkuck, W. & Koepke, J. (2002). A combined rapid-quench and H_2-membrane setup for internally heated pressure vessels: Description and application for water solubility in basaltic melts. *American Mineralogist*. De Gruyter **87**, 1717–1726. 10.2138/am-2002-11-1222

Bird, R. B., Stewart, W. E. & Lightfoot, E. N. (2006). *Transport Phenomena*. John Wiley & Sons.

Bista, S., Morin, E. I. & Stebbins, J. F. (2016). Response of complex networks to compression: Ca, La, and Y aluminoborosilicate glasses formed from liquids at 1 to 3 GPa pressures. *The Journal of Chemical Physics* **144**, 044502. 10.1063/1.4940691

Bradshaw, R. W., Kent, A. J. R. (2017). The analytical limits of modeling short diffusion timescales. *Chemical Geology, 466, 667-677.* https://doi.org/10.1016/j.chemgeo.2017.07.018

Chakraborty, S., Dingwell, D. B. & Chaussidon, M. (1993). Chemical diffusivity of boron in melts of haplogranitic composition. *Geochimica et Cosmochimica Acta* **57**, 1741–1751. 10.1016/0016-7037(93)90110-I

Chakraborty, S. (1995). Chapter 10. Diffusion in Silicate Melts. In: Stebbins, J. F., McMillan, P. F. & Dingwell, D. B. (eds) *Structure, Dynamics, and Properties of Silicate Melts*. De Gruyter, 411–504. 10.1515/9781501509384-012

Chakraborty, S. (1997). Rates and mechanisms of Fe-Mg interdiffusion in olivine at 980°–1300°C. *Journal of Geophysical Research: Solid Earth* **102**, 12317–12331. 10.1029/97JB00208

Cichy, S. B. (2011). Experimental study on vesiculation and formation of groundmass microlites induced by decompression: Constraints on processes related to magma ascent at Unzen volcano. Hannover, Gottfried Wilhelm Leibniz Universität. 10.15488/7602

Cichy, S. B., Botcharnikov, R. E., Holtz, F. & Behrens, H. (2011). Vesiculation and Microlite Crystallization Induced by Decompression: a Case Study of the 1991–1995 Mt Unzen Eruption (Japan). *Journal of Petrology* **52**, 1469–1492.

Cornelius, M. (2006). Techniques for embedding instrumentation in pressure vessel test articles. In: Korman, V. (ed.) paper presented at the Defense and Security Symposium. Orlando (Kissimmee), FL, 622205. 10.1093/petrology/egq072

Costa, F. (2008). Residence times of silicic magmas associated with calderas. In: Caldera Volcanism: Analysis, Modelling and Response. *Gottsmann J, Marti J (eds), Developments in Volcanology* 55.

Costa, F., Shea, T. & Ubide, T. (2020). Diffusion chronometry and the timescales of magmatic processes. *Nature Reviews Earth & Environment* **1**, 201–214. 10.1038/s43017-020-0038-x

Crank, J. (1975). *The mathematics of diffusion*. Oxford, [Eng]: Clarendon Press. 10.2307/3609455

Cunningham, G. J., Henderson, P., Lowry, R. K., Nolan, J., Reed, S. J. B. & Long, J. V. P. (1983). Lithium diffusion in silicate melts. *Earth and Planetary Science Letters* **65**, 203–205. 10.1016/0012-821X(83)90199-1

Dell, W. J. & Xiao, S. Z. (1983). ^{11}B NMR studies and structural modeling of Na_2O-B_2O_3-SiO_2 Glasses of high soda content. *Journal of Non-Crystalline Solids* **58**, 1–16. 10.1016/0022-3093(83)90097-2

Dingwell, D. B. (2006). Transport Properties of Magmas: Diffusion and Rheology. *Elements* **2**, 281–286. 10.2113/gselements.2.5.281

Dohmen, R. & Chakraborty, S. (2007). Fe–Mg diffusion in olivine II: point defect chemistry, change of diffusion mechanisms and a model for calculation of diffusion coefficients in natural olivine. *Physics and Chemistry of Minerals* **34**, 409–430. 10.1007/s00269-007-0158-6

Doremus, R. H. (1966). Physical Solubility of Gases in Fused Silica. *Journal of the American Ceramic Society* **49**, 461–462. 10.1111/j.1151-2916.1966.tb13299.x

Endo, E. T. & Murray, T. (1991). Real-time Seismic Amplitude Measurement (RSAM): a volcano monitoring and prediction tool. *Bulletin of Volcanology* **53**, 533–545. 10.1007/BF00298154

Fanara, S., Sottili, G., Silleni, A., Palladino, D. M. & Schmidt, B. C. (2017). CO_2 bubble nucleation upon pressure release in potassium-rich silicate magmas. *Chemical Geology* **461**, 171–181. 10.1016/j.chemgeo.2016.12.033

Fick, A. (1855). Ueber Diffusion. *Annalen der Physik* **170**, 59–86. 10.1002/andp.18551700105

Fiege, A., Holtz, F. & Cichy, S. B. (2014). Bubble formation during decompression of andesitic melts. *American Mineralogist* **99**, 1052–1062. 10.2138/am.2014.4719

Fiege, A. & Cichy, S. B. (2015). Experimental constraints on bubble formation and growth during magma ascent: A review. *American Mineralogist* **100**, 2426–2442. 10.2138/am-2015-5296

Foster, G. L., Marschall, H. R. & Palmer, M. R. (2018). Boron Isotope Analysis of Geological Materials. In: Marschall, H. & Foster, G. (eds) *Boron Isotopes*. Cham: Springer International Publishing, 13–31. 10.1007/978-3-319-64666-4_2

Gardner, J. E., Hilton, M. & Carroll, M. R. (1999). Experimental constraints on degassing of magma: isothermal bubble growth during continuous decompression from high pressure. *Earth and Planetary Science Letters* **168**, 201–218. 10.1016/S0012-821X(99)00051-5

Giletti, B. J. & Shanahan, T. M. (1997). Alkali diffusion in plagioclase feldspar. *Chemical Geology* **139**, 3–20. 10.1016/S0009-2541(97)00026-0

Gillis, K. M., Coogan, L. A. & Chaussidon, M. (2003). Volatile element (B, Cl, F) behaviour in the roof of an axial magma chamber from the East Pacific Rise. *Earth and Planetary Science Letters* **213**, 447–462. 10.1016/S0012-821X(03)00346-7

Giordano, D., Russell, J. K. & Dingwell, D. B. (2008). Viscosity of magmatic liquids: A model. *Earth and Planetary Science Letters* **271**, 123–134. 10.1016/j.epsl.2008.03.038

Gonnermann, H. & Manga, M. (2005). Nonequilibrium magma degassing: Results from modeling of the ca. 1340 A.D. eruption of Mono Craters, California. *Earth and Planetary Science Letters* **238**, 1–16.

Gonnermann, H. M. & Manga, M. (2007). The Fluid Mechanics Inside a Volcano. *Annual Review of Fluid Mechanics* **39**, 321–356. 10.1146/annurev.fluid.39.050905.110207

Gonnermann, H. M. & Mukhopadhyay, S. (2007). Non-equilibrium degassing and a primordial source for helium in ocean-island volcanism. *Nature*. Nature Publishing Group **449**, 1037–1040. 10.1038/nature06240

Gonnermann, H. M. & Manga, M. (2012). Dynamics of magma ascent in the volcanic conduit. *Modeling Volcanic Processes: The Physics and Mathematics of Volcanism*. Cambridge: Cambridge University Press. 10.1017/CBO9781139021562

Gonnermann, H. M. (2015). Magma Fragmentation. *Annual Review of Earth and Planetary Sciences* **43**, 431–458. 10.1146/annurev-earth-060614-105206

Hamada, M., Laporte, D., Cluzel, N., Koga, K. T. & Kawamoto, T. (2010). Simulating bubble number density of rhyolitic pumices from Plinian eruptions: constraints from fast decompression experiments. *Bulletin of Volcanology* **72**, 735–746. 10.1007/s00445-010-0353-z

Hervig, R. L., Moore, G. M., Williams, L. B., Peacock, S. M., Holloway, J. R. & Roggensack, K. (2002). Isotopic and elemental partitioning of boron between hydrous fluid and silicate melt. *American Mineralogist* **87**, 769–774. 10.2138/am-2002-5-620

Higgins, M. D. (2000). Measurement of crystal size distributions. *American Mineralogist* **85**, 1105–1116. 10.2138/am-2000-8-901

Holloway, J. R. (1971). Internally Heated Pressure Vessels. In: Ulmer, G. C. (ed.) *Research Techniques for High Pressure and High Temperature*. Berlin, Heidelberg: Springer, 217–258. 10.1007/978-3-642-88097-1_8

Holycross, M. E., Watson, E. B., Richter, F. M. & Villeneuve, J. (2018). Diffusive fractionation of Li isotopes in wet, silicic melts. *Geochemical Perspectives Letters* **6**, 39–42. 10.7185/geochemlet.1807

Huppert, H. E. & Woods, A. W. (2002). The role of volatiles in magma chamber dynamics. *Nature* **420**, 493–495. 10.1038/nature01211

Hurwitz, S. & Navon, O. (1994). Bubble nucleation in rhyolitic melts: Experiments at high pressure, temperature, and water content. *Earth and Planetary Science Letters* **122**, 267–280. 10.1016/0012-821X(94)90001-9

Ihinger, P. D., Zhang, Y. & Stolper, E. M. (1999). The speciation of dissolved water in rhyolitic melt. *Geochimica et Cosmochimica Acta* **63**, 3567–3578. 10.1016/S0016-7037(99)00277-X

Jambon, A. & Semet, M. P. (1978). Lithium diffusion in silicate glasses of albite, orthoclase, and obsidian composition: An ion-microprobe determination. *Earth and Planetary Science Letters* **37**, 445–450. 10.1016/0012-821X(78)90060-2

Jochum, K. P. *et al.* (2011). Determination of Reference Values for NIST SRM 610-617 Glasses Following ISO Guidelines. *Geostandards and Geoanalytical Research* **35**, 397–429. 10.1111/j.1751-908X.2011.00120.x

Jollands, M.C., (2020) Assessing analytical convolution effects in diffusion studies: Applications to experimental and natural diffusion profiles. PLoS ONE 15(11): e0241788. https://doi.org/10.1371/journal.pone.0241788

Kakihana, H., Kotaka, M., Satoh, S., Nomura, M. & Okamoto, M. (1977). Fundamental studies on the Ion-Exchange separation of boron isotopes. *Bulletin of the Chemical society of Japan* **50**, 158–163. 10.1246/bcsj.50.158

Kauzmann, W. & Eyring, H. (1940). The Viscous Flow of Large Molecules. *Journal of the American Chemical Society* **62**, 3113–3125. 10.1021/ja01868a059

Koga, K. T., Rose-Koga, E. F., Laporte, D., Cluzel, N. & Deloule, E. (2011). Lithium-boron isotope fractionation during degassing of rhyolitic magma. paper presented at the Goldschmidt. Prague.

Kowalski, P. M., Wunder, B. & Jahn, S. (2013). Ab initio prediction of equilibrium boron isotope fractionation between minerals and aqueous fluids at high P and T. *Geochimica et Cosmochimica Acta* **101**, 285–301. 10.1016/j.gca.2012.10.007

Kuritani, T. & Nakamura, E. (2006). Elemental fractionation in lavas during post-eruptive degassing: Evidence from trachytic lavas, Rishiri Volcano, Japan. *Journal of Volcanology and Geothermal Research* **149**, 124–138. 10.1016/j.jvolgeores.2005.06.008

Lautze, N. C., Sisson, T. W., Mangan, M. T. & Grove, T. L. (2011). Segregating gas from melt: an experimental study of the Ostwald ripening of vapor bubbles in magmas. *Contributions to Mineralogy and Petrology* **161**, 331–347. 10.1007/s00410-010-0535-x

Le Losq, C., Neuville, D. R., Moretti, R. & Roux, J. (2012). Determination of water content in silicate glasses using Raman spectrometry: Implications for the study of explosive volcanism. *American Mineralogist* **97**, 779–790. 10.2138/am.2012.3831

Le Losq, C., Mysen, B. O. & Cody, G. D. (2015). Water and magmas: insights about the water solution mechanisms in alkali silicate melts from infrared, Raman, and 29Si solid-state NMR spectroscopies. *Progress in Earth and Planetary Science* **2**, 22. 10.1186/s40645-015-0052-7

Lécuyer, C. (2016). Boron. In: Bobrowsky, P. & Marker, B. (eds) *Encyclopedia of geochemistry*. Cham: Springer International Publishing, 1–6. 10.1007/978-3-319-39193-9_253-1

Lesher, C. E. & Spera, F. J. (2015). Thermodynamic and Transport Properties of Silicate Melts and Magma. *The Encyclopedia of Volcanoes*. Elsevier, 113–141. 10.1016/B978-0-12-385938-9.00005-5

Liang, Y. (2017). Diffusion. In: Bobrowsky, P. & Marker, B. (eds) *Encyclopedia of Engineering Geology*. Cham: Springer International Publishing, 1–13. 10.1007/978-3-319-39193-9_336-1

Lockwood, J. P. & Hazlett, R. W. (2010). *Volcanoes: Global Perspectives* | *Wiley*. Wiley-Blackwell.

Mangan, M. & Sisson, T. (2000). Delayed, disequilibrium degassing in rhyolite magma: decompression experiments and implications for explosive volcanism. *Earth and Planetary Science Letters* **183**, 441–455. 10.1016/S0012-821X(00)00299-5

Marschall, H. R., Altherr, R. & Rüpke, L. (2007). Squeezing out the slab — modelling the release of Li, Be and B during progressive high-pressure metamorphism. *Chemical Geology* **239**, 323–335. 10.1016/j.chemgeo.2006.08.008

Marschall, H. & Foster, G. (eds) (2018). *Boron Isotopes*. Cham: Springer International Publishing. 10.1007/978-3-319-64666-4_1

Marxer, H., Bellucci, P. & Nowak, M. (2014). Degassing of H_2O in a phonolitic melt: A closer look at decompression experiments. *Journal of Volcanology and Geothermal Research* **297**, 109–124. 10.1016/j.jvolgeores.2014.11.017

Mehrer, H. (2007). *Diffusion in Solids: Fundamentals, Methods, Materials, Diffusion-Controlled Processes*. Springer Science & Business Media. 10.1007/978-3-540-71488-0

Menard, G., Vlastélic, I., Ionov, D. A., Rose-Koga, E. F., Piro, J.-L. & Pin, C. (2013). Precise and accurate determination of boron concentration in silicate rocks by direct isotope dilution ICP-MS: Insights into the B budget of the mantle and B behavior in magmatic systems. *Chemical Geology* **354**, 139–149. 10.1016/j.chemgeo.2013.06.017

Mills, K. C., Hayashi, M., Wang, L. & Watanabe, T. (2014). The Structure and Properties of Silicate Slags. *Treatise on Process Metallurgy*. Elsevier, 149–286. 10.1016/B978-0-08-096986-2.00008-4

Mollo, S., Vetere, F., Behrens, H., Tecchiato, V., Langone, A., Scarlato, P. & Perugini, D. (2017). The effect of degassing and volatile exsolution on the composition of a trachybasaltic melt decompressed at slow and fast rates. *Periodico di Mineralogia* **86**. 10.2451/2017PM691

Mourtada-Bonnefoi, C. C. & Laporte, D. (1999). Experimental study of homogeneous bubble nucleation in rhyolitic magmas. *Geophysical Research Letters* **26**, 3505–3508. 10.1029/1999GL008368

Mourtada-Bonnefoi, C. C. & Laporte, D. (2002). Homogeneous bubble nucleation in rhyolitic magmas: An experimental study of the effect of H_2O and CO_2. *Journal of Geophysical Research: Solid Earth* **107**, ECV 2-1-ECV 2-19. 10.1029/2001JB000290

Mourtada-Bonnefoi, C. C. & Laporte, D. (2004). Kinetics of bubble nucleation in a rhyolitic melt: an experimental study of the effect of ascent rate. *Earth and Planetary Science Letters* **218**, 521–537. 10.1016/S0012-821X(03)00684-8

Mungall, J. E., Dingwell, D. B. & Chaussidon, M. (1999). Chemical diffusivities of 18 trace elements in granitoid melts. *Geochimica et Cosmochimica Acta* **63**, 2599–2610. 10.1016/S0016-7037(99)00209-4

Mungall, J. E. (2002). Empirical models relating viscosity and tracer diffusion in magmatic silicate melts. *Geochimica et Cosmochimica Acta* **66**, 125–143. 10.1016/S0016-7037(01)00736-0

Mysen, B. O., virgo, D., Harrison, W. J. & Scarfe, C. M. (1980). Solubility mechanisms of H_2O in silicate melts at high pressures and temperatures: a Raman spectroscopic study. *American Mineralogist* **65**, 900–914.

Mysen, B. O. & Richet, P. (2019). *Silicate Glasses and Melts*. Elsevier. 10.1016/C2018-0-00864-6

Namiki, A. & Manga, M. (2006). Influence of decompression rate on the expansion velocity and expansion style of bubbly fluids. *Journal of Geophysical Research: Solid Earth* **111**. 10.1029/2005JB004132

Neave, D. A. & Maclennan, J. (2020). Clinopyroxene Dissolution Records Rapid Magma Ascent. *Frontiers in Earth Science* **8**, 188. 10.3389/feart.2020.00188

Newman, S. & Lowenstern, J. B. (2002). VolatileCalc: a silicate melt–H_2O–CO_2 solution model written in Visual Basic for excel. *Computers & Geosciences* **28**, 597–604. 10.1016/S0098-3004(01)00081-4

Ni, H., Hui, H. & Steinle-Neumann, G. (2015). Transport properties of silicate melts. *Reviews of Geophysics* **53**, 715–744. 10.1002/2015RG000485

Noguchi, S., Toramaru, A. & Nakada, S. (2008). Relation between microlite textures and discharge rate during the 1991–1995 eruptions at Unzen, Japan. *Journal of Volcanology and Geothermal Research* **175**, 141–155. 10.1016/j.jvolgeores.2008.03.025

Nowak, M. & Behrens, H. (2000). Water in rhyolitic magmas: getting a grip on a slippery problem. *Earth and Planetary Science Letters* **184**, 515–522. 10.1016/S0012-821X(00)00343-5

Nowak, M., Cichy, S. B., Botcharnikov, R. E., Walker, N. & Hurkuck, W. (2011). A new type of high-pressure low-flow metering valve for continuous decompression: First experimental results on degassing of rhyodacitic melts. *American Mineralogist* **96**, 1373–1380. 10.2138/am.2011.3786

Ottonello, G., Richet, P. & Papale, P. (2018). Bulk solubility and speciation of H_2O in silicate melts. *Chemical Geology* **479**, 176–187. 10.1016/j.chemgeo.2018.01.008

Paton, C., Hellstrom, J., Paul, B., Woodhead, J. & Hergt, J. (2011). Iolite: Freeware for the visualisation and processing of mass spectrometric data. *Journal of Analytical Atomic Spectrometry* **26**, 2508. 10.1039/c1ja10172b

Prousevitch, A. A., Sahagian, D. L. & Anderson, A. T. (1993). Dynamics of diffusive bubble growth in magmas: Isothermal case. *Journal of Geophysical Research: Solid Earth* **98**, 22283–22307. 10.1029/93JB02027

Proussevitch, A. A. & Sahagian, D. L. (1998). Dynamics and energetics of bubble growth in magmas: Analytical formulation and numerical modeling. *Journal of Geophysical Research: Solid Earth* **103**, 18223–18251. 10.1029/98JB00906

Puls, I. S. & Eckert, H. (2007). Spatial distribution of lithium ions in glasses studied by ^{7}Li{^{6}Li} spin echo double resonance. *Physical Chemistry Chemical Physics* **9**, 3992. 10.1039/b705338j

Pyle, D. M. (1992). The volume and residence time of magma beneath active volcanoes determined by decay-series disequilibria methods. *Earth and Planetary Science Letters* **112**, 61–73. 10.1016/0012-821X(92)90007-I

Richter, F. M., Liang, Y. & Davis, A. M. (1999). Isotope fractionation by diffusion in molten oxides. *Geochimica et Cosmochimica Acta* **63**, 2853–2861. 10.1016/S0016-7037(99)00164-7

Richter, F. M., Davis, A. M., DePaolo, D. J. & Watson, E. B. (2003). Isotope fractionation by chemical diffusion between molten basalt and rhyolite. *Geochimica et Cosmochimica Acta* **67**, 3905–3923. 10.1016/S0016-7037(03)00174-1

Richter, F., Watson, B., Chaussidon, M., Mendybaev, R. & Ruscitto, D. (2014). Lithium isotope fractionation by diffusion in minerals. Part 1: Pyroxenes. *Geochimica et Cosmochimica Acta* **126**, 352–370. 10.1016/j.gca.2013.11.008

Richter, F., Chaussidon, M., Watson, B. E., Mendybaev, R. & Homolova, V. (2017). Lithium isotope fractionation by diffusion in minerals Part 2: Olivine. *Geochimica et Cosmochimica Acta* **219**, 124–142. 10.1016/j.gca.2017.09.001

Rogers, N. (2015). The Composition and Origin of Magmas. *The Encyclopedia of Volcanoes*. Elsevier, 93–112. 10.1016/B978-0-12-385938-9.00004-3

Ross, S., Welsch, A.-M. & Behrens, H. (2015). Lithium conductivity in glasses of the Li_2O–Al_2O_3–SiO_2 system. *Physical Chemistry Chemical Physics* **17**, 465–474. 10.1039/C4CP03609C

Schiavi, F., Bolfan-Casanova, N., Withers, A. C., Médard, E., Laumonier, M., Laporte, D., Flaherty, T. & Gómez-Ulla, A. (2018). Water quantification in silicate glasses by Raman spectroscopy: Correcting for the effects of confocality, density and ferric iron. *Chemical Geology* **483**, 312–331. 10.1016/j.chemgeo.2018.02.036

Schmidt, B. C., Zotov, N. & Dupree, R. (2004). Structural implications of water and boron dissolution in albite glass. *Journal of Non-Crystalline Solids* **337**, 207–219. 10.1016/j.jnoncrysol.2004.04.007

Schmidt, B. C. & Behrens, H. (2008). Water solubility in phonolite melts: Influence of melt composition and temperature. *Chemical Geology* **256**, 259–268. 10.1016/j.chemgeo.2008.06.043

Schmincke, H.-U. (2004). *Volcanism*. Springer Science & Business Media. doi.org/10.1007/978-3-642-18952-4

Schulze, F., Behrens, H., Holtz, F., Roux, J. & Johannes, W. (1996). The influence of H_2O on the viscosity of a haplogranitic melt. *American Mineralogist* **81**, 1155–1165. 10.2138/am-1996-9-1014

Shackelford, J. F., Studt, P. L. & Fulrath, R. M. (1972). Solubility of Gases in Glass. II. He, Ne, and H_2 in Fused Silica. *Journal of Applied Physics*. American Institute of Physics **43**, 1619–1626. 10.1063/1.1661371

Shea, T. (2017). Bubble nucleation in magmas: A dominantly heterogeneous process? *Journal of Volcanology and Geothermal Research* **343**, 155–170. 10.1016/j.jvolgeores.2017.06.025

Shewmon, P. G. (1963). *Diffusion in Solids*. McGraw-Hill. 10.1007/978-3-319-48206-4

Spilliaert, N., Allard, P., Métrich, N. & Sobolev, A. V. (2006). Melt inclusion record of the conditions of ascent, degassing, and extrusion of volatile-rich alkali basalt during the powerful 2002 flank eruption of Mount Etna (Italy). *Journal of Geophysical Research* **111**, B04203. http://doi.wiley.com/10.1029/2005JB003934

Stanton, T. R. (1990). High-pressure, isotopic studies of the water diffusion mechanism in silicate melts and glasses. Arizona State University.

Stolper, E. (1989). Temperature dependence of the speciation of water in rhyolitic melts and glasses. *American Mineralogist* **74**, 1247–1257.

Teasdale, R., van der Hoeven Kraft, K. & Poland, M. P. (2015). Using near-real-time monitoring data from Puʻu ʻŌʻō vent at Kīlauea Volcano for training and educational purposes. *Journal of Applied Volcanology* **4**, 11. 10.1186/s13617-015-0026-x

Tiller, W. A. & Ahn, K.-S. (1980). Interface field effects on solute redistribution during crystallization. *Journal of Crystal Growth* **49**, 483–501. 10.1016/0022-0248(80)90123-2

Toramaru, A. (1995). Numerical study of nucleation and growth of bubbles in viscous magmas. *Journal of Geophysical Research: Solid Earth* **100**, 1913–1931. 10.1029/94JB02775

Toramaru, A. (2006). BND (bubble number density) decompression rate meter for explosive volcanic eruptions. *Journal of Volcanology and Geothermal Research* **154**, 303–316. 10.1016/j.jvolgeores.2006.03.027

Toramaru, A. (2022). *Vesiculation and Crystallization of Magma*. Singapore: Springer. 10.1007/978-981-16-4209-8_2

Vlastélic, I., Staudacher, T., Bachèlery, P., Télouk, P., Neuville, D. & Benbakkar, M. (2011). Lithium isotope fractionation during magma degassing: Constraints from silicic differentiates and natural gas condensates from Piton de la Fournaise volcano (Réunion Island). *Chemical Geology* S0009254111000696. 10.1016/j.chemgeo.2011.02.002

Vlastélic, I., Menard, G., Gannoun, A., Piro, J.-L., Staudacher, T. & Famin, V. (2013). Magma degassing during the April 2007 collapse of Piton de la Fournaise: The record of semi-volatile trace elements (Li, B, Cu, In, Sn, Cd, Re, Tl, Bi). *Journal of Volcanology and Geothermal Research* **254**, 94–107. 10.1016/j.jvolgeores.2012.12.027

Wallace, P. J., Plank, T., Edmonds, M. & Hauri, E. (2015). Volatiles in magmas. *The Encyclopedia of Volcanoes*, 163–183. 10.1016/B978-0-12-385938-9.00007-9

Watkins, J. M., DePaolo, D. J., Huber, C. & Ryerson, F. J. (2009). Liquid composition-dependence of calcium isotope fractionation during diffusion in molten silicates. *Geochimica et Cosmochimica Acta* **73**, 7341–7359. 10.1016/j.gca.2009.09.004

Watkins, J. M., DePaolo, D. J. & Watson, E. B. (2017). Kinetic Fractionation of Non-Traditional Stable Isotopes by Diffusion and Crystal Growth Reactions. *Reviews in Mineralogy and Geochemistry* **82**, 85–125. 10.2138/rmg.2017.82.4

Watson, E. B. (1994). Chapter 10. Diffusion in Volatile-bearing magmas. *Volatiles in Magmas*. De Gruyter, 371–412. 10.1515/9781501509674-016

Watson, E. B. & Liang, Y. (1995). A simple model for sector zoning in slowly grown crystals: Implications for growth rate and lattice diffusion, with emphasis on accessory minerals in crustal rocks. *American Mineralogist*. De Gruyter **80**, 1179–1187. 10.2138/am-1995-11-1209

Watson, Bruce. E. & Müller, T. (2009). Non-equilibrium isotopic and elemental fractionation during diffusion-controlled crystal growth under static and dynamic conditions. *Chemical Geology* **267**, 111–124. 10.1016/j.chemgeo.2008.10.036

Watson, E. B. (2017). Diffusive fractionation of volatiles and their isotopes during bubble growth in magmas. *Contributions to Mineralogy and Petrology* **172**, 61. 10.1007/s00410-017-1384-7

Woodhead, J. D., Hellstrom, J., Hergt, J. M., Greig, A. & Maas, R. (2007). Isotopic and Elemental Imaging of Geological Materials by Laser Ablation Inductively Coupled Plasma-Mass Spectrometry. *Geostandards and Geoanalytical Research* **31**, 331–343. 10.1111/j.1751-908X.2007.00104.x

Yoshimura, S. (2015). Diffusive fractionation of H_2O and CO_2 during magma degassing. *Chemical Geology* **411**, 172–181. 10.1016/j.chemgeo.2015.07.003

Zhang, Y. (1999). H_2O in rhyolitic glasses and melts: Measurement, speciation, solubility, and diffusion. *Reviews of Geophysics* **37**, 493–516. 10.1029/1999RG900012

Zhang, Y. & Behrens, H. (2000). H_2O diffusion in rhyolitic melts and glasses. *Chemical Geology* **169**, 243–262. 10.1016/S0009-2541(99)00231-4

Zhang, Y. (2008). *Geochemical kinetics*. Princeton, N.J: Princeton University Press.

Zhang, Y., Ni, H. & Chen, Y. (2010). Diffusion Data in Silicate Melts. *Reviews in Mineralogy and Geochemistry* **72**, 311–408. 10.2138/rmg.2010.72.8

Appendix A1: Diffusion tables

Table A1.1: Electron microprobe results of major elements of the depleted end-members of the diffusion samples, and water values from the difference method and by Raman spectroscopy measurements. Numbers in brackets are the standard deviation errors.

Sample	**SiO_2 Wt%**	**Al_2O_3 Wt%**	**Na_2O Wt%**	**K_2O Wt%**	**CaO Wt%**	**MgO Wt%**	**MnO Wt%**	**FeO Wt%**	**H_2O** Wt%	**H2O Raman**
LPR50 DIFF1	74.4 (0.7)	13.1 (0.5)	4.03 (0.18)	3.81 (0.10)	0.35 (0.04)	0.03 (0.01)	0.01 (0.01)	0.07 (0.02)	4.09 (0.46)	4.00 (0.08)
LPR50 DIFF2	75.0 (0.5)	12.97 (0.20)	3.85 (0.08)	3.76 (0.04)	0.34 (0.02)	0.05 (0.01)	0.01 (0.01)	0.04 (0.03)	3.97 (0.25)	4.23 (0.21)
LPR50 DIFF3	(0.4) 74.6	13.2 (0.3)	3.93 (0.13)	3.79 (0.06)	0.36 (0.02)	0.03 (0.01)	0.01 (0.01)	0.05 (0.03)	4.02 (0.28)	4.10 (0.09)
LPR50 DIFF5	75.2 (0.4)	12.8 (0.2)	3.89 (0.14)	3.75 (0.06)	0.32 (0.01)	0.04 (0.01)	0.01 (0.02)	0.04 (0.01)	3.89 (0.49)	4.23 (0.21)
LPR50 DIFF6	74.9 (0.1)	12.9 (0.1)	3.88 (0.06)	3.76 (0.03)	0.34 (0.01)	0.05 (0.01)	0.01 (0.01)	0.10 (0.03)	3.97 (0.16)	4.11 (0.02)
LPR50 DIFF7	75.2 (0.2)	13.0 (0.2)	3.91 (0.07)	3.39 (0.05)	0.33 (0.02)	0.04 (0.01)	0.01 (0.01)	0.13 (0.02)	3.99 (0.28)	4.11 (0.02)
LPR50 DIFF8	75.0 (0.2)	12.9 (0.1)	3.83 (0.12)	3.74 (0.04)	0.34 (0.01)	0.04 (0.01)	0.01 (0.01)	0.07 (0.03)	4.03 (0.14)	4.11 (0.02)
LPR50 DIFF10	74.4 (0.4)	12.9 (0.3)	4.29 (0.23)	3.71 (0.07)	0.39 (0.02)	0.04 (0.01)	0.01 (0.01)	0.08 (0.02)	4.16 (0.18)	3.86 (0.08)
LPR50 DIFF12	74.7 (0.3)	12.8 (0.2)	3.89 (0.12)	3.78 (0.09)	0.38 (0.02)	0.04 (0.01)	0.01 (0.01)	0.11 (0.03)	4.30 (0.23)	4.12 (0.14)
LPR50 DIFF13	74.5 (0.1)	12.8 (0.2)	4.04 (0.12)	3.73 (0.03)	0.37 (0.02)	0.03 (0.01)	0.01 (0.01)	0.12 (0.01)	4.38 (0.07)	3.86 (0.08)
LPR50 STD	74.5 (0.2)	12.7 (0.1)	3.92 (0.06)	3.75 (0.04)	0.37 (0.02)	0.04 (0.01)	0.01 (0.01)	0.11 (0.02)	4.56 (0.19)	

Table A1.2: Electron microprobe results of major elements of the depleted end-members of the diffusion samples, and water values from the difference method and by Raman spectroscopy measurements. Numbers in brackets are the standard deviation errors.

Sample	**SiO_2 Wt%**	**Al_2O_3 Wt%**	**Na_2O Wt%**	**K_2O Wt%**	**CaO Wt%**	**MgO Wt%**	**MnO Wt%**	**FeO Wt%**	**H_2O** Wt%	**H2O Raman**
LPR200	74.4	13.1	3.96	3.78	0.35	0.04	0.01	0.05	4.33	4.03
DIFF1	(0.5)	(0.2)	(0.09)	(0.03)	(0.02)	(0.01)	(0.01)	(0.03)	(0.47)	(0.10)
LPR200	74.8	13.0	3.96	3.79	0.34	0.04	0.00	0.07	3.98	3.91
DIFF2	(0.3)	(0.2)	(0.10)	(0.03)	(0.01)	(0.01)	(0.00)	(0.02)	(0.30)	(0.12)
LPR200	74.5	13.1	3.96	3.77	0.35	0.04	0.01	0.07	4.21	4.01
DIFF3	(0.6)	(0.1)	(0.17)	(0.05)	(0.02)	(0.02)	(0.01)	(0.03)	(0.36)	(0.07)
LPR200	74.8	13.0	3.95	3.78	0.35	0.04	0.01	0.08	3.96	3.97
DIFF5	(0.3)	(0.1)	(0.13)	(0.02)	(0.01)	(0.01)	(0.01)	(0.02)	(0.26)	(0.05)
LPR200	74.8	13.1	4.01	3.79	0.35	0.03	0.01	0.05	3.82	4.08
DIFF6	(0.3)	(0.2)	(0.13)	(0.04)	(0.01)	(0.01)	(0.01)	(0.03)	(0.15)	(0.12)
LPR200	75.0	12.9	3.91	3.80	0.34	0.04	0.01	0.02	3.97	4.08
DIFF7	(0.2)	(0.1)	(0.10)	(0.05)	(0.01)	(0.01)	(0.01)	(0.02)	(0.14)	(0.12)
LPR200	74.6	13.0	4.01	3.78	0.34	0.04	0.01	0.05	4.04	4.08
DIFF8	(0.2)	(0.1)	(0.09)	(0.02)	(0.01)	(0.01)	(0.02)	(0.02)	(0.21)	(0.12)
LPR200	74.5	12.8	3.98	3.76	0.41	0.04	0.01	0.12	4.42	4.06
DIFF10	(0.3)	(0.2)	(0.11)	(0.11)	(0.03)	(0.01)	(0.01)	(0.02)	(0.19)	(0.17)
LPR200 DIFF12	74.6	12.9	3.92	3.75	0.35	0.03	0.01	0.11	4.25	4.06
pre exp	(0.3)	(0.2)	(0.12)	(0.04)	(0.01)	(0.01)	(0.01)	(0.02)	(0.41)	(0.17)
LPR200	74.5	12.8	3.97	3.81	0.38	0.04	0.01	0.07	4.38	
DIFF12	(0.3)	(0.3)	(0.09)	(0.11)	(0.01)	(0.01)	(0.01)	(0.03)	(0.17)	
LPR200	74.7	12.7	3.87	3.81	0.39	0.05	0.01	0.06	4.36	4.06
DIFF13	(0.49	(0.1)	(0.10)	(0.11)	(0.02)	(0.01)	(0.02)	(0.02)	(0.24)	(0.17)
LPR200	74.4	12.8	3.89	3.81	0.40	0.05	0.01	0.09	4.58	
STD	(0.4)	(0.2)	(0.11)	(0.06)	(0.03)	(0.01)	(0.01)	(0.02)	(0.18)	

Table A1.3: SIMS results of lithium for the experiment DIFF1, in multi and monocollection mode

DIFF1 - 700 °C - 0 seconds (multic)					DIFF1 - 700 °C - 0 seconds (monoc)		
Dist [mm]	δ^{7}Li	δ^{7}Li err	Li [µg/g]	Li err [µg/g]	Dist [mm]	δ^{7}Li	δ^{7}Li err
-4.6	-2.4	1.2	207.0	22.4	-1.49	-1.33	0.38
-3.9	-0.6	0.9	211.1	22.6	-0.99	-0.72	0.37
-3.0	0.0	1.2	207.8	24.5	-0.57	-2.37	0.40
-2.9	-2.4	1.4	202.6	6.5	-0.51	-1.28	0.40
-2.6	-1.7	1.0	207.6	7.0	-0.46	-0.34	0.40
-2.0	-1.9	1.0	211.9	26.6	-0.41	0.16	0.40
-2.0	-3.5	1.1	204.3	6.1	-0.36	0.58	0.40
-1.7	-2.2	1.0	206.5	6.1	-0.31	-0.02	0.40
-1.4	-3.7	0.9	205.8	8.7	-0.26	2.13	0.41
-1.2	2.6	1.1	209.3	16.4	-0.21	2.02	0.41
-1.1	-2.1	1.2	212.1	19.2	-0.16	3.60	0.42
-1.1	-0.4	1.3	202.8	6.0	-0.11	2.23	0.44
-1.0	0.9	1.3	204.0	12.7	-0.05	0.36	0.45
-0.8	-1.4	0.9	203.6	11.9	0.01	-4.00	0.52
-0.6	1.3	1.2	205.5	12.1	0.06	-4.29	0.56
-0.4	-3.2	1.3	205.2	12.6	0.12	-5.24	0.60
-0.2	4.0	1.3	197.0	13.6	0.16	-5.93	0.65
-0.2	2.1	1.3	183.7	15.4	0.22	-5.67	0.70
-0.1	2.7	1.7	170.9	5.2	0.26	-2.41	0.78
0.0	2.0	1.1	151.7	10.7	0.31	-1.70	0.80
0.0	-1.8	1.5	123.4	7.9	0.36	-0.48	0.81
0.1	-6.6	1.5	96.7	9.3	0.41	-0.36	0.81
0.3	-5.2	1.8	64.5	4.7	0.46	-1.83	0.81
0.5	3.2	2.0	61.6	3.6	0.51	0.20	0.82
0.7	1.5	2.5	58.8	22.6	1.01	0.40	0.74
0.9	-2.3	1.8	55.5	3.6	1.51	0.40	0.70
0.9	1.5	1.7	55.1	1.8			
1.1	-1.1	1.8	53.6	3.6			
1.3	-2.0	1.9	54.9	3.4			
1.5	0.5	2.4	55.4	3.5			
1.7	1.6	2.1	52.8	2.3			
1.9	-1.7	2.0	51.7	2.3			
1.9	1.6	2.1	51.2	3.1			
2.2	-1.1	2.0	48.3	1.6			
2.5	1.9	1.8	49.6	1.7			
2.6	0.5	2.3	49.9	2.5			
2.8	-0.1	2.0	53.0	1.7			
3.0	0.3	1.6	57.7	1.9			
3.4	2.0	1.9	57.5	2.9			
3.6	2.5	1.6	57.0	1.8			
3.7	3.4	2.4	56.4	4.7			
4.6	2.0	2.2	52.2	2.7			

Table A1.4: Lithium measurements in Multi- and Mono-collection mode at the SIMS, of DIFF2

DIFF2 - 700 °C - 30 minutes (multicoll)					DIFF2 - 700 °C - 30 minutes (monocoll)		
Dist [mm]	δ^7Li	δ^7Li err	Li [µg/g]	Li err [µg/g]	Dist [mm]	Li [µg/g]	Li err [µg/g]
-5.0	-0.9	1.1	206.9	20.5	2.00	1.23	0.83
-3.5	0.4	1.1	194.8	20.2	1.50	-1.94	0.81
-3.2	-0.1	1.1	192.3	7.6	1.13	-4.05	0.79
-3.0	-1.3	1.0	194.5	7.3	1.00	-4.29	0.76
-2.9	-3.5	1.1	195.8	6.2	0.88	-4.39	0.75
-2.6	-1.1	1.3	197.7	6.8	0.74	-3.78	0.73
-2.3	-2.6	1.4	196.4	7.5	0.61	-3.44	0.72
-2.0	-1.0	1.1	204.2	20.1	0.48	-5.64	0.69
-1.7	-2.8	1.2	199.7	7.4	0.36	-0.93	0.66
-1.5	-3.1	1.1	202.1	6.3	0.23	-0.37	0.63
-1.4	-1.9	1.5	198.4	6.9	0.11	-2.64	0.59
-1.4	0.8	1.0	200.1	19.0	-0.04	1.68	0.57
-1.2	1.1	1.7	190.2	15.4	-0.15	4.45	0.54
-0.9	2.0	1.4	181.9	13.5	-0.27	2.93	0.53
-0.8	5.8	1.2	173.6	12.0	-0.40	3.36	0.51
-0.5	2.9	1.0	163.5	12.4	-0.53	3.57	0.50
-0.3	2.6	1.4	166.9	16.7	-0.65	0.82	0.51
-0.2	2.7	1.3	149.9	11.8	-0.78	0.20	0.51
-0.1	1.9	1.6	141.2	10.9	-0.90	-0.28	0.51
0.0	2.1	1.2	140.8	18.2	-1.03	-2.99	0.51
0.0	3.0	1.4	111.8	10.5	-1.16	-1.56	0.51
0.1	0.4	1.1	112.0	14.3	-1.28	-1.53	0.51
0.2	0.5	1.5	100.9	9.5	-1.41	-1.21	0.51
0.3	-2.4	1.2	94.7	3.8	-1.54	-2.79	0.50
0.4	-3.8	1.4	84.6	7.4	-2.01	-1.62	0.44
0.5	-4.2	1.7	70.4	6.4	-2.52	-1.13	0.44
0.7	-3.7	1.6	60.2	4.6			
0.9	3.1	1.7	54.2	3.2			
1.1	4.2	1.8	53.8	4.0			
1.2	-1.7	1.9	51.9	3.4			
1.3	-3.4	1.8	55.3	2.2			
1.6	-0.2	1.7	52.4	4.4			
1.9	0.9	1.6	55.6	2.4			
1.9	-0.3	1.7	55.8	1.8			
2.2	-0.7	2.1	53.7	1.7			
2.5	1.6	1.6	53.3	1.7			
2.8	0.0	1.6	55.0	1.7			
3.1	0.2	2.0	55.4	4.5			
3.4	-2.4	1.7	55.1	1.7			
3.4	-0.8	2.0	53.9	1.7			
5.0	2.3	1.7	54.6	4.9			

Table A1.5: SIMS Li profiles for samples DIFF3 and DIFF5

DIFF3 - 800 °C - 30 minutes					DIFF5 - 1000 °C - 0 seconds				
Dist [mm]	δ^7Li	δ^7Li err	Li [µg/g]	Li err [µg/g]	Dist [mm]	δ^7Li	δ^7Li err	Li [µg/g]	Li err [µg/g]
-4.7	-0.2	1.2	200.4	16.0	-2.7	-3.4	1.4	194.5	6.6
-3.6	-1.3	0.9	194.5	6.0	-2.7	0.8	1.3	197.7	14.3
-2.6	0.8	1.0	199.5	8.2	-2.4	1.5	1.6	201.1	7.1
-2.4	-1.9	1.2	187.4	6.1	-2.1	1.8	1.0	199.0	6.5
-2.3	-0.8	1.2	193.0	6.1	-1.8	-0.6	1.6	198.9	6.4
-2.1	2.4	1.4	196.0	14.5	-1.5	-0.7	1.0	199.2	18.7
-1.8	1.0	0.9	195.6	8.0	-1.5	0.6	1.2	198.6	6.2
-1.6	-0.4	1.4	183.2	5.8	-1.2	0.6	1.3	194.2	7.5
-1.5	6.4	1.5	170.6	8.0	-1.0	2.2	1.1	182.6	6.8
-1.3	1.3	1.2	171.2	5.4	-0.8	2.1	1.2	177.8	6.7
-1.1	0.0	1.0	168.7	14.0	-0.7	6.5	1.2	171.3	8.4
-1.0	3.3	1.5	160.7	6.5	-0.5	2.7	1.4	160.6	5.9
-0.9	3.2	1.7	156.9	9.7	-0.3	3.1	1.9	144.0	8.9
-0.7	1.6	1.6	150.3	6.4	-0.2	0.1	1.1	145.5	5.5
-0.5	-0.6	1.4	155.6	4.9	-0.1	2.9	2.3	127.1	7.3
-0.5	3.3	1.4	140.5	6.1	0.0	3.1	1.2	119.1	17.1
-0.5	2.5	1.5	131.6	7.6	0.1	-1.7	1.3	102.6	9.7
-0.3	0.7	1.2	138.2	11.3	0.1	0.7	1.8	95.2	5.6
-0.1	-1.5	1.3	125.2	7.6	0.3	0.6	1.9	79.9	6.3
-0.1	0.4	1.4	122.0	14.1	0.5	-5.6	2.0	70.4	5.2
0.1	-1.7	2.1	105.0	7.1	0.7	-8.3	2.1	63.6	2.8
0.1	-2.1	1.6	99.6	6.2	0.8	-6.9	2.3	63.9	2.3
0.3	-1.6	1.9	94.5	5.6	0.8	-10.8	1.9	65.2	5.9
0.5	-2.8	1.7	99.9	3.5	0.9	-5.7	2.2	58.4	3.7
0.6	-4.0	1.9	86.8	7.1	1.1	-3.5	2.1	57.4	2.0
0.8	-3.6	2.2	82.0	4.6	1.1	-0.3	2.6	53.5	2.5
1.0	-6.8	1.3	83.7	3.4	1.4	0.9	2.6	53.0	1.9
1.0	-3.4	1.9	77.1	5.1	1.7	-3.3	2.0	52.5	1.8
1.1	-4.4	1.6	75.8	3.0	2.0	-2.2	1.7	55.8	2.6
1.2	-5.7	1.6	70.8	5.3	2.3	-0.6	1.7	55.1	1.9
1.4	-10.2	1.5	68.8	2.2	2.3	4.4	1.6	55.8	5.7
1.7	-7.3	1.5	65.5	2.9	2.5	-2.6	1.8	53.2	2.0
1.9	-4.0	2.0	59.4	2.9	2.9	-0.5	2.2	51.1	1.7
2.0	-5.0	1.7	55.8	2.5	3.2	0.7	1.8	50.1	1.8
2.3	-4.4	1.7	54.8	4.0	3.5	-3.7	1.8	51.5	2.0
2.6	-2.4	2.0	53.3	4.2	3.8	-4.1	1.8	52.6	2.0
2.9	5.6	2.1	51.5	4.9	3.8	2.3	2.0	53.4	3.7
2.9	2.9	2.1	47.5	4.2	4.1	-0.8	1.9	50.9	1.7
					4.3	0.6	2.1	50.4	1.9
					4.4	3.5	1.8	50.8	1.7
					4.7	0.0	2.4	52.2	2.1
					5.0	0.5	1.9	53.7	2.2
					2.3	-0.1	2.3	52.3	2.6
					5.3	0.0	1.8	50.5	2.5

Table A1.6: SIMS measurements of the experiments DIFF10 and DIFF13 for lithium.

DIFF10 - 1200 °C - 0 seconds					DIFF13 - 1050 °C - 15 minutes				
Dist [mm]	δ^7Li	δ^7Li err	Li [µg/g]	Li err [µg/g]	Dist [mm]	δ^7Li	δ^7Li err	Li [µg/g]	Li err [µg/g]
-2.9	0.6	1.0	184.8	15.1	-3.4	4.7	1.3	145.3	11.1
-2.8	0.8	0.9	201.4	13.5	-3.3	4.0	2.2	168.3	13.8
-2.7	-0.9	1.0	205.9	14.7	-3.2	3.6	1.7	180.9	16.0
-2.6	3.3	1.6	207.4	11.9	-3.1	1.8	1.2	186.6	13.9
-2.5	-0.2	1.0	206.1	7.3	-3.0	3.5	1.9	189.6	10.9
-2.4	-1.4	0.9	206.9	6.8	-2.9	1.7	0.7	192.0	11.3
-2.3	-0.6	0.6	207.5	10.6	-2.8	2.8	1.4	193.4	18.0
-2.2	-0.6	1.1	206.7	8.2	-2.7	0.0	1.7	189.7	12.2
-2.1	-0.3	0.6	205.6	7.5	-2.6	9.6	3.0	189.6	36.0
-2.0	-1.4	0.5	203.2	10.8	-2.5	5.3	1.4	191.8	30.0
-1.9	-1.1	0.6	201.7	8.3	-2.4	4.7	1.2	188.0	21.3
-1.8	0.2	0.7	198.7	8.4	-2.3	4.1	1.4	187.3	17.4
-1.7	1.0	0.9	195.4	6.8	-2.2	7.0	1.7	186.4	22.4
-1.6	-0.2	0.9	191.8	7.9	-2.1	3.6	1.6	184.5	26.9
-1.5	0.0	1.1	187.2	7.9	-2.0	2.5	0.9	181.3	18.6
-1.4	-1.5	0.6	184.2	8.4	-1.9	4.3	1.2	179.8	21.8
-1.3	0.3	0.7	180.8	7.2	-1.8	3.3	1.4	177.5	26.6
-1.2	0.5	0.8	178.4	6.0	-1.7	3.3	1.3	175.0	23.2
-1.1	0.3	0.5	174.6	7.2	-1.6	3.6	1.1	174.0	24.8
-1.0	0.6	1.1	171.5	7.4	-1.5	4.3	1.2	170.9	20.4
-0.9	0.2	0.9	167.0	6.3	-1.4	5.6	1.2	169.3	25.3
-0.8	2.2	0.9	163.4	5.0	-1.3	3.9	1.0	166.9	27.3
-0.7	-0.4	0.8	158.7	5.3	-1.2	1.5	1.7	164.5	23.3
-0.6	0.8	1.3	153.1	6.8	-1.1	3.5	1.4	164.2	22.1
-0.5	0.7	0.9	148.1	6.0	-1.0	3.3	1.0	161.9	26.1
-0.4	0.2	0.8	144.1	7.6	-0.9	4.9	0.9	160.9	22.7
-0.3	-0.3	1.0	139.5	5.1	-0.8	4.5	1.0	160.2	22.0
-0.2	-2.6	1.3	135.6	7.1	-0.7	2.9	1.1	155.6	15.4
-0.1	-3.2	1.2	127.8	6.0	-0.6	3.7	1.2	154.1	16.7
0.1	-1.7	0.9	121.9	7.1	-0.5	4.4	1.0	151.5	19.9
0.2	-1.6	1.0	117.5	6.2	-0.4	1.7	0.6	144.8	17.5
0.3	-2.4	1.2	113.9	5.6	-0.3	1.3	1.2	139.7	12.1
0.4	-5.3	0.8	108.5	5.2	-0.2	0.4	1.1	136.3	15.4
0.5	-3.3	1.1	106.1	5.7	-0.1	-2.6	1.1	131.4	16.9
0.6	-5.5	1.2	102.7	5.6	0.1	1.3	1.5	129.2	18.7
0.7	-4.7	1.0	99.0	3.6	0.2	1.3	1.8	124.2	13.0
0.8	-7.0	1.4	99.1	7.2	0.3	1.3	1.0	117.9	10.6
0.9	-6.0	0.9	92.3	4.4	0.4	-0.5	0.9	112.9	9.2
1.0	-7.2	0.9	88.3	3.8	0.5	0.1	1.2	109.1	14.6
1.1	-6.0	1.1	85.9	5.4	0.6	-2.7	1.2	105.4	12.0
1.2	-8.2	1.1	83.3	5.4	0.7	-3.8	0.7	102.5	11.5
1.3	-6.1	1.2	80.2	4.1	0.8	-3.5	1.0	100.9	10.7
1.4	-6.1	1.2	77.8	5.3	0.9	-3.6	0.9	99.2	10.3
1.5	-3.8	0.9	75.1	4.4	1.0	-3.0	1.1	97.9	11.6
1.6	-10.4	1.1	72.6	3.6	1.1	-5.5	1.3	94.7	6.6

Table A1.6 continuation

DIFF10 - 1200 °C - 0 seconds					DIFF13 - 1050 °C - 15 minutes				
Dist [mm]	δ^7Li	δ^7Li err	Li [µg/g]	Li err [µg/g]	Dist [mm]	δ^7Li	δ^7Li err	Li [µg/g]	Li err [µg/g]
1.7	-7.6	0.9	70.5	4.0	1.2	-4.8	1.2	92.9	10.6
1.8	-6.1	1.4	68.6	3.5	1.3	-4.9	1.1	91.3	12.9
1.9	-7.8	1.2	67.0	3.0	1.4	-6.3	2.0	89.0	7.0
2.0	-4.7	1.5	65.6	3.8	1.5	-4.2	0.9	86.8	7.8
2.1	-7.4	0.9	64.6	4.2	1.6	-6.9	1.3	84.7	7.0
2.2	-7.6	0.8	63.4	3.9	1.7	-8.6	1.2	83.0	6.3
2.3	-7.1	1.0	62.8	3.7	1.8	-7.3	1.1	81.5	7.8
2.4	-6.3	1.4	61.9	4.7	1.9	-7.5	1.3	79.8	8.1
2.5	-4.9	0.8	61.5	3.5	2.0	-10.6	1.1	77.8	6.4
2.6	-6.4	1.2	60.9	3.5	2.1	-8.5	1.2	77.2	5.0
2.7	-4.6	1.3	60.5	3.4	2.2	-7.6	1.2	76.2	4.7
2.8	-3.3	0.8	60.2	3.1	2.3	-11.2	0.9	74.5	4.7
2.9	-3.8	0.9	60.0	2.9	2.4	-9.7	0.9	74.2	4.7
3.0	-0.9	1.1	59.4	2.9	2.5	-10.2	1.2	73.6	3.6
3.1	-2.3	0.9	58.9	3.9	2.6	-6.8	0.9	72.9	6.4
3.2	0.4	1.1	58.7	3.7	2.7	-10.6	0.8	72.2	4.5
3.3	-2.0	1.1	58.0	3.3	2.8	-10.2	1.4	71.2	3.9
3.4	-1.8	1.3	57.8	3.8	2.9	-11.1	0.9	70.1	3.6
3.5	-1.3	1.0	57.0	2.7	3.0	-11.2	1.3	69.8	3.5
3.6	-0.1	1.1	56.9	3.4	3.1	-11.4	1.3	69.4	4.1
3.7	1.0	0.9	56.6	4.4					
3.8	0.2	1.2	55.6	3.7					
3.9	0.1	0.9	54.6	4.6					
4.0	-0.8	1.2	52.1	3.9					
4.1	3.1	1.1	46.6	3.1					

Table A1.7: Boron concentration and δ^{11}B for experiments DIFF5 and DIFF6

DIFF5 - 1000 °C - 0 seconds (SIMS)					DIFF6 - 1000 °C - 24 hours (SIMS)				
Dist [mm]	δ^{11}B	δ^{11}B err	B [µg/g]	B err [µg/g]	Dist [mm]	δ^{11}B	δ^{11}B err	B [µg/g]	B err [µg/g]
-2.70	0.37	0.40	675.87	181.03	-0.63	0.01	0.51	641.74	20.16
-1.54	2.46	0.43	678.42	191.67	-0.59	0.47	0.48	637.77	18.84
-1.07	-2.77	0.39	618.89	80.26	-0.55	0.33	0.48	635.81	12.35
-0.87	-2.59	0.42	611.49	78.11	-0.51	-0.17	0.50	637.75	17.94
-0.67	-2.12	0.41	612.25	87.11	-0.47	0.01	0.71	633.01	11.75
-0.47	1.34	0.40	619.93	85.61	-0.43	-1.06	0.57	631.46	16.24
-0.28	0.18	0.64	617.70	57.48	-0.39	0.58	0.48	630.24	17.52
-0.06	0.10	0.46	624.11	56.93	-0.35	-0.04	0.57	627.58	19.43
0.04	8.14	1.08	155.30	44.49	-0.30	0.11	0.45	627.09	18.43
0.08	-1.34	0.55	154.92	50.11	-0.26	0.12	0.67	627.43	17.92
0.10	-0.53	0.82	141.13	15.16	-0.22	-0.09	0.46	626.18	19.33
0.30	2.07	1.16	148.19	19.24	-0.18	-0.17	0.62	624.94	18.09
0.50	0.66	0.72	168.82	17.50	-0.15	0.84	0.54	624.46	16.50
0.71	0.90	0.70	180.49	22.74	-0.11	-0.14	0.63	605.79	25.77
0.76	-0.69	0.53	179.93	56.79	-0.06	0.10	0.45	561.91	13.95
0.90	3.66	0.94	170.82	20.50	-0.02	1.14	0.50	468.56	14.13
1.10	1.89	0.81	154.11	18.54	0.02	0.87	0.61	359.60	12.18
2.27	2.19	0.51	188.86	60.97	0.06	-1.12	0.66	256.96	9.33
3.79	-2.72	0.59	158.19	39.39	0.10	-0.64	0.75	200.64	6.83
5.32	-2.56	0.73	134.48	30.86	0.14	-1.50	0.79	179.64	5.83
					0.19	1.15	1.00	174.22	5.50
					0.23	-0.72	0.97	172.78	3.88
					0.27	-0.20	0.86	172.40	5.14
					0.31	-0.67	0.81	171.80	4.24
					0.35	1.10	0.81	171.23	4.31
					0.40	-0.08	0.92	171.14	6.13
					0.43	-3.44	0.82	170.60	5.92
					0.48	-1.22	0.81	170.33	4.12
					0.52	-1.65	1.10	170.06	4.09
					0.56	-0.86	0.95	170.19	5.31
					0.61	0.11	0.85	170.69	6.61
					0.65	-0.50	0.81	170.11	5.32
					0.69	-1.44	1.10	170.25	5.68
					0.73	-1.90	0.94	170.39	5.35
					0.77	-1.98	0.81	170.32	4.73
					0.81	-0.75	0.94	170.82	5.10
					0.85	-0.93	0.81	170.46	6.01
					0.89	-1.40	0.81	170.77	4.45
					0.93	-0.02	0.92	170.62	6.79
					0.98	-1.41	0.81	171.17	5.65

Table A1.8: Boron concentration and isotopes for experiments DIFF7 and DIFF8

DIFF7 - 1100 °C - 20 hours (SIMS)					DIFF8 - 1200 °C - 20 hours (SIMS)				
Dist [mm]	$\delta^{11}B$	$\delta^{11}B$ err	B [µg/g]	B err [µg/g]	Dist [mm]	$\delta^{11}B$	$\delta^{11}B$ err	B [µg/g]	B err [µg/g]
-0.62	0.69	1.46	608.43	17.35	-0.66	-1.60	1.40	631.05	32.45
-0.58	0.54	0.99	606.99	14.94	-0.62	0.74	1.03	627.26	27.94
-0.54	2.46	1.00	609.31	17.49	-0.58	1.76	0.97	631.01	20.41
-0.50	-0.17	0.99	613.06	17.90	-0.54	-0.71	1.03	630.32	21.48
-0.45	-0.09	1.25	613.99	15.47	-0.50	0.79	0.76	628.56	13.26
-0.42	0.98	1.01	617.40	16.49	-0.46	-0.33	0.80	630.57	16.17
-0.38	0.38	1.41	617.94	18.49	-0.42	-0.83	0.77	632.60	16.05
-0.34	-1.40	1.20	622.44	17.63	-0.38	-1.24	0.68	626.89	16.57
-0.29	-0.10	1.04	623.44	16.02	-0.34	-1.13	0.74	626.14	19.54
-0.26	0.14	1.02	623.14	17.62	-0.30	-0.51	0.50	620.15	13.13
-0.21	5.76	2.15	621.11	17.91	-0.26	-0.06	1.12	609.08	16.01
-0.18	-1.66	1.04	614.49	20.79	-0.22	-2.61	1.27	595.77	23.20
-0.14	0.35	0.89	596.16	17.62	-0.18	-0.15	0.86	576.31	13.99
-0.10	-1.75	0.89	566.43	20.02	-0.14	0.65	0.65	547.01	15.86
-0.06	-1.10	0.87	517.47	18.74	-0.10	1.17	1.52	507.07	18.16
-0.02	-1.56	0.87	452.36	12.56	-0.06	-0.82	0.74	462.19	12.95
0.02	0.73	0.94	390.95	11.62	-0.02	-0.92	0.68	414.14	11.16
0.06	-0.38	0.90	318.32	11.49	0.02	-2.03	1.16	373.72	10.04
0.10	-0.36	1.13	259.51	7.99	0.06	-0.38	0.89	324.39	10.16
0.14	-2.07	0.97	219.91	8.12	0.10	-2.25	0.90	280.54	9.00
0.19	-0.03	0.85	195.49	4.55	0.14	1.28	0.82	244.38	8.08
0.22	-0.16	0.82	183.93	6.67	0.17	-1.87	1.88	218.04	7.38
0.26	-0.70	0.74	179.33	5.71	0.22	-1.89	1.29	199.48	6.94
0.30	-1.43	0.64	177.53	6.45	0.25	-3.34	1.12	186.53	7.52
0.34	0.04	0.58	176.86	5.66	0.30	-1.95	0.75	178.07	5.62
0.38	-0.16	0.62	176.27	5.66	0.34	-2.07	0.87	175.39	6.20
0.42	-0.69	0.48	175.52	4.28	0.38	-0.14	0.86	173.09	5.40
0.47	-2.36	0.72	175.41	6.24	0.42	-1.80	0.77	172.25	6.49
0.50	-0.51	0.44	175.51	6.40	0.46	-1.23	0.77	172.27	5.58
0.54	-1.82	0.45	174.59	6.21	0.50	-1.18	0.77	172.89	4.98
0.58	-0.55	0.43	174.48	6.68	0.54	-1.40	0.82	173.17	7.58
0.63	-0.99	0.48	174.34	6.85	0.58	-1.41	0.88	173.78	7.03
0.66	-0.40	0.52	173.13	5.50	0.62	-0.81	0.89	173.97	5.91
0.71	0.10	0.51	173.21	6.18	0.66	-2.04	0.75	174.96	5.89
0.74	-0.60	0.43	173.15	7.91	0.70	-2.08	0.75	175.46	6.66
0.79	0.25	0.46	173.43	6.33	0.74	-3.43	0.77	176.35	6.73
0.82	-0.66	0.43	173.82	5.99	0.78	-0.67	0.75	177.18	6.12
0.86	0.45	0.43	172.17	6.23	0.82	-1.89	0.90	177.63	6.27
0.90	-1.74	0.52	172.34	5.11	0.86	-0.92	0.93	177.70	6.54
0.94	-0.84	0.43	172.69	6.15	0.89	-1.13	0.74	177.87	7.35
0.98	-0.64	0.42	172.36	10.95	0.94	-0.71	0.74	179.24	5.92

Table A1.9: Boron concentration and isotopes results for DIFF10 and DIFF12

DIFF10 - 1200 °C - 0 seconds (LA-ICP-MS)			DIFF12 - 1250 °C - 20 hours (SIMS)				
Dist [mm]	B [mg/g]	B err [mg/g]	Dist [mm]	$\delta^{11}B$	$\delta^{11}B$ err	B [mg/g]	B err [mg/g]
4.05	137.73	11.59	-1.02	-0.34	0.46	595.08	19.88
3.9	160.05	14.39	-0.98	-0.86	0.58	597.18	18.86
3.75	149.22	16.87	-0.93	0.05	0.54	596.57	21.16
3.6	152.53	15.94	-0.90	0.34	0.49	596.20	17.52
3.45	145.43	14.55	-0.86	-0.60	0.54	596.43	19.91
3.3	156.84	17.19	-0.82	-0.39	0.53	597.38	18.04
3.15	161.26	14.61	-0.78	-0.46	0.70	598.95	20.43
3	162.11	18.50	-0.74	-1.73	0.46	599.25	22.10
2.85	159.11	16.17	-0.70	-0.31	0.58	597.49	16.90
2.7	163.27	16.25	-0.66	-0.36	0.70	598.75	19.23
2.55	158.55	14.92	-0.62	-0.60	0.46	600.98	19.80
2.4	161.91	13.89	-0.58	-0.85	0.59	598.99	18.60
2.25	144.19	13.69	-0.54	-0.50	0.51	601.33	19.39
2.1	143.10	15.56	-0.50	-0.36	0.65	599.63	19.64
1.95	142.13	18.12	-0.46	-0.53	0.67	600.79	21.36
1.8	148.16	15.28	-0.42	0.29	0.46	598.31	25.22
1.65	146.67	16.18	-0.38	-0.15	0.58	598.18	21.05
1.5	149.86	18.30	-0.34	-0.94	0.52	592.38	25.06
1.35	171.99	20.61	-0.31	-1.03	0.60	587.99	16.53
1.2	147.38	14.35	-0.27	0.12	0.45	578.82	14.39
1.05	151.93	17.04	-0.22	-0.57	0.48	562.07	17.29
0.9	132.69	22.31	-0.18	1.00	0.47	548.14	14.64
0.75	171.00	20.36	-0.14	0.21	0.51	526.20	16.14
0.6	134.41	16.17	-0.10	-0.45	0.50	500.98	16.54
0.45	176.82	24.49	-0.06	0.12	0.72	470.47	12.70
0.3	171.69	24.89	-0.02	-0.70	0.58	438.65	14.60
0.15	175.60	26.38	0.02	-0.53	0.68	405.03	13.63
0	620.32	78.31	0.06	0.62	0.70	380.94	11.23
-0.15	649.16	105.59	0.10	-0.55	0.61	345.23	11.88
-0.3	553.57	71.86	0.14	-1.46	0.64	311.16	11.99
-0.45	601.28	96.97	0.18	-1.55	0.93	280.97	8.25
-0.6	593.28	85.43	0.22	-0.84	0.77	255.06	9.63
-0.75	721.17	134.08	0.26	-1.60	0.74	232.85	7.05
-0.9	727.56	109.47	0.30	-1.93	0.84	215.12	9.61
-1.05	541.01	83.32	0.34	-2.77	0.80	201.26	8.00
-1.2	718.31	127.99	0.38	-1.14	0.82	191.05	6.14
-1.35	775.83	139.16	0.42	-1.42	0.84	184.01	6.40
-1.5	627.89	98.52	0.46	-1.88	1.21	178.98	7.45
-1.65	639.41	89.69	0.50	-3.28	0.87	176.61	7.79
-1.8	771.77	143.25	0.54	-1.00	0.94	174.00	5.25
-1.95	656.02	114.01	0.58	-1.74	0.76	173.05	6.23
-2.1	799.3981	150.4463					

Table A1.10: LA ICP-MS lithium results for DIFF1 – DIFF2 – DIFF3 – DIFF5 – DIFF6

DIFF1 - 700 °C 0 s		DIFF2 - 700 °C 30 min		DIFF3 - 800 °C 30 min		DIFF5 - 1000 °C 0 s		DIFF6 - 1000 °C 24 hrs	
Dist [µm]	Li [µg/g] (err)	Dist [µm]	Li [µg/g] (err)	Dist [µm]	Li [µg/g] (err)	Dist [µm]	Li [µg/g] (err)	Dist [µm]	Li [µg/g] (err)
-280	321 (95)	-300	205 (22)	-370	165 (25)	400	57 (7)	-800	142 (1)
-260	263 (38)	-280	190 (20)	-350	185 (33)	380	67 (8)	-785	143 (1)
-240	275 (48)	-260	193 (18)	-330	169 (26)	360	61 (8)	-770	143 (1)
-220	267 (43)	-240	202 (22)	-310	155 (22)	340	56 (7)	-755	143 (1)
-200	276 (120)	-220	188 (19)	-290	159 (23)	320	66 (8)	-740	142 (1)
-180	234 (65)	-200	204 (23)	-270	195 (48)	300	72 (9)	-725	142 (1)
-160	244 (45)	-180	201 (20)	-250	162 (26)	280	64 (8)	-710	143 (1)
-140	251 (164)	-160	182 (19)	-230	172 (45)	260	83 (11)	-695	144 (1)
-120	243 (35)	-140	181 (19)	-210	148 (20)	240	88 (12)	-680	144 (1)
-100	259 (48)	-120	171 (21)	-190	155 (29)	220	79 (10)	-665	144 (1)
-80	257 (42)	-100	172 (17)	-170	142 (22)	200	87 (11)	-650	142 (1)
-60	146 (98)	-80	171 (19)	-150	168 (52)	180	92 (13)	-635	144 (1)
-40	240 (53)	-60	187 (21)	-130	137 (25)	160	88 (12)	-620	143 (1)
-20	256 (77)	-40	152 (18)	-110	151 (47)	140	106 (15)	-605	144 (1)
0	187 (26)	-20	137 (91)	-90	133 (30)	120	106 (16)	-590	145 (1)
20	128 (15)	0	113 (15)	-70	171 (35)	100	134 (16)	-575	145 (1)
40	133 (20)	20	100 (13)	-50	198 (46)	80	121 (11)	-560	145 (1)
60	126 (17)	40	117 (13)	-30	147 (31)	60	94 (11)	-545	145 (1)
80	124 (22)	60	127 (16)	-10	184 (38)	40	106 (13)	-530	145 (1)
100	133 (26)	80	98 (9)	10	159 (31)	20	117 (49)	-515	145 (1)
120	96 (15)	100	109 (12)	30	133 (17)	0	125 (14)	-500	145 (1)
140	124 (32)	120	122 (15)	50	161 (26)	-20	137 (14)	-485	147 (1)
160	133 (29)	140	101 (13)	70	145 (28)	-40	133 (16)	-470	145 (1)
180	110 (23)	160	116 (14)	90	164 (33)	-60	147 (24)	-455	144 (1)
200	85 (17)	180	118 (16)	110	131 (18)	-80	136 (17)	-440	143 (1)
220	103 (21)	200	116 (18)	130	125 (16)	-100	153 (14)	-425	144 (1)
240	100 (21)	220	122 (16)	150	154 (29)	-120	150 (19)	-380	144 (1)
260	81 (15)	240	119 (14)	170	142 (22)	-140	127 (16)	-335	144 (1)
280	74 (20)	260	117 (15)	190	117 (17)	-160	140 (18)	-290	145 (1)
300	122 (27)	280	96 (13)	210	148 (24)	-180	169 (19)	-245	146 (1)
320	87 (16)	300	106 (13)	230	129 (18)	-200	84 (44)	-200	143 (1)
				250	138 (15)			-155	144 (1)
				270	131 (15)			-110	143 (1)
				290	125 (15)			-65	144 (1)
				310	130 (14)			-20	146 (1)
				330	128 (14)			15	145 (1)
				350	121 (13)			50	147 (1)
				370	137 (20)			85	148 (1)
				390	105 (13)			120	148 (1)
				410	121 (15)			155	148 (1)
				430	114 (15)			190	147 (1)
								225	148 (1)
								260	149 (1)
								295	150 (1)
								330	150 (1)

Table A1.11: LA ICP-MS lithium results for DIFF7 – DIFF8 – DIFF10 – DIFF12 – DIFF13

DIFF8 - 1200 °C - 20 hrs		DIFF8 - 1200 °C - 20 hrs		DIFF10 - 1200 °C - 0 s		DIFF12 - 1250 °C - 20 hrs		DIFF13 - 1050 °C - 15 min	
Dist [µm]	Li [µg/g] (err)	Dist [µm]	Li [µg/g] (err)	Dist [µm]	Li [µg/g] (err)	Dist [µm]	Li [µg/g] (err)	Dist [µm]	Li [µg/g] (err)
-3900	131 (1)	-4850	127 (1)	-2625	146 (22)	-3350	98 (8)	-3150	143 (11)
-3700	130 (1)	-4650	128 (1)	-2475	164 (22)	-3200	94 (69	-3000	142 (9)
-3500	129 (1)	-4450	129 (1)	-2325	202 (40)	-3050	90 (6)	-2850	148 (9)
-3300	129 (1)	-4250	127 (1)	-2175	218 (44)	-2900	96 (8)	-2700	158 (10)
-3100	129 (1)	-4050	129 (1)	-2025	220 (48)	-2750	112 (16)	-2550	163 (9)
-2900	129 (1)	-3850	128 (1)	-1875	210 (36)	-2600	97 (10)	-2400	163 (12)
-2700	129 (1)	-3650	128 (1)	-1725	198 (35)	-2450	102 (10)	-2250	176 (14)
-2500	129 (1)	-3450	127 (1)	-1575	154 (21)	-2300	109 (11)	-2100	170 (13)
-2300	130 (1)	-3250	127 (1)	-1425	191 (32)	-2150	94 (9)	-1950	167 (15)
-2100	130 (1)	-3050	128 (1)	-1275	162 (26)	-2000	90 (8)	-1800	160 (14)
-1900	130 (1)	-2850	126 (1)	-1125	164 (23)	-1850	105 (10)	-1650	160 (13)
-1700	131 (1)	-2650	127 (1)	-975	210 (38)	-1700	97 (8)	-1500	161 (14)
-1500	129 (1)	-2450	128 (1)	-825	168 (26)	-1550	103 (9)	-1350	162 (14)
-1300	131 (1)	-2250	128 (1)	-675	147 (22)	-1400	95 (8)	-1200	149 (14)
-1100	131 (1)	-2050	127 (1)	-525	156 (25)	-1250	92 (7)	-1050	144 (14)
-900	132 (1)	-1850	129 (1)	-375	131 (18)	-1100	93 (7)	-900	128 (9)
-700	132 (1)	-1650	128 (1)	-225	146 (25)	-950	93 (8)	-750	145 (12)
-500	131 (1)	-1450	128 (1)	-75	112 (13)	-800	96 (8)	-600	142 (12)
-300	132 (1)	-1250	127 (1)	75	120 (15)	-650	100 (7)	-450	135 (11)
-100	132 (1)	-1050	128 (1)	225	113 (14)	-500	103 (9)	-300	134 (11)
100	132 (1)	-850	127 (1)	375	102 (12)	-350	106 (8)	-150	129 (9)
300	133 (1)	-650	128 (1)	525	97 (11)	-200	104 (8)	0	113 (9)
500	132 (1)	-450	130 (1)	675	95 (10)	-50	98 (6)	150	117 (8)
700	132 (1)	-250	129 (1)	825	79 (7)	100	88 (6)	300	103 (8)
900	132 (1)	-50	129 (1)	975	84 (8)	250	101 (8)	450	101 (8)
1100	133 (1)	150	129 (1)	1125	78 (7)	400	99 (7)	600	96 (7)
1300	131 (1)	350	129 (1)	1275	81 (8)	550	98 (6)	750	84 (6)
1500	132 (1)	550	129 (1)	1425	74 (6)	700	97 (7)	900	83 (7)
1700	132 (1)	750	129 (1)	1575	71 (6)	850	104 (7)	1050	78 (6)
1900	132 (1)	950	129 (1)	1725	70 (6)	1000	100 (7)	1200	73 (5)
2100	131 (1)	1150	129 (1)	1875	68 (7)	1150	94 (6)	1350	68 (4)
2300	131 (1)	1350	130 (1)	2025	60 (6)	1300	101 (8)	1500	66 (4)
2500	131 (1)	1550	129 (1)	2175	56 (5)	1450	94 (6)	1650	67 (5)
2700	131 (1)	1750	129 (1)	2325	61 (5)	1600	103 (8)	1800	65 (6)
2900	133 (1)	1950	130 (1)	2475	58 (5)	1750	100 (6)	1950	61 (10)
3100	133 (1)	2150	129 (1)	2625	58 (6)	1900	100 (6)	2100	56 (5)
3300	133 (1)	2350	131 (1)	2775	54 (4)	2050	100 (7)	2250	56 (5)
3500	132 (1)	2550	129 (1)	2925	55 (4)	2200	103 (7)	2400	63 (8)
3700	133 (1)	2750	128 (1)	3075	53 (4)	2350	97 (7)	2550	63 (7)
3900	132 (1)	2950	127 (1)	3225	57 (5)	2500	96 (6)	2700	64 (5)
4100	132 (1)	3150	128 (1)	3375	54 (4)	2650	104 (6)	2850	60 (5)
4300	130 (1)	3350	129 (1)	3525	52 (5)	2800	106 (7)	3000	57 (5)
4500	130 (1)	3550	127 (1)	3675	51 (4)	2950	104 (7)	3150	54 (4)
4700	129 (1)	3750	125 (1)	3825	58 (5)	3100	106 (6)		
4900	127 (1)	3950	126 (1)	3975	49 (3)	3250	107 (7)		

Table A1.12: LA ICP-MS boron results for DIFF1 – DIFF2 – DIFF3 – DIFF5 – DIFF6

DIFF1 - 700 °C 0 s		DIFF2 - 700 °C 30 min		DIFF3 - 800 °C 30 min		DIFF5 - 1000 °C 0 s		DIFF6 - 1000 °C 24 hrs	
Dist [µm]	B [µg/g] (err)	Dist [µm]	B [µg/g] (err)	Dist [µm]	B [µg/g] (err)	Dist [µm]	B [µg/g] (err)	Dist [µm]	B [µg/g] (err)
-280	822 (205)	-300	605 (60)	-370	856 (154)	-200	524 (167)	-800	596 (8)
-260	771 (131)	-280	616 (65)	-350	891 (143)	-180	644 (75)	-785	605 (7)
-240	812 (147)	-260	618 (62)	-330	820 (120)	-160	569 (65)	-770	604 (8)
-220	692 (115)	-240	636 (73)	-310	818 (129)	-140	550 (56)	-755	607 (7)
-200	813 (195)	-220	623 (65)	-290	750 (107)	-120	583 (77)	-740	600 (7)
-180	748 (136)	-200	693 (85)	-270	1016 (188)	-100	614 (64)	-725	600 (6)
-160	831 (180)	-180	683 (79)	-250	914 (142)	-80	606 (64)	-710	605 (8)
-140	770 (202)	-160	676 (73)	-230	756 (140)	-60	642 (75)	-695	610 (7)
-120	878 (141)	-140	608 (67)	-210	735 (101)	-40	617 (62)	-680	612 (7)
-100	743 (127)	-120	590 (64)	-190	780 (117)	-20	632 (67)	-665	609 (7)
-80	780 (158)	-100	619 (64)	-170	785 (137)	0	441 (48)	-650	594 (8)
-60	602 (167)	-80	652 (70)	-150	948 (254)	20	217 (87)	-635	608 (8)
-40	780 (139)	-60	693 (73)	-130	732 (146)	40	189 (40)	-620	597 (7)
-20	789 (268)	-40	613 (76)	-110	908 (223)	60	151 (29)	-605	602 (7)
0	630 (80)	-20	539 (157)	-90	827 (195)	80	192 (24)	-590	600 (7)
20	236 (34)	0	367 (83)	-70	1052 (204)	100	212 (28)	-575	602 (7)
40	250 (48)	20	156 (30)	-50	920 (186)	120	138 (31)	-560	602 (7)
60	194 (33)	40	200 (35)	-30	948 (252)	140	178 (36)	-545	616 (8)
80	204 (50)	60	188 (31)	-10	915 (173)	160	147 (27)	-530	607 (7)
100	232 (45)	80	195 (24)	10	227 (74)	180	175 (30)	-515	601 (7)
120	185 (35)	100	179 (31)	30	180 (27)	200	193 (31)	-500	600 (7)
140	242 (70)	120	203 (40)	50	264 (62)	220	196 (32)	-485	609 (7)
160	282 (66)	140	201 (33)	70	261 (75)	240	157 (31)	-470	610 (7)
180	289 (115)	160	209 (36)	90	336 (71)	260	163 (27)	-455	605 (7)
200	198 (40)	180	203 (36)	110	200 (45)	280	141 (25)	-440	597 (7)
220	233 (56)	200	209 (40)	130	190 (40)	300	146 (27)	-425	590 (7)
240	196 (46)	220	206 (37)	150	226 (52)	320	184 (30)	-380	597 (7)
260	215 (54)	240	173 (34)	170	217 (29)	340	165 (25)	-335	599 (7)
280	229 (59)	260	174 (29)	190	212 (47)	360	166 (27)	-290	597 (8)
300	261 (53)	280	159 (28)	210	203 (37)	380	168 (29)	-245	604 (7)
320	252 (59)	300	209 (35)	230	191 (30)	400	165 (22)	-200	595 (8)
				250	217 (38)			-155	589 (7)
				270	221 (36)			-110	587 (8)
				290	215 (35)			-65	546 (7)
				310	233 (40)			-20	441 (6)
				330	199 (32)			15	305 (5)
				350	189 (30)			50	216 (4)
				370	208 (44)			85	172 (4)
				390	189 (27)			120	161 (4)
				410	183 (27)			155	161 (4)
				430	190 (30)			190	152 (4)
								225	157 (4)
								260	158 (4)
								295	161 (4)
								330	159 (4)
								-155	589 (7)
								-110	587 (8)
								-65	546 (7)
								-20	441 (6)
								15	305 (5)

Table A1.13: LA ICP-MS boron results for DIFF7 – DIFF8 – DIFF10 – DIFF12 – DIFF13

DIFF7 - 1100 °C 20 hrs		DIFF8 - 1200 °C 20 hrs		DIFF10 - 1200 °C 0 s		DIFF12 - 1250 °C 20 hrs		DIFF13 - 1050 °C 15 min	
Dist [µm]	B [µg/g] (err)	Dist [µm]	B [µg/g] (err)	Dist [µm]	B [µg/g] (err)	Dist [µm]	B [µg/g] (err)	Dist [µm]	B [µg/g] (err)
-3900	590 (8)	-4850	603 (7)	-2625	477 (127)	-3350	528 (45)	-3150	552 (45)
-3700	583 (7)	-4650	600 (8)	-2475	577 (80)	-3200	525 (40)	-3000	563 (33)
-3500	570 (7)	-4450	605 (8)	-2325	630 (93)	-3050	534 (39)	-2850	553 (39)
-3300	564 (8)	-4250	604 (8)	-2175	799 (150)	-2900	510 (45)	-2700	584 (46)
-3100	555 (7)	-4050	614 (8)	-2025	656 (114)	-2750	548 (68)	-2550	528 (32)
-2900	554 (8)	-3850	606 (7)	-1875	772 (143)	-2600	552 (52)	-2400	561 (42)
-2700	558 (7)	-3650	609 (7)	-1725	639 (90)	-2450	521 (54)	-2250	607 (49)
-2500	558 (7)	-3450	600 (7)	-1575	628 (99)	-2300	634 (70)	-2100	615 (50)
-2300	563 (7)	-3250	602 (7)	-1425	776 (139)	-2150	558 (51)	-1950	572 (44)
-2100	567 (7)	-3050	602 (7)	-1275	718 (128)	-2000	510 (56)	-1800	552 (36)
-1900	572 (7)	-2850	596 (8)	-1125	541 (83)	-1850	568 (60)	-1650	587 (55)
-1700	575 (7)	-2650	596 (7)	-975	728 (109)	-1700	506 (49)	-1500	571 (45)
-1500	569 (7)	-2450	592 (8)	-825	721 (134)	-1550	529 (48)	-1350	543 (41)
-1300	574 (7)	-2250	589 (8)	-675	593 (85)	-1400	464 (43)	-1200	544 (54)
-1100	579 (7)	-2050	588 (8)	-525	601 (97)	-1250	489 (44)	-1050	564 (52)
-900	576 (6)	-1850	587 (7)	-375	554 (72)	-1100	509 (43)	-900	528 (40)
-700	568 (6)	-1650	586 (8)	-225	649 (106)	-950	505 (47)	-750	575 (43)
-500	541 (7)	-1450	582 (7)	-75	620 (78)	-800	511 (54)	-600	538 (42)
-300	495 (6)	-1250	567 (7)	75	176 (26)	-650	534 (46)	-450	547 (40)
-100	415 (6)	-1050	563 (7)	225	172 (25)	-500	559 (60)	-300	556 (43)
100	334 (5)	-850	551 (7)	375	177 (24)	-350	551 (55)	-150	529 (40)
300	266 (4)	-650	534 (7)	525	134 (16)	-200	495 (50)	0	501 (36)
500	204 (4)	-450	505 (6)	675	171 (20)	-50	421 (38)	150	524 (44)
700	177 (4)	-250	456 (7)	825	133 (22)	100	271 (31)	300	157 (15)
900	164 (4)	-50	404 (5)	975	152 (17)	250	194 (27)	450	144 (17)
1100	163 (4)	150	351 (5)	1125	147 (14)	400	143 (24)	600	144 (15)
1300	161 (4)	350	292 (5)	1275	172 (21)	550	147 (21)	750	133 (15)
1500	159 (4)	550	242 (4)	1425	150 (18)	700	144 (16)	900	129 (14)
1700	158 (4)	750	204 (4)	1575	147 (16)	850	164 (19)	1050	148 (17)
1900	156 (4)	950	177 (4)	1725	148 (15)	1000	147 (21)	1200	138 (14)
2100	161 (4)	1150	163 (4)	1875	142 (18)	1150	138 (18)	1350	133 (14)
2300	157 (4)	1350	153 (4)	2025	143 (16)	1300	149 (16)	1500	137 (14)
2500	155 (4)	1550	154 (4)	2175	144 (14)	1450	146 (17)	1650	152 (19)
2700	153 (4)	1750	154 (4)	2325	162 (14)	1600	160 (16)	1800	148 (18)
2900	156 (4)	1950	153 (4)	2475	159 (15)	1750	162 (17)	1950	156 (24)
3100	156 (3)	2150	149 (4)	2625	163 (16)	1900	157 (17)	2100	167 (25)
3300	158 (4)	2350	148 (4)	2775	159 (16)	2050	138 (13)	2250	143 (22)
3500	157 (4)	2550	152 (4)	2925	162 (19)	2200	148 (17)	2400	155 (35)
3700	157 (4)	2750	151 (4)	3075	161 (15)	2350	144 (16)	2550	128 (21)
3900	153 (4)	2950	155 (4)	3225	157 (17)	2500	143 (15)	2700	137 (22)
4100	160 (4)	3150	154 (4)	3375	145 (15)	2650	160 (12)	2850	128 (21)
4300	155 (4)	3350	154 (3)	3525	153 (16)	2800	133 (14)	3000	167 (24)
4500	156 (4)	3550	154 (3)	3675	149 (17)	2950	149 (15)	3150	142 (19)
4700	156 (4)	3750	150 (3)	3825	160 (14)	3100	151 (13)		
4900	155 (4)	3950	155 (4)	3975	138 (12)	3250	163 (13)		

Appendix A2: Decompression tables

Table A2.1: BND calculation for each BSE image. Front and Side refer to the horizontal or vertical cut of the picture

Picture	Count	Tot Area [µm^2]	Size [µm]	% Area	BND [m^3]	log BND
LPR50_DEC2_front-1	114	43554	382.1	2.2	2.07E+12	12.32
LPR50_DEC2_front-2	67	24084	359.5	2.0	2.54E+12	12.40
LPR50_DEC2_front-3	261	36619	140.3	2.4	2.31E+12	12.36
LPR50_DEC2_front-4	214	34853	162.9	2.3	1.74E+12	12.24
LPR50_DEC2_front-5	73	14484	198.4	2.9	2.51E+12	12.40
LPR50_DEC2_front-6	88	13130	149.2	2.7	4.33E+12	12.64
LPR50_DEC2_front-7	26	7823	300.9	1.6	3.26E+12	12.51
LPR50_DEC2_front-8	24	8124	338.5	1.6	1.71E+12	12.23
LPR50_DEC2_front-9	27	9487	130.0	1.9	5.81E+12	12.76
LPR50_DEC2_side-1	80	25007	312.6	1.7	2.27E+12	12.36
LPR50_DEC2_side-2	96	27200	283.3	2.0	3.71E+12	12.57
LPR50_DEC2_side-3	126	25183	199.9	2.1	2.81E+12	12.45
LPR50_DEC2_side-4	74	26012	351.5	2.2	2.15E+12	12.33
LPR50_DEC2_side-5	42	10796	257.0	2.1	8.19E+12	12.91
LPR50_DEC2_side-6	53	11498	217.0	2.3	2.96E+12	12.47
LPR50_DEC2_side-7	39	12698	325.6	2.5	2.17E+12	12.34
LPR50_DEC2_side-8	42	8459	201.4	1.7	4.07E+12	12.61
LPR50_DEC2_side-9	53	9261	174.7	1.8	3.30E+12	12.52
LPR50_DEC3_front-1	342	48165	127.8	3.7	1.91E+13	13.28
LPR50_DEC3_front-2	268	33634	125.5	4.3	2.87E+13	13.46
LPR50_DEC3_front-3	292	37551	128.6	4.0	2.49E+13	13.40
LPR50_DEC3_front-4	239	34471	144.2	5.3	2.85E+13	13.45
LPR50_DEC3_front-5	174	21365	122.8	5.4	3.31E+13	13.52
LPR50_DEC3_front-6	201	22930	114.1	4.6	2.97E+13	13.47
LPR50_DEC3_front-7	195	23052	118.2	4.7	3.45E+13	13.54
LPR50_DEC3_front-8	189	21606	114.3	4.4	2.19E+13	13.34
LPR50_DEC3_front-9	168	18221	108.5	3.9	3.64E+13	13.56
LPR50_DEC3_side-1	591	100126	169.4	3.7	1.38E+13	13.14
LPR50_DEC3_side-2	562	82497	146.8	4.6	2.37E+13	13.38
LPR50_DEC3_side-3	536	82765	154.4	4.6	2.22E+13	13.35
LPR50_DEC3_side-4	521	77937	149.6	4.4	1.80E+13	13.25
LPR50_DEC3_side-5	196	26326	134.3	5.2	2.54E+13	13.40
LPR50_DEC3_side-6	186	25064	134.8	4.9	2.63E+13	13.42
LPR50_DEC3_side-7	193	20923	108.4	4.1	3.28E+13	13.52
LPR50_DEC3_side-8	206	24719	120.0	4.8	3.05E+13	13.48

Table A2.1:continuation

Picture	Count	Tot Area [µm²]	Size [µm]	% Area	BND [m³]	log BND
LPR50_DEC3_side-9	193	21743	112.7	4.2	3.14E+13	13.50
LPR50_DEC4_front-1	359	194288	541.2	10.4	6.57E+12	12.82
LPR50_DEC4_front-2	283	162610	574.6	11.1	7.22E+12	12.86
LPR50_DEC4_front-3	276	141107	511.3	10.6	6.91E+12	12.84
LPR50_DEC4_front-4	338	157528	466.1	11.3	7.51E+12	12.88
LPR50_DEC4_front-5	129	60910	472.2	11.8	9.46E+12	12.98
LPR50_DEC4_front-6	102	47221	463.0	9.6	6.34E+12	12.80
LPR50_DEC4_front-7	127	60472	476.2	12.3	7.91E+12	12.90
LPR50_DEC4_front-8	121	55848	461.6	11.3	7.14E+12	12.85
LPR50_DEC4_front-9	96	44786	466.5	9.1	6.66E+12	12.82
LPR50_DEC4_side-1	592	341033	576.1	10.5	6.28E+12	12.80
LPR50_DEC4_side-2	376	215953	574.3	12.2	7.37E+12	12.87
LPR50_DEC4_side-3	391	200754	513.4	11.4	8.03E+12	12.90
LPR50_DEC4_side-4	366	212888	581.7	12.1	7.25E+12	12.86
LPR50_DEC4_side-5	117	56887	486.2	11.6	8.65E+12	12.94
LPR50_DEC4_side-6	102	54014	529.5	11.0	6.65E+12	12.82
LPR50_DEC4_side-7	113	55008	486.8	11.2	8.60E+12	12.93
LPR50_DEC4_side-8	114	59449	521.5	12.1	7.30E+12	12.86
LPR50_DEC4_side-9	134	63689	475.3	13.0	9.75E+12	12.99
LPR50_DEC5_front-1	929	66775	71.9	3.0	5.27E+13	13.72
LPR50_DEC5_front-2	945	62885	66.5	4.7	6.67E+13	13.82
LPR50_DEC5_front-3	820	48643	59.3	3.9	7.54E+13	13.88
LPR50_DEC5_front-4	918	57764	62.9	4.2	7.33E+13	13.87
LPR50_DEC5_front-5	409	24253	59.3	4.8	7.98E+13	13.90
LPR50_DEC5_front-6	401	25760	64.2	5.1	9.86E+13	13.99
LPR50_DEC5_front-7	364	18817	51.7	3.8	8.54E+13	13.93
LPR50_DEC5_front-8	348	21176	60.9	4.2	8.43E+13	13.93
LPR50_DEC5_front-9	376	19011	50.6	3.8	9.76E+13	13.99
LPR50_DEC5_side-1	499	58657	117.5	4.1	4.63E+13	13.67
LPR50_DEC5_side-2	638	58252	91.3	5.0	5.41E+13	13.73
LPR50_DEC5_side-3	617	46116	74.7	3.9	5.47E+13	13.74
LPR50_DEC5_side-4	690	64057	92.8	4.8	5.52E+13	13.74
LPR50_DEC5_side-5	320	20320	63.5	4.1	7.00E+13	13.85
LPR50_DEC5_side-6	305	25632	84.0	5.1	6.25E+13	13.80
LPR50_DEC5_side-7	313	23682	75.7	4.7	6.22E+13	13.79
LPR50_DEC5_side-8	328	26036	79.4	5.2	6.44E+13	13.81
LPR50_DEC5_side-9	306	23507	76.8	4.7	6.01E+13	13.78
LPR50_DEC7_front-1	59	158159	2680.7	4.8	2.51E+11	11.40

Table A2.1:continuation

Picture	Count	Tot Area [µm²]	Size [µm]	% Area	BND [m³]	log BND
LPR50_DEC7_front-2	28	99344	3548.0	5.7	2.26E+11	11.35
LPR50_DEC7_front-3	44	69278	1574.5	4.0	5.47E+11	11.74
LPR50_DEC7_front-4	36	77245	2145.7	5.8	1.36E+11	11.13
LPR50_DEC7_front-5	32	40669	1270.9	8.2	2.18E+11	11.34
LPR50_DEC7_front-6	36	44241	1228.9	9.0	5.66E+11	11.75
LPR50_DEC7_front-7	24	23340	972.5	4.7	5.56E+11	11.74
LPR50_DEC7_front-8	45	24318	540.4	4.9	7.86E+11	11.90
LPR50_DEC7_front-9	35	31585	902.4	6.4	7.60E+10	10.88
LPR50_DEC7_side-1	49	113322	2312.7	3.8	2.78E+11	11.44
LPR50_DEC7_side-2	28	63613	2271.9	4.0	2.19E+11	11.34
LPR50_DEC7_side-3	36	74349	2065.3	4.2	2.25E+11	11.35
LPR50_DEC7_side-4	25	55068	2202.7	4.2	2.02E+11	11.31
LPR50_DEC7_side-5	18	33387	1854.8	6.8	2.78E+11	11.44
LPR50_DEC7_side-6	23	25704	1117.6	5.2	3.87E+11	11.59
LPR50_DEC7_side-7	12	25891	2157.5	5.2	6.30E+11	11.80
LPR50_DEC7_side-8	14	31345	2238.9	6.4	2.99E+11	11.48
LPR50_DEC7_side-9	30	35122	1170.7	7.1	6.24E+11	11.79
LPR50_DEC9_front-1	77	269612	3501.5	6.5	1.91E+11	11.28
LPR50_DEC9_front-2	30	98052	3268.4	5.6	1.69E+11	11.23
LPR50_DEC9_front-3	31	123450	3982.3	7.0	1.46E+11	11.16
LPR50_DEC9_front-4	43	138346	3217.3	7.9	1.73E+11	11.24
LPR50_DEC9_front-5	19	37439	1970.5	7.6	1.98E+11	11.30
LPR50_DEC9_front-6	17	39738	2337.5	8.1	1.98E+11	11.30
LPR50_DEC9_front-7	13	50044	3849.5	10.1	1.92E+11	11.28
LPR50_DEC9_front-8	14	34806	2486.1	7.1	1.87E+11	11.27
LPR50_DEC9_front-9	13	40296	3099.7	8.2	2.00E+11	11.30
LPR50_DEC9_side-1	53	308612	5822.9	5.6	9.17E+10	10.96
LPR50_DEC9_side-2	19	104884	5520.2	6.0	9.01E+10	10.95
LPR50_DEC9_side-3	15	101729	6781.9	5.8	5.17E+10	10.71
LPR50_DEC9_side-4	13	100524	7732.7	5.7	9.22E+10	10.96
LPR50_DEC9_side-5	6	44974	6424.8	9.1	1.13E+11	11.05
LPR50_DEC9_side-6	6	45761	7626.9	9.3	8.96E+10	10.95
LPR50_DEC9_side-7	8	48642	6080.3	9.9	1.18E+11	11.07
LPR50_DEC9_side-8	17	39353	2314.9	8.0	3.63E+11	11.56
LPR50_DEC9_side-9	6	22315	3719.2	4.5	1.41E+11	11.15
LPR200_DEC1_front-1	320	41496	129.7	1.9	8.77E+12	12.94
LPR200_DEC1_front-2	221	25186	114.0	2.2	1.32E+13	13.12
LPR200_DEC1_front-3	258	32429	125.7	2.6	1.12E+13	13.05

Table A2.1:continuation

Picture	Count	Tot Area [µm²]	Size [µm]	% Area	BND [m³]	log BND
LPR200_DEC1_front-4	221	28046	126.9	2.2	1.10E+13	13.04
LPR200_DEC1_front-5	86	8396	97.6	1.7	1.76E+13	13.24
LPR200_DEC1_front-6	122	11580	94.9	2.3	1.64E+13	13.22
LPR200_DEC1_front-7	114	8979	78.8	1.8	1.41E+13	13.15
LPR200_DEC1_front-8	107	7155	66.9	1.4	1.48E+13	13.17
LPR200_DEC1_front-9	108	8322	77.1	1.7	1.69E+13	13.23
LPR200_DEC1_side-1	752	111378	148.1	2.0	9.03E+12	12.96
LPR200_DEC1_side-2	247	35493	143.7	2.0	1.05E+13	13.02
LPR200_DEC1_side-3	258	31889	123.6	1.8	1.00E+13	13.00
LPR200_DEC1_side-4	235	33679	143.3	1.9	9.18E+12	12.96
LPR200_DEC1_side-5	114	11676	102.4	2.4	2.43E+13	13.38
LPR200_DEC1_side-6	83	10077	121.4	2.0	1.36E+13	13.13
LPR200_DEC1_side-7	71	11824	166.5	2.4	1.25E+13	13.10
LPR200_DEC1_side-8	93	12526	134.7	2.5	1.05E+13	13.02
LPR200_DEC1_side-9	116	10427	89.9	2.1	2.87E+13	13.46
LPR200_DEC5_front-1	444	53651	120.8	2.4	2.03E+13	13.31
LPR200_DEC5_front-2	404	32047	79.3	3.2	4.26E+13	13.63
LPR200_DEC5_front-3	598	45941	76.8	3.4	4.14E+13	13.62
LPR200_DEC5_front-4	519	46229	89.1	3.4	4.19E+13	13.62
LPR200_DEC5_front-5	237	17655	74.5	3.6	5.63E+13	13.75
LPR200_DEC5_front-6	249	20396	81.9	4.1	5.53E+13	13.74
LPR200_DEC5_front-7	235	15886	67.6	3.2	3.08E+13	13.49
LPR200_DEC5_front-8	208	16832	80.9	3.4	4.11E+13	13.61
LPR200_DEC5_front-9	236	18089	76.7	3.6	5.35E+13	13.73
LPR200_DEC5_side-1	637	51677	81.1	2.5	3.27E+13	13.51
LPR200_DEC5_side-2	722	64386	89.2	3.7	3.52E+13	13.55
LPR200_DEC5_side-3	692	64177	92.7	3.7	3.39E+13	13.53
LPR200_DEC5_side-4	661	58380	88.3	3.3	3.62E+13	13.56
LPR200_DEC5_side-5	209	15667	75.0	3.2	4.25E+13	13.63
LPR200_DEC5_side-6	226	17301	76.6	3.5	4.77E+13	13.68
LPR200_DEC5_side-7	202	14595	72.3	2.9	4.59E+13	13.66
LPR200_DEC5_side-8	210	14181	67.5	2.9	4.42E+13	13.65
LPR200_DEC5_side-9	226	20063	88.8	4.0	4.26E+13	13.63

Table A2.2: Electron microprobe results of major elements of the decompression samples, and water values from the difference method and by Raman spectroscopy measurements. Numbers in brackets are the standard deviation errors.

Sample	**Dec. time**	**SiO_2**	**Al_2O_3**	**Na_2O**	**K_2O**	**CaO**	**MgO**	**MnO**	**TiO_2**	**FeO**	**H_2O**	**H_2O Raman**
LPR50 Dec1	30 min	74.5 (1.4)	14.4 (0.8)	4.8 (0.3)	4.25 (0.16)	0.47 0.14)	0.05 (0.02)	0.01 (0.01)	0.02 (0.01)	0.07 (0.02)	1.44 (0.27)	1.11 (0.10)
LPR200 Dec1	30 min	74.7 (0.4)	13.3 (0.3)	4.8 (0.2)	3.78 (0.07)	0.37 0.05)	0.03 (0.01)	0.01 (0.01)	0.01 (0.01)	0.09 (0.02)	2.95 (0.24)	3.00 (0.27)
LPR50 Dec2	2 hrs	74.8 (0.8)	13.8 (0.6)	4.2 (0.3)	3.87 (0.09)	0.45 (0.07)	0.03 (0.01)	0.01 (0.01)	0.02 (0.02)	0.05 (0.02)	2.82 (0.19)	2.83 (0.19)
LPR200 Dec2	2 hrs	75.1 (0.9)	14.1 (0.5)	4.5 (0.3)	3.98 (0.16)	0.43 (0.08)	0.04 (0.01)	0.01 (0.01)	0.02 (0.02)	0.04 (0.02)	1.77 (0.32)	1.91 (0.20)
LPR50 Dec3	30 min	75.2 (0.5)	13.2 (0.4)	4.1 (0.1)	3.96 (0.05)	0.38 (0.06)	0.03 (0.01)	0.01 (0.01)	0.04 (0.02)	0.04 (0.02)	3.12 (0.23)	3.12 (0.26)
LPR200 Dec4	2 hrs	74.9 (0.8)	13.5 (0.5)	4.1 (0.1)	3.88 (0.08)	0.40 (0.08)	0.03 (0.01)	0.01 (0.01)	0.01 (0.01)	0.02 (0.01)	3.09 (0.13)	2.99 (0.26)
LPR200 Dec4	2 hrs	73.4 (1.0)	15.8 (0.8)	4.5 (0.2)	4.12 (0.21)	0.52 (0.10)	0.06 (0.02)	0	0.02 (0.01)	0.04 (0.03)	1.53 (0.10)	1.74 (0.42)
LPR200 Dec5	30 min	74.2 (0.9)	14.0 (0.5)	4.2 (0.3)	3.92 (0.05)	0.46 (0.03)	0.04 (0.01)	0.01 (0.01)	0.01 (0.01)	0.03 (0.03)	3.09 (0.25)	3.11 (0.09)
LPR50 Dec5	30 min	74.6 (0.9)	13.7 (0.6)	4.1 (0.2)	3.94 (0.10)	0.45 (0.24)	0.04 (0.01)	0.01 (0.01)	0.01 (0.01)	0.03 (0.02)	3.15 (0.25)	3.08 (0.12)
LPR50 Dec7	5 hrs	74.8 (0.9)	13.7 (0.5)	4.1 (0.2)	3.85 (0.05)	0.37 (0.07)	0.04 (0.02)	0.01 (0.01)	0.02 (0.02)	0.03 (0.01)	2.99 (0.15)	2.95 (0.09)
LPR50 Dec9a	10 hrs	74.9 (0.5)	13.6 (0.3)	4.2 (0.1)	3.87 (0.04)	0.38 (0.02)	0.04 (0.01)	0.01 (0.01)	0.02 (0.02)	0.02 (0.02)	2.96 (0.22)	2.97 (0.14)
LPR50 STDA		74.9 (0.9)	13.1 (0.7)	3.9 (0.2)	3.73 (0.19)	0.31 (0.07)	0.03 (0.01)	0.01 (0.01)	0.01 (0.01)	0.05 (0.03)	3.97 (0.12)	
LPR200 STDB		74.8 (0.8)	12.9 (0.7)	4.00 (0.2)	3.75 (0.08)	0.40 (0.07)	0.03 (0.01)	0.01 (0.01)	0.02 (0.02)	0.08 (0.02)	3.98 (0.12)	

Table A2.3: Li and B concentration and isotopic ratios SIMS results on the decompression samples (b1 and b2 are the distinction between analyses of bubble 1 and bubble 2 on the sample)

Sample	Dist [µm]	Li [µg/g]	Li err [µg/g]	δ^{7}Li ‰	δ^{7}Li err	B [µg/g]	B err [µg/g]	δ^{11}B ‰	δ^{11}B err
LPR50-DEC3-b1-1	10	58.9	3.5	-0.34	2.99	225.8	18.6	0.24	2.39
LPR50-DEC3-b1-2	30	58.4	2.7	-3.23	1.90	208.9	16.6	-4.13	3.20
LPR50-DEC3-b1-3	50	55.8	2.7	-6.19	3.39	192.4	14.2	-0.40	2.80
LPR50-DEC3-b1-4	70	53.5	2.4	-7.43	2.77	177.1	11.8	-0.59	3.78
LPR50-DEC3-b1-5	90	52.8	2.2	1.72	3.44	168.9	10.2	-2.68	3.98
LPR50-DEC3-b1-6	110	53.2	1.9	-4.10	2.14	165.0	9.7	0.13	3.29
LPR50-DEC3-b1-7	130	56.4	2.4	1.06	2.11	161.4	10.6	-4.92	4.58
LPR50-DEC3-b1-8	150	59.6	2.7	3.94	2.98	167.6	8.4	0.00	3.30
LPR50-DEC3-b1-9	170	65.5	4.3	-3.09	2.44	170.6	11.6	-6.61	3.96
LPR50-DEC3-b2-1	10	65.8	2.5	0.76	2.51	213.2	21.6	-3.44	3.35
LPR50-DEC3-b2-2	30	64.8	3.6	-2.66	1.96	207.0	18.5	0.39	2.75
LPR50-DEC3-b2-3	50	63.4	3.4	-1.41	3.59	206.5	19.8	-2.05	2.65
LPR50-DEC3-b2-4	70	62.2	3.3	-3.70	2.69	205.3	20.6	-7.80	2.28
LPR50-DEC3-b2-5	90	61.6	3.9	3.82	1.64	205.0	19.2	-6.03	2.65
LPR50-DEC3-b2-6	110	61.4	3.0	-3.00	2.93	195.1	21.8	-1.80	2.87
LPR50-DEC3-b2-7	130	61.1	4.4	1.56	1.76	204.5	21.8	-3.51	2.85
LPR50-DEC3-b2-8	150	61.0	3.3	-3.25	2.43	202.3	21.0	-2.26	2.77
LPR50-DEC2_b1-1	190	55.2	2.8	1.66	3.01	171.3	16.3	0.24	2.59
LPR50-DEC2_b1-2	160	57.8	2.7	2.96	2.62	178.0	18.1	2.62	2.77
LPR50-DEC2_b1-3	130	60.3	2.9	5.67	1.97	182.1	18.6	-0.29	2.72
LPR50-DEC2_b1-4	100	59.5	3.4	1.16	1.97	182.7	20.2	1.44	2.63
LPR50-DEC2_b1-5	70	59.8	3.0	3.53	2.86	180.6	18.6	-3.58	2.10
LPR50-DEC2_b1-6	40	57.8	4.0	-1.24	1.93	173.2	16.8	3.50	2.32
LPR50-DEC2_b1-7	10	55.3	2.4	1.40	2.59	163.1	13.1	0.55	3.15
LPR50-DEC2_b2-1	10	54.6	2.2	1.15	2.56	152.0	12.1	-0.18	2.38
LPR50-DEC2_b2-2	40	55.7	2.7	3.29	2.24	159.3	12.7	3.77	2.56
LPR50-DEC2_b2-3	70	58.4	2.7	2.69	2.51	166.9	15.7	-2.62	2.36
LPR50-DEC2_b2-4	100	60.3	2.3	0.75	2.71	169.9	13.7	-1.65	2.15
LPR50-DEC2_b2-5	130	62.2	2.8	3.14	2.15	169.4	14.8	1.87	2.13
LPR50-DEC2_b2-6	160	62.5	2.6	5.59	3.08	165.6	13.0	1.97	2.15
LPR50-DEC2_b2-7	190	60.8	2.2	1.76	2.08	160.3	11.6	2.52	3.12
LPR50-DEC7_b1-1	280	52.7	2.8	6.58	2.81	165.2	14.3	-2.60	2.94
LPR50-DEC7_b1-2	250	54.2	2.6	0.00	2.17	158.9	12.4	0.14	3.51
LPR50-DEC7_b1-3	220	55.0	2.7	3.31	2.12	154.1	12.2	1.20	2.87
LPR50-DEC7_b1-4	190	55.2	3.2	3.81	3.05	152.4	14.4	-1.81	2.88
LPR50-DEC7_b1-5	160	55.0	3.1	8.82	2.51	152.7	13.8	-0.02	3.94

Table A2.3 continuation

Sample	Dist [µm]	Li [µg/g]	Li err [µg/g]	δ^7Li ‰	δ^7Li err	B [µg/g]	B err [µg/g]	δ^{11}B ‰	δ^{11}B err
LPR50-DEC7_b1-6	130	54.1	3.5	2.22	2.40	153.0	15.8	-0.35	2.83
LPR50-DEC7_b1-7	100	52.6	2.6	0.44	2.41	154.2	13.6	4.03	3.13
LPR50-DEC7_b1-8	70	51.8	2.5	6.58	2.99	156.6	13.0	-1.25	3.87
LPR50-DEC7_b1-9	40	48.8	2.5	0.75	2.56	157.7	14.7	3.28	2.79
LPR50-DEC7_b1-10	10	46.0	2.0	4.40	3.75	151.1	12.9	0.93	3.46
LPR50-DEC7_b2-1	10	48.3	3.7	1.52	2.07	156.0	18.0	-0.11	2.54
LPR50-DEC7_b2-2	40	51.8	3.0	4.68	2.46	160.1	16.9	1.39	2.51
LPR50-DEC7_b2-3	70	55.1	3.0	5.59	1.76	165.9	17.6	-2.42	2.49
LPR50-DEC7_b2-4	100	57.0	4.1	5.94	2.00	166.6	21.8	2.62	2.45
LPR50-DEC7_b2-5	130	57.6	4.0	2.69	1.84	165.1	18.9	0.17	2.68
LPR50-DEC7_b2-6	160	58.5	3.9	3.93	2.32	166.1	19.7	-3.53	2.42
LPR50-DEC7_b2-7	190	58.3	4.2	3.63	2.33	167.3	20.7	0.45	2.40
LPR50-DEC7_b2-8	220	57.6	4.7	-0.76	2.62	165.7	22.5	1.22	2.44
LPR50-DEC7_b2-9	250	57.6	4.2	1.18	2.09	166.0	21.5	-0.95	2.71
LPR50-DEC7_b2-10	280	56.8	3.7	-0.22	2.78	164.9	18.5	-0.18	2.90
LPR50-DEC7_b2-11	310	57.5	3.5	6.52	2.22	163.4	18.9	-2.27	2.38
LPR50-DEC9_b1-1	190	48.6	2.7	4.85	3.25	149.4	11.5	6.53	3.22
LPR50-DEC9_b1-2	160	49.3	2.8	3.87	2.30	146.4	12.5	0.32	3.52
LPR50-DEC9_b1-3	130	49.5	2.8	-1.03	2.76	143.9	13.8	2.96	3.27
LPR50-DEC9_b1-4	100	50.6	2.7	7.15	2.41	143.1	10.7	2.94	3.31
LPR50-DEC9_b1-5	70	48.5	2.6	3.49	3.07	135.4	9.9	-0.59	3.68
LPR50-DEC9_b1-6	40	43.4	2.7	-1.24	3.01	127.3	11.7	6.42	3.44
[6]LPR50-DEC9_b1-7	10	74.6	19.0	12.58	16.84	116.4	31.6	-23.12	37.12
LPR50-DEC9_b2-1	10	44.2	2.9	2.07	3.24	127.3	11.2	5.76	3.42
LPR50-DEC9_b2-2	40	46.5	2.7	0.86	2.21	136.0	12.1	-0.27	3.51
LPR50-DEC9_b2-3	70	47.2	2.8	3.84	3.71	141.3	11.9	0.41	3.30
LPR50-DEC9_b2-4	100	45.8	1.9	-1.88	2.67	143.0	12.1	-0.21	3.31
LPR50-DEC9_b2-5	130	46.0	3.0	1.25	3.12	149.7	13.0	-1.67	3.13
LPR50-DEC9_b2-6	160	42.0	2.0	0.51	3.64	144.5	12.2	-2.03	3.31
LPR50-DEC9_b2-7	190	41.0	2.4	1.68	2.57	145.3	13.0	-1.14	2.79
LPR50-DEC9_b2-8	220	42.2	2.6	0.73	2.68	155.1	13.5	-2.43	2.97

---

[6] Discarded value, because a focus misalignment in the SIMS laser beam caused the hitting of the epoxy, which was filling the bubble, and therefore the measurement has not been included in any data evaluation.